Ben-Gurion University of the Negev

The Faculty of Natural Sciences

The Department of Geological and Environmental Sciences

Mechanical and Petrophysical behavior of oil shale from the Judea Plains, Israel

Thesis Submitted In Partial Fulfillment of the Requirements for the M.Sc. Degree in the Faculty of Natural Sciences

Ksenia Bisnovat

Under the Supervision of Prof. Yossef Hodara Hatzor

and Prof. Shimon Feinstein

September 2013

Abstract

Different aspects of the Shefela oil shale such as geology, geochemistry and hydrology were previously described in the literature, but the mechanical and petrophysical properties are described in this research for the first time. The Shefela oil shale found in central Israel is mostly a high porosity (~37%), low permeability (~0.09 mD) dark brown bituminous chalk rich in organic matter. The TOC values reach up to 20 wt% at the Ghareb formation in the middle of the investigated Aderet borehole. The permeability is strongly anisotropic, implying that vertical flow is more restricted relative to horizontal flow along the bedding planes. At room temperature, the rock exhibits a brittle behavior, the failure of which can be described by both the linear Coulomb-Mohr criterion and by the non-linear Griffith's criterion. The cohesion and the angle of internal friction obtained are 5.51 MPa and 10.7°, respectively. The Uniaxial compressive strength averages 19 MPa at the Ghareb interval and the Brazilian tensile strength averages ~3.1 MPa at dry conditions and decreases with increasing water content to a value of ~2.6 MPa on average for a water content of ~25%, being higher by 1.7 on average for the parallel to bedding tension. An empirical linear compression-dilation boundary was defined and applied to analyze the volumetric behavior of the rock in case of drilling vertical or horizontal boreholes for heating elements during a theoretical "in-situ" production process.

The porosity, permeability, Klinkenberg slip factor and total organic carbon (TOC) were measured before and after three different pyrolysis experiments. The porosity and the permeability are relatively independent of organic content before pyrolysis. Upon the release of liquids and gases from the organic matter during thermal maturation, the volume of organic matter is reduced and new space is being created. During that process, a finer secondary pore structure develops within the organic matter, enhancing the porosity by an average factor of ~1.28 up to a maximum value of 62% with relatively small variation due to changes in pyrolysis conditions. The permeability is significantly enhanced by almost an order of a magnitude on average (up to of 6.5 mD). The amount of organic matter loss depends on the initial organic matter content and on the pyrolysis conditions. Applying back pressure seems to increase the amount of residual organic matter remaining in the rock and decrease the porosity growth. Moreover, slowing down the rate of temperature increase during the pyrolysis seems to have the same effect but to a much lower extent. The degree of

thermal permeability enhancement is also related to the amount of organic matter initially in place but independent of pyrolysis conditions and can be estimated if the initial organic matter content is given. The research findings contribute to the understanding of the relationship between petrophysical properties and organic matter. Moreover, the effect of thermal maturation process and the release of water and volatile fractions on petrophysical properties are further explored. This information is of paramount importance for the scientific understanding of the migration process, and for better execution of commercial production by thermal in situ recovery from a bituminous chalk.

Acknowledgements

I would like to thank my advisors, Prof. Yossef H. Hatzor for his mentoring with dedication and enthusiasm. I extremely appreciate his professionalism and support.
Prof. Shimon Feinstein is thanked for his guidance, patience and for long productive discussions.

This research was funded by Israel Energy Initiative Ltd through BGU contract No.87244811. The financial support of IEI is greatly appreciated.
IEI Ltd. staff is also thanked for the academic and technical assistance, in particular:
Dr. Scott Nguyen is thanked for his professional guidance, patience and inspiring conversations along the whole research period.
Dr. Harold Vinegar is thanked for contributing from his broad knowledge.
The good advice and support of Dr. Itay Reznik has been invaluable on both an academic and a personal level, for which I am extremely grateful.
My special thanks to Leonardo Freitas and Edna Danon for helping to perform TOC measurements, crushing rock samples and being a great company.

Dr. Vyacheslav Palchik is thanked for his guidance and assistance in performing mechanical measurements.
I am most grateful to Mr. Diro Kozashvily for preparing the samples for the entire research (and there were a lot…) and for his kindness and patience.
The geological department staff, Mrs. Rivka Eini and Mrs. Zehala Sharabi is thanked for administrative assistance.
My friends and colleagues in the department: Guy, Gony, Yuval, Yael, Amir, Moria, Libby, Irit and Osnat are thanked for good advices and enjoyable breaks together.

Especially, I wish to thank my family that has supported and helped me along the whole academic period by giving encouragement and providing the moral and emotional support I needed to complete my thesis.
Last but not least, I would like to give my special thanks to my spouse Itzik whose patient love enabled me to stay focused and complete this work.

Contents

List of Figures

List of Tables

Chapter 1- Introduction

1.1 Background

Oil shale is a fine-grained sedimentary rock containing various amounts of organic matter called 'kerogen' that yields substantial amounts of oil and gas upon thermal maturation (Tissot and Welte, 1984; Hutton, 1987). The mechanical and petrophysical properties of oil shale are significantly affected by the organic phase, the mineralogical composition and dynamic processes. About thirty sub-basins containing Late Cretaceous carbonates-rich oil shale were described in Israel (Minster, 2009). Among the largest basins in the Levant is the Shefela basin located at central Israel (Figure 1). It extends across more than 1000 km^2 and contains the thickest oil shale succession, estimated at 100-500 m (Gvirtzman et al., 1985; Minster, 2009). This oil shale unit is associated with the En Zetim, Ghareb and Mishash formations, of the Mount Scopus group (Figure 2). The oil shale is mostly dark brown bituminous chalk, rich in organic matter- reaching up to 20 wt% (Burg et al., 2010). Different aspects of The Shefela basin (geology, geochemistry and hydrology) were previously described in the literature (Gvirtzman et al., 1985; Almogi-Labin et al., 1993; Eshet et al., 1994; Dyni, 2003; Minster, 2009; Burg et al., 2010) but the mechanical and petrophysical characteristics have not been studied as yet. This characterization of the Shefela basin and testing the thermal maturation effect on these characteristics is significant for understanding natural thermal maturation and migration processes.

1.2 Research goals and significance

The aim of this research is to characterize the mechanical and the petrophysical behavior of the oil shale from the Shefela basin. These properties are not only of great importance to engineering and earth sciences, but are also essential in the evaluation of the Shefela oil shale deposit as a potential resource of energy. Knowledge and understanding of the mechanical and petrophysical properties of the Shefela deposit are required for production planning and management and for modeling of the dynamic variations in the section and evaluation of environmental implications.

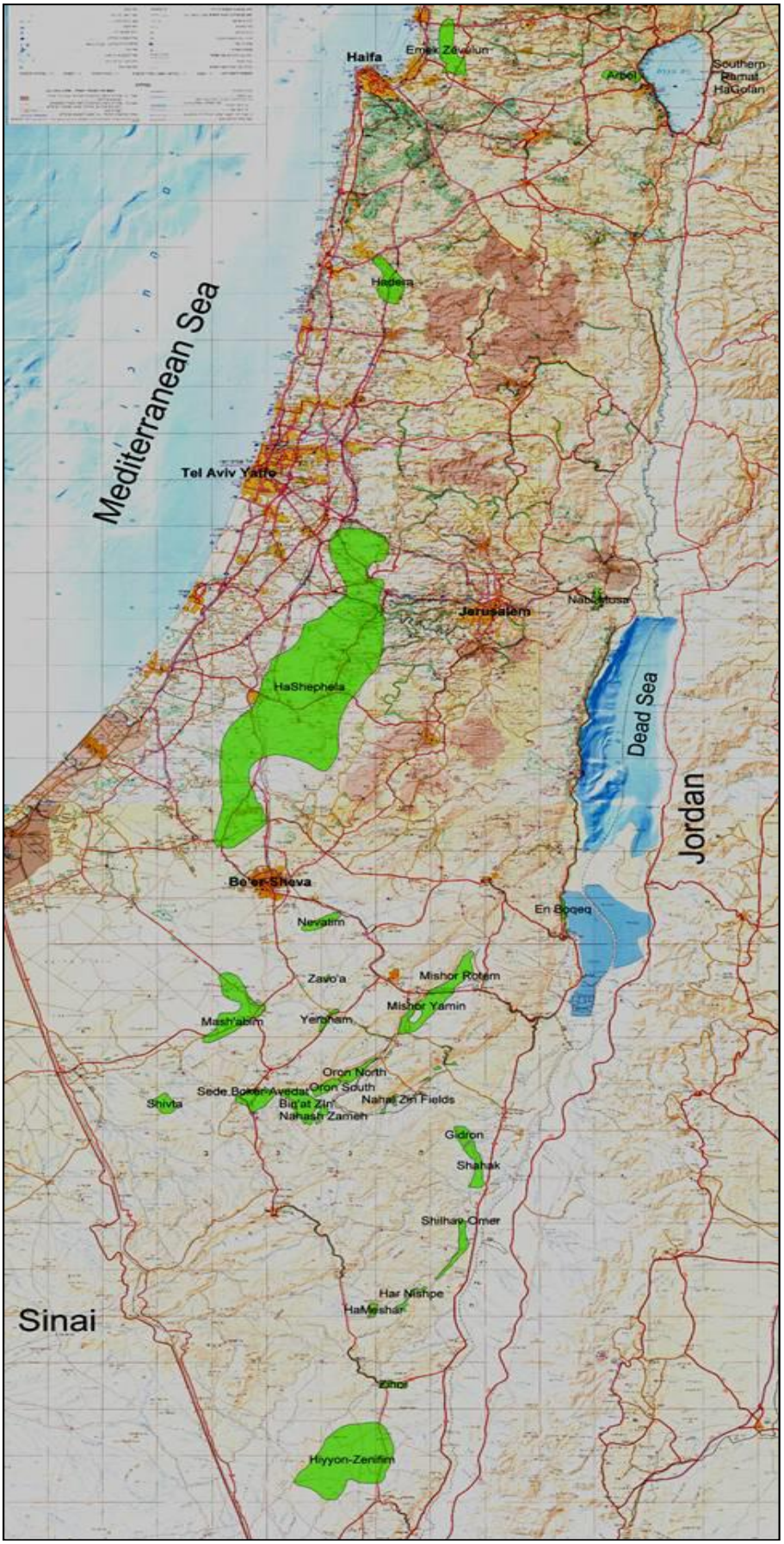

Figure 1: Oil shale deposits in Israel (Minster, 2009)

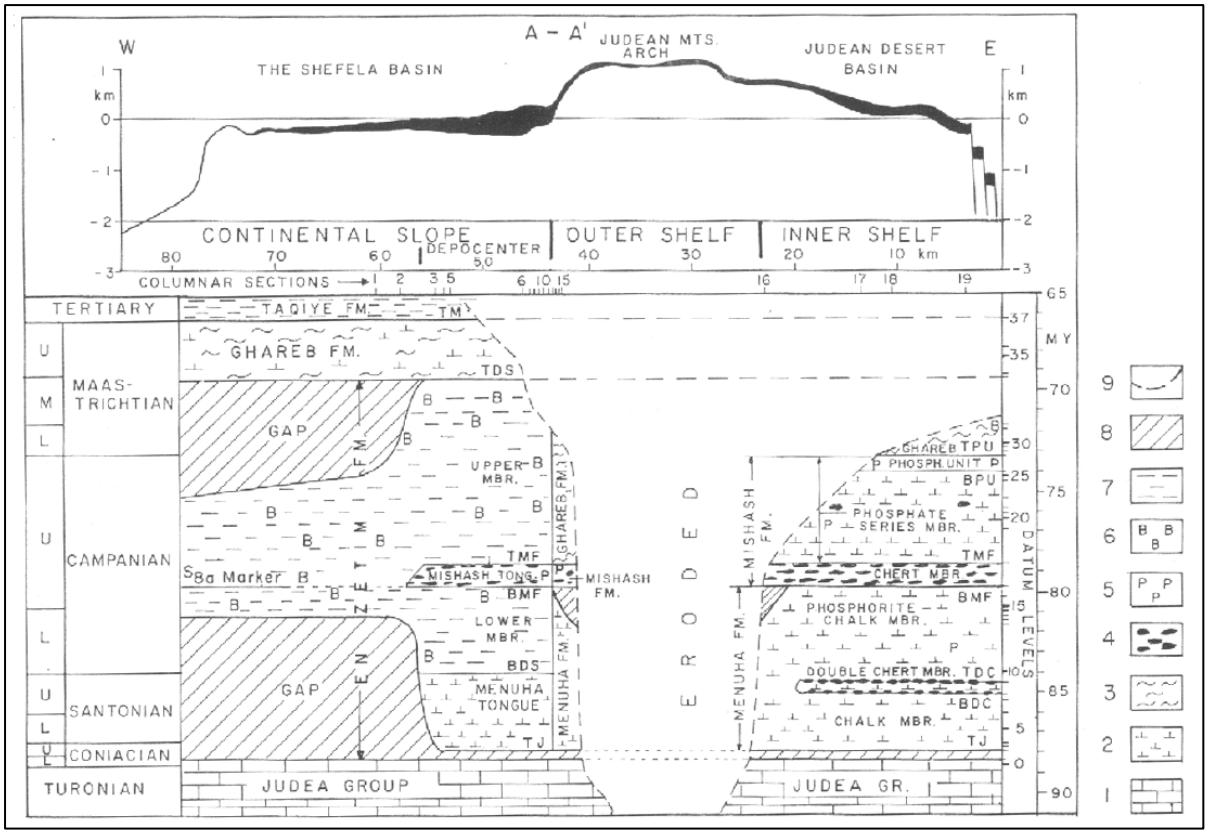

Figure 2: East-West structural and stratigraphic sections across central Israel. The west section describes the Shefela basin. Legend: 1, limestone; 2, chalk; 3, marl; 4, chert; 5, phosphatic; 6, bituminous; 7, shale; 8, internal gaps; 9, outline of present day erosion (Gvirtzman et al., 1989).

1.3 Research plan

A comprehensive testing program was conducted on core samples extracted from the Aderet borehole drilled by IEI ltd. Most of the measurements were done in the Rock Mechanics Laboratory of the Negev at BGU as follows:

1. Unconfined, Triaxial and Hydrostatic compression tests were performed using a hydraulic, stiff, closed-loop servo controlled triaxail system manufactured by TerraTek Inc. The results of these measurements include the static elastic constants, intact compressional strength under unconfined and confined conditions, cohesion and internal friction angle.

2. Brazilian tensile strength was measured using a manual, hydraulic, mini-load frame manufactured by ELE systems Inc. (SBEL model PLT-75). By measuring the tensile strength parallel and perpendicular to the bedding direction, mechanical anisotropy was examined.

3. Porosity, permeability and Klinkenberg slip factor were measured before and after thermal conversion of kerogen by pyrolysis and release of the liquid and gas products. These

properties were determined with an unsteady state gas permeameter & porosimeter device manufactured by Vinci technologies. In addition, anisotropy was examined by measuring the permeability parallel and perpendicular to the bedding direction.

Two additional tests were performed at the organic geochemistry laboratory at BGU:

4. Pyrolysis experiments, under different pressure and temperature conditions, were performed using a pressure vessel manufactured by Parr Instruments Inc.

5. Total organic carbon (TOC) values were determined on a LECO SC632 device.

This thesis is divided into seven chapters. Following this first introduction chapter, a general background on the origin and distribution of oil shale worldwide and more detailed on the Shefela deposit is given in Chapter 2. Later, the petrophysical and mechanical parameters of oil shale deposits from around the world, as described in previous studies, are summarized. The research methods are described in Chapter 3 and the results are provided in Chapter 4. In Chapter 5 and 6, the mechanical and petrophysical behavior is discussed, and important correlations and conclusions are obtained. Finally, the main conclusions from this research and suggestions for future research are summarized in Chapter 7.

Chapter 2- General Background

2.1 Oil Shale

2.1.1 Definition

Oil shale is a fine-grained sedimentary rock containing relatively high concentration of organic matter, mainly a solid material known as ‘kerogen’, a complex macromolecular structure that is insoluble in common organic solvents and considerably smaller bituminous fraction which is soluble in organic solvents. It has the potential to yield substantial amounts of oil and gas upon thermal maturation, natural or induced. Oil shale have been deposited in a variety of depositional environments where the combination of primary production and preservation conditions were favorable for organic matter accumulation in the sediments from Precambrian to Tertiary worldwide. The organic matter in oil shale is composed primarily of carbon, hydrogen, oxygen, and small amounts of sulfur and nitrogen. The organic matter is mixed with varied amounts of fine-grained mineral matter. The composition of the inorganic fraction may vary from shale where clay minerals are predominant, such as the Lower Jurassic shales of Western Europe (particularly France and West Germany), to carbonates with subordinate amounts of clay and other minerals, such as the Green River shales of Colorado, Utah and Wyoming (Tissot and Vandenbroucke, 1983). The mineral inorganic fraction typically consists of about 60-90% of the oil shale, whereas smaller amounts (40% and less) are referred to as coals. Organic matter in oil shale can include the remains of algae, spores, pollen, plant cuticle and corky fragments of herbaceous and woody plants, and other cellular remains of lacustrine, marine, and land plants. When compared with the classification established for petroleum source rocks, kerogen of the oil shale most frequently belongs to type I or II. There is no oil and little extractable bitumen naturally present in the rock (Tissot and Welte, 1984; Dyni, 2003).

The thermal maturity of oil shale refers to the degree to which the organic matter has been altered by geothermal heating. If the oil shale is heated to sufficiently high temperatures, the organic matter can decompose and release hydrocarbons (oil and gas). Usually oil shale thermal maturity level is relatively low and it still retains the potential for hydrocarbon generation upon thermal maturation. However, oil shale that was buried deep enough and exposed to sufficient heating can become source rocks for petroleum and natural gas (Dyni, 2003). Hutton (1987) adapted petrographic terms from coal terminology and developed a

classification of oil shale, based primarily on the origin of the organic matter. He visualized the oil shale as one of three broad groups of organic-rich sedimentary rocks: (1) humic coal and carbonaceous shale, (2) bitumen-impregnated rock, and (3) oil shale. He then divided oil shale into three sub-groups based upon their environments of deposition: Terrestrial, lacustrine, and marine. The hydrocarbon yield potential of oil shale is a function of the organic matter content and chemical composition, which is determined primarily by the type of organic matter assemblages and depositional and diagenetic environments (Figure 3).

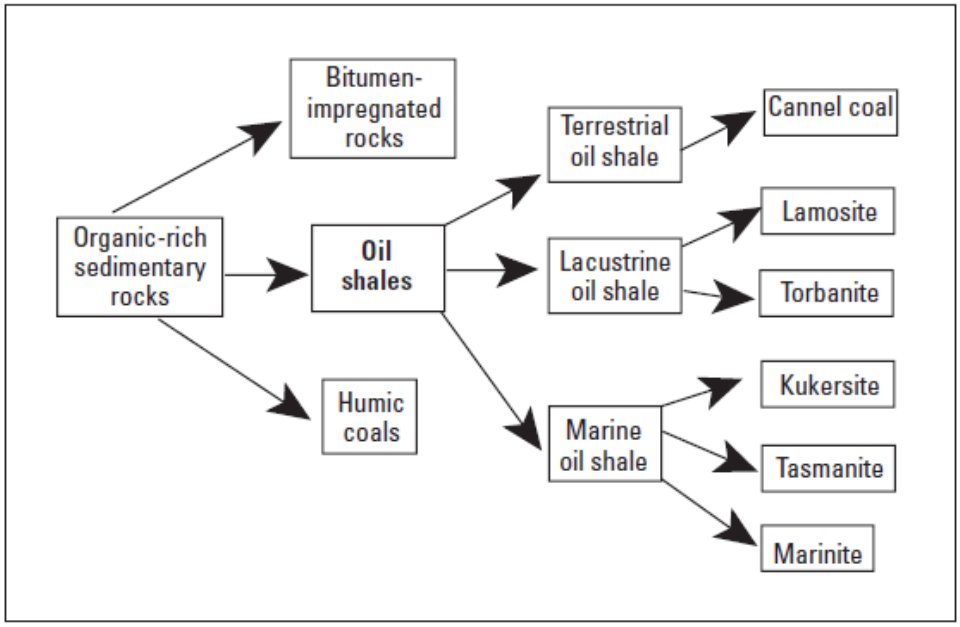

Figure 3: Classification of oil shale (Hutton, 1987).

Shale Oil and gas are generated from immature oil shale during pyrolysis, a treatment that consists of heating the rock to induce thermal maturation of the organic matter and generate hydrocarbons. The grade of oil shale is determined by measuring its potential to yield oil through a standard laboratory retort conditions (e.g. "modified Fischer assay")' and is commonly used in the United States. The grade of oil shale is usually expressed in liters of shale oil per metric ton (l/t) of rock, where 100-200 l/t represents high quality grade and 25-45 l/t is considered as the lower limit for economic potential (Dyni, 2003; Minster, 2009).

2.1.2 Distribution in the world

Oil shale deposits in the world range in size from small occurrences to enormous masses that occupy thousands of square kilometers and in age from Precambrian to Tertiary. Well-explored oil shale deposits, that are being mined or have the best potential for development because of their volume and grade include the Green River deposits in the western United

States, the Tertiary deposits in Queensland, Australia, deposits in Sweden and Estonia, the El-Lajjun deposit in Jordan, and deposits in France, Germany, Brazil, China, Canada, Turkey and Russia. It is expected that these deposits would yield at least 40 liters (0.25 bbl) of shale oil per metric ton of shale, using the Fischer Assay (Dyni, 2003; Altun et al., 2006). According to the 2010 World Energy Outlook by the International Energy Agency, the world oil shale resources may be equivalent of more than 5 trillion barrels (790×10^9 m^3) of oil in place of which more than 1 trillion barrels (160×10^9 m^3) may be technically produced (IEA, 2010). As the supply of petroleum diminishes and its costs increases, oil shale deposits that occur worldwide and their vast amounts become a promising option as a potential resource for oil production (including in-situ) or as a solid fuel supplement. In light of the above, the research of the different aspects of oil shale deposits is necessary for potential production planning.

2.2 Physical and mechanical properties of oil shale deposits worldwide

The purpose of this section is to describe the petrophysical and mechanical parameters of oil shale, as have been reported in previous studies. Despite the abundance of oil shale deposits in the world, little work has been published on their petrophysical and mechanical parameters properties. The majority of the data comes from the US deposits in the Green River and Antrim Formations (Eseme et al., 2007) and the Canadian deposit in the Kettle Point Formation (Dusseault and Loftson, 1985). Other studies focus on oil shale from Germany, Australia and Turkey (Eseme et al., 2006a; Eseme et al., 2012).

Microstructure, mineralogy and organic content are highly variable in oil shale occurring worldwide, making large discrepancies in their properties. Therefore extrapolation of the existing data to other oil shale worldwide is possible only in qualitative terms. Most studies on the oil shale behavior are accompanied by an indication of organic matter content.

2.2.1 Petrophysical properties

Petrophysical properties such as porosity and permeability strongly depend on the rock pore size and shape, and the link between them. In oil shale these properties also depend on the organic matter content. Low porosity is usually associated with high organic matter content, but mineral composition and diagenetic processes also have an effect. Intergranular permeability of oil shale is mostly very low, due to very small pore sizes (Eseme et al., 2007). Eseme et al. (2006) studied the relative significance of extrinsic (axial stress and temperature) and intrinsic (mineralogy and organic matter) factors during compaction of mudstones. Also,

they examined the relation between compaction (volume change) and porosity (void ratio) (Eseme et al., 2006). In that study, series of measurements have been performed on samples from the Posidonia and the Messel oil shale from Germany, the Himmetoglu oil shale from Turkey, the Torbanite oil shale from Australia and the Condor oil shale from Australia. The depositional environments were shallow marine for the Posidonia shales and Lacustrine for the rest. The samples textures were micro-laminated to massive but not fissile. The bulk density values ranged from 1.14 g/cm^3 for the Australian Torbanite to 2.1 g/cm^3 for the South Posidonia with slightly higher grain densities all consistent with their total organic carbon (TOC) contents, which varied from 9.66 wt% in South Posidonia to 51.33wt% in the Australian Torbanite. The carbonate content calculated from total inorganic carbon (TIC) contents ranged from 1.5 wt% in the Australian Torbanite to 24.2wt% in South Posidonia in agreement with their deposition in lacustrine and shallow marine environments, respectively. Porosity values of the oil shale samples as were determined by mercury porosimetry ranged from 7.6% in the Australian Torbanite to 20.13% in Himmetoglu.

In a recent study, Eseme et al. (2012) studied the evolution of porosity, specific surface area and intergranular permeability during high temperature compaction tests. The intergranular permeability of samples was assessed in two ways. Two samples (south Posidonia and Messel) were subjected to steady-state permeability tests and their absolute permeability determined using the Darcy's single phase flow equation. The permeability coefficients for south Posidonia and Messel were in the nanodarcy range: 2.6 x 10^{-21} m^2 and 0.72 x 10^{-21} m^2, respectively. The Kozenye-Carman equation was used to estimate permeability coefficients from measured porosity and specific surface area values of the samples before and after the compaction tests. The values of calculated permeability from the Kozenye-Carman equation for the pre-deformation samples ranged from 6.82 x 10^{-24} m^2 to 5.27 x 10^{-21} m^2. For the post-deformation samples, the calculated permeability coefficients ranged from 2.21 x 10^{-22} m^2 to 4.79 x 10^{-21} m^2. From both measured and calculated permeability coefficients oil shale have low permeability coefficients in the range from 10^{-18} to 10^{-24} m^2 (Eseme et al., 2012).

Low permeability values of oil shale also reported from the Antrim formation, where average permeability values range from 0.123 - 0.025 millidarcies (10^{-16} to 10^{-17} m^2) parallel to bedding planes and 0.044 - 0.004 millidarcies (10^{-17} to 10^{-18}m^2) perpendicular to bedding planes (Dusseault and Loftson, 1985).

The relation between grain density and volume fraction of organic matter for six oil shale (Australian Torbanite, Posidonia, Messel, Himmetoglu and Condor) studied by Eseme et al. (2006b) is described by a linear equation (Figure 4): Oc = 113.94 – 40.5 ρ_m, where Oc is the

volume fraction of organic matter (in %) and ρ_m is the grain density in g/cm^3. This relation is only valid for the oil shale investigated, because it also depends on density and fraction of inorganic minerals (mostly 2-3 up to 5 g/cm^3) as well as density of kerogen (1.0-1.3 g/cm^3), density of oil generated (0.7-0.9 g/cm^3), porosity (very low to over 30%) and conversion efficiency of kerogen depending on retorting process (Oil shale containing type II kerogen may lose upon complete conversion about 50 wt%). Generally, both bulk and grain density decrease with increasing organic matter volume.

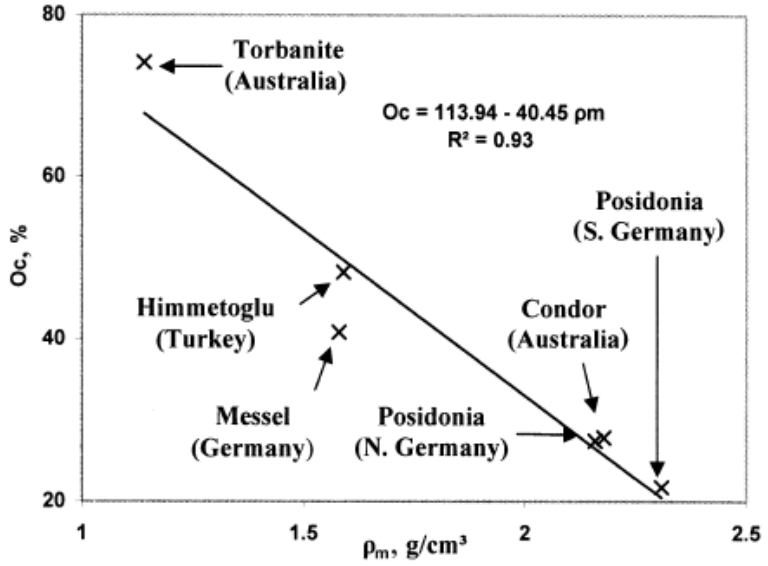

Figure 4: Grain density versus organic matter volume for six oil shale (Eseme et al., 2006).

2.2.2 Mechanical properties

According to the review on the mechanical properties of oil shale (Eseme et al., 2007), at room temperature, most oil shale are hard and brittle with mechanical properties that are pressure-dependent and only weakly rate-dependent. Mohr-Coulomb- type constitutive equations are used commonly to evaluate mechanical properties at room temperature. The response to stress is correlated to grade, with ductile behavior becoming more apparent as grade increases.

Samples of oil shale that have been loaded in different directions showed transverse isotropy. Tensile strength is lowest perpendicular to bedding due to lamination. It correlates with grade and decreases with increasing organic content. Mechanical properties of oil shale at room temperature from different deposits worldwide are summarized in Table 1.

Based on published measurements from the Western US oil shale (Eseme et al., 2007), the properties strongly correlate with grade except for cohesion and tensile strength. Unconfined compressive strength decreases with decreasing loading rate while Young's modulus increases non-linearly with increasing confining pressure. The unconfined compressive strength and Young's modulus decrease with increasing grade whereas Poisson's ratio shows an increase with grade at room temperature. The grain density, the unconfined compressive strength, the Young's modulus and the Poisson's ratio also show variations that are not related to variations in grade but reflect differences in composition and geologic history. Variations in the data from sub-samples of the same oil shale that are not related to grade are presumably due to variation in the properties (heterogeneity) of the organic matter.

Eseme et al. performed in their study (Eseme et al., 2006) series of deformation experiments including unconfined compressive strength (UCS) tests. Most of the samples exhibited brittle failure, while the brittle behavior decreased as organic matter content in the samples increased. The strength of samples (σ_c) at room temperature ranged from 5.3 MPa for Messel up to 70 MPa for north Posidonia. The axial strain values ranged from 1.9% in north Posidonia to 23% in Torbanite and showed strong correlation to the ultimate strength. The Young's modulus (E) ranged from 0.08 GPa in Messel to 3.5 GPa in north Posidonia and was consistent with the strength data.

The Kettle point oil shale (Dusseault and Loftson, 1985) differs from the Western US Green River Shale in the small amount of carbonate minerals present. It is geologically and lithologically similar to the Michigan Antrim shale, which is very fine grained, laminated shale, composed dominantly of clay minerals and organic matter, pyrite and carbonate. The total organic content ranges from 0.2-15.4 wt%, with an average of 7.7 wt%.

The Brazilian tensile strength of the Kettle point oil shale, ranges from 5.1-16.5 MPa. Dusseault et al. (1985) showed that the tensile strength is influenced significantly by the mineral matter and to a much lesser degree by the organic content. Water contents of the samples ranged from 0.7-2.2% and the data indicated that variations in moisture content had no effect on the results with reservations due to very narrow range of values. Uniaxial compressive strength ranges from 59-100 MPa and, like the Brazilian tensile strength, is mainly influenced by the mineral content and not by the organic content. In triaxial compression the compressive strength increased with increasing confining pressure.

Table 1: Summary of mechanical properties of oil shale worldwide at ambient conditions. Data from ((Dusseault and Loftson, 1985; Eseme et al., 2006; Eseme et al., 2007; Eseme et al., 2012).

Property/ Deposit	Western US		Kettle Point (Canada)	Posidonia (Germany)	Himmetoglu (Turkey)	Torbanite (Australia)	Condor (australia)	Messel (Germany)
Depositional environment	Lacustarine [Org.C vol. 20%]	Lacustarine [Org.C vol. 50%]	Marine	Shallow marine	Lacustarine	Lacustarine	Lacustarine	Lacustarine
Description			Dark-grey to black-laminated	Grey-micro laminated	Brown-macro laminated	Black-massive	Brown- micro laminated	Dark-grey macro-laminated
Organic carbon content (vol %)	20	50						
Organic carbon content (wt %)			0-20	9.66-12.07	31.3	51.33	12.61	20.33
Oil yield (l/t)	63	210						
Grain density (g/cm3)	2.4	1.8		2.16-2.31	1.59	1.1	2.18	1.58
Porosity (%)	0	0	1.2-3.4	8.14-12.53	20.13	7.6	16.2	16.19
Young's modulus (GPa)	16±2	4.5±0.5	5.9-10.1	1.57-3.5	0.72	0.61	0.78	0.08
Poisson's ratio	0.2	0.35	0.19-0.29					
Uniaxial compressive strength (MPa)	125±25	50±30	59-100	62.96-70	57.7	49	47	5.3
Triaxial compressive strngth (MPa)			$\sigma 3$=1.7-20.7, $\sigma 1$=85-164					
Friction angle (°)	40.5±0.5	20	20-36					
Cohesion (MPa)	28±7	28±7	22-26					
Tensile strength (MPa)	13±1	9.5±1.5	5.1-16.5					
Permeability parallel to bedding planes (mD)			0.025-0.123					
Permeability normal to bedding planes (mD)			0.004-0.044					

2.3 Oil shale deposits in Israel

About thirty deposits of Late Cretaceous sub-basins containing organic-rich carbonates were described in a GSI report (Minster, 2009) on the geology of the Israel oil shale resources (Figure 1). The first reported domestic oil shale occurrences are at Nabi Musa where exposed rocks were used for centuries as heating material, and En Boqeq which was studied in the 1950's. Other occurrences were first noted in boreholes for mineral, water, and oil exploration. The Mishor Rotem deposit and many other oil shale occurrences in the northern and central Negev were discovered during prospecting for phosphate. During the late 1970's and into the 1980's, prospecting was carried out specifically for oil shale in various locations of the northern Negev.

The kerogen of the Israeli oil shale is mainly type IIs (Spiro, 1980). The deposits extend over approximately 15% of Israel's area, mainly in the northern and central parts of the country, where the total reserves are estimated to be larger than 300 billion tones. In several localities in central and southern Israel, the organic matter-rich sequences reach 200-400 m, and in certain thick sections represent a major portion of the Mount Scopus Group. The oil shale member of the Ghareb Formation is ~20 m thick at the type section in Giv'at Mador, southwest of Oron (Shahar et al., 1968) and reaches a maximum of ~130 m in Mishor Rotem (Minster, 2009). It is characterized by a gradual decrease in the organic matter content from the base of the sequence upwards. The total organic content (TOC) is about 16% in the base of the Ghareb Formation.

Below the Ghareb Formation, within the Mishash Formation a 5 m to 12 m thick section is found with lower organic content in chalky and siliceous host rocks. Such sections were found in Mishor Rotem, Mishor Yamin, Oron, Nahal Zin, Biq'at Zin.

Thicker and sometimes richer oil shale sequences of the Mishash formation are indicated from some localities in the Negev. In several places of the Northern Negev (e.g., Hatrurim, Biq'at Zin) chalky sections of the Menuha formation that underlies the Mishash formation, were found to be enriched in organic material as well.

The deposits that are associated with the Mount Scopus Group are found in synclinal structures. These structures contributed to the preservation of the organic matter, as well as the global anoxic event of the Upper Cretaceous (Minster, 2009). Carbonates like chalk, marl and limestone comprise the mineral constituents of the oil shale, while the organic component is dispersed in the matrix or micro-laminated.

2.3.1 The Shefela deposit

The Shefela basin, found in the Shefela and the East coastal plain areas of central Israel, is the largest of the oil shale bearing basins in Israel and among the largest in the Levant. It extends across more than 1000 km^2 and contains the thickest oil shale succession, estimated at 100-500 m (Gvirtzman et al., 1985; Minster, 2009; Burg et al., 2010). The resource was estimated at 300-350 billion tons of mainly organic rich carbonates (Minster, 2009).The section enriched with organic matter is part of the Mount Scopus group. The thickness of Mount Scopus group varies due to the folding and subsidence of the synclinal basins during its sedimentation, resulting in asymmetric synclinal structure at the Shefela basin. The organic rich succession in the Shefela basin accumulated on the continental slope, marginally to the main upwelling center for a duration of about 10 m.y between middle Campanian and late Maastrichtian, is the longest known organic-rich deposition in all of the Levant (Almogi-Labin et al., 1993; Eshet et al., 1994).

Following Gvirzman et al. (1989) the main units of the Mount Scopus group in the basin from top to bottom are (Figure 2):

- Taqiye: gray to yellowish chalky shale, 20-140 m. Underlies the Adulam Fm. (silicified chalks and chert) with a 5-10 m transition zone.
- Ghareb: relatively hard light yellowish chalk, 10-30 m. Exposed on the east flank.
- En Zetim: dark brown bituminous calcareous shales with a brown chert intercalation in the east. The upper member: rich in organic matter, 20-280 m. The middle member: (the Mishash tongue) brecciated brown chert with thin beds of phosphorite and interlayered porcelanite, 0-15 m, exposed in the Hebron monocline and extends westwards 5-10 km in the subsurface. The lower member: harder, lighter, less bituminous chalk than the upper En Zetim sequence, 20-200 m. Found in the depocenter of the basin.

The material for this study consists of cores drilled by IEI Ltd in the exploration permit area inside the synclinal Shefela basin (Figure 5). Five boreholes were drilled: Aderet, Beit-Guvrin, Lachish, Gal'on and Zoharim. This research focuses on the oil shale succession in the Aderet borehole ranging from a depth of 265 to 600 meters.

Burg et al. (2010) have adopted the conventional Negev division to the stratigraphic units of Mount Scopus group in the Shefela region, namely the section consists of four formations:

Menuha formation of the Santonian, Mishash formation of the Campanian, Ghareb formation of the Maastrichtian and Taqiye formation of the Paleocene- lower Eocene. The main implications of the adoption of this division are that the oil shale unit includes the Ghareb and the Mishash formations where the Mishash formation includes not only the "Mishash tongue" (about 20m thick chert and phosphorite unit) (Gvirtzman and Reiss, 1965) but also the thick chalky section above and below.

Following the geological investigation of the site by Burg et al. (2010) in this research the section is divided to Ghareb (265 m- 460 m) upper Mishash (460 m-530 m) above the "Mishash tongue" (530 m-537 m) and lower Mishash below it (537 m-600 m). The section division that is used in this study and the division by Gvirtzman (Figure 2) are shown in Figure 6.

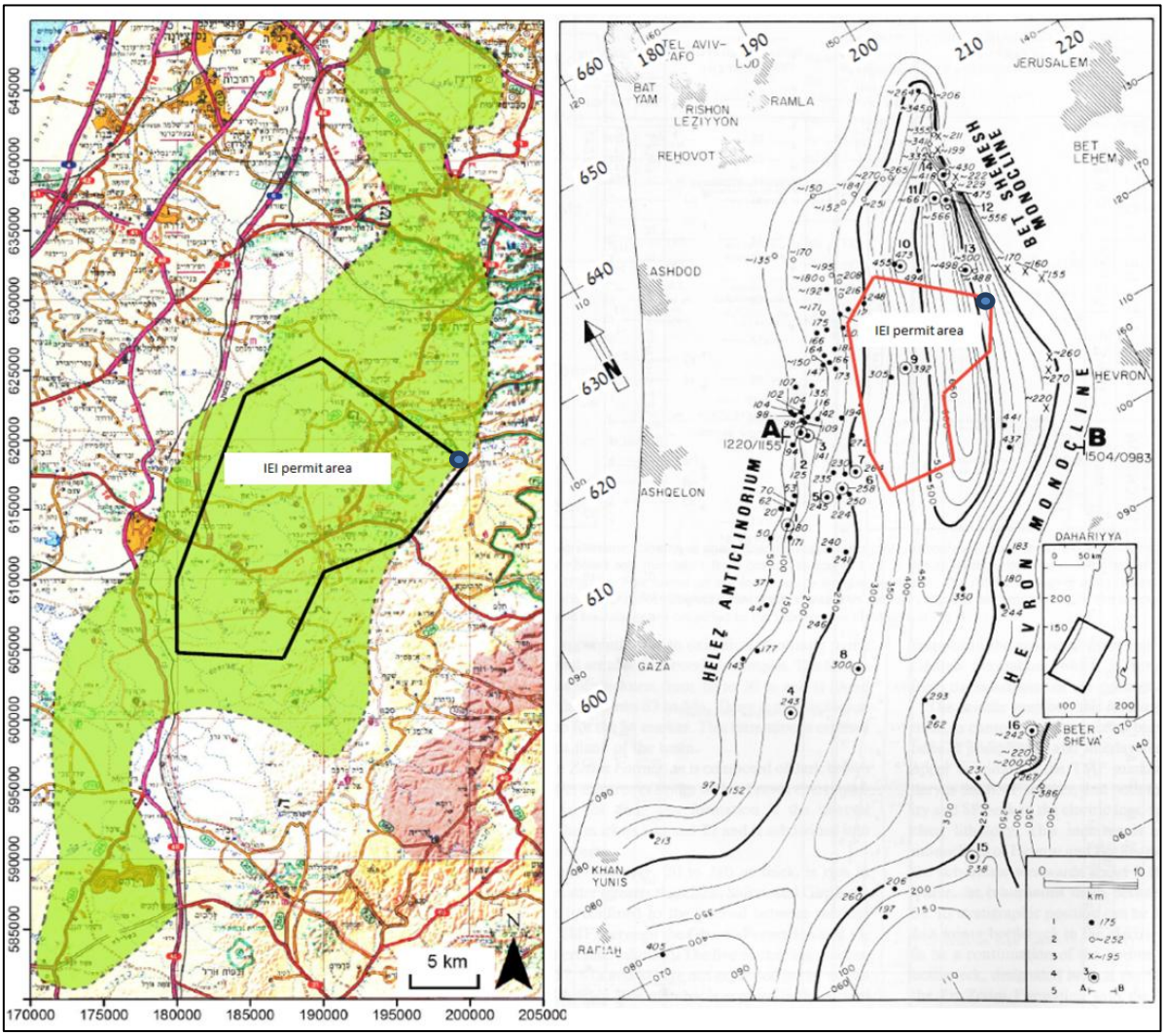

Figure 5: To the Left- The Shefela oil shale deposit (Minster, 2009). To the right- isochore map of the Mount Scopus Group in the Shefela basin (Gvirtzman et al., 1985). The polygon in both figures represents the IEI exploration permit area (Burg et al., 2010) and the blue dot is the Aderet borehole (199339/617813).

The oil shale unit shows vertical lithological uniformity at the Ghareb formation and in transition to the upper Mishash formation. It consists of mostly dark brown bituminous chalk, rich in organic matter and large visible fossils, accompanied by thin marl beds in places, some phosphate and small pyrite crystals. There are hardly any open fissures and no visible bedding. The "Mishash tongue" appears as a thin layer of chert, bituminous chalk and phosphate. Below it, the bituminous chalk becomes brighter with depth, indicating the decrease in organic matter; silicification can be noticed (Burg et al., 2010).

Depth (m) *		Gvirzman et al. (1989)		Negev Division adopted by Burg el al. (2010) and by this study	
	Age	Formation	Lithology Description	Formation	Lithology Description
265	Upper Cretaceous: Senonian	En Zetim	Dark brown bituminous calcareous shales, rich in organic matter	Ghareb	Hard brown bituminous chalk, with dark laminas of organic matter, high amount of micro and visible fossils, small presence of phosphate **
460				Upper Mishash	Dark very rich bituminous chalk, very hard and heavy, rich with micro fossils
530		Mishash (tongue)	Brecciated brown chert with thin beds of Phosphorite and interlayered porcelanite	Mishash (tongue)	Interchanges of dark hard chert with bituminous chalk
540		En Zetim	Harder, brighter and less bituminous chalk	Lower Mishash	Hard light gray chalk, bituminous smell decreasing with depth
600					

Figure 6: A columnar schematic section of the studied material; * the depths division represents the Aderet Borehole, the same division is used for the schematic section of Gvirtzman et al. (1989); ** the transition from Ghareb to upper Mishash formations shows lithological uniformity.

The main chemical components of the oil shale from the Aderet borehole are presented in Figure 7: Aluminum oxide (Al_2O_3) that represents the clay component, calcium oxide (CaO) that represents the calcite component, phosphorus pentoxide (P_2O_5) that represents the phosphate component and sulfur trioxide (SO_3) that stands for the kerogen, the gypsum and the pyrite. Only 1% of the sulfur content is found in the inorganic constituents and 50-80% of the sulfur originates from the organic matter. The calcium is the main inorganic component, the calcite ($CaCO_3$) being the most common mineral in the oil shale (41-73% of the rock) (Burg et al., 2010).

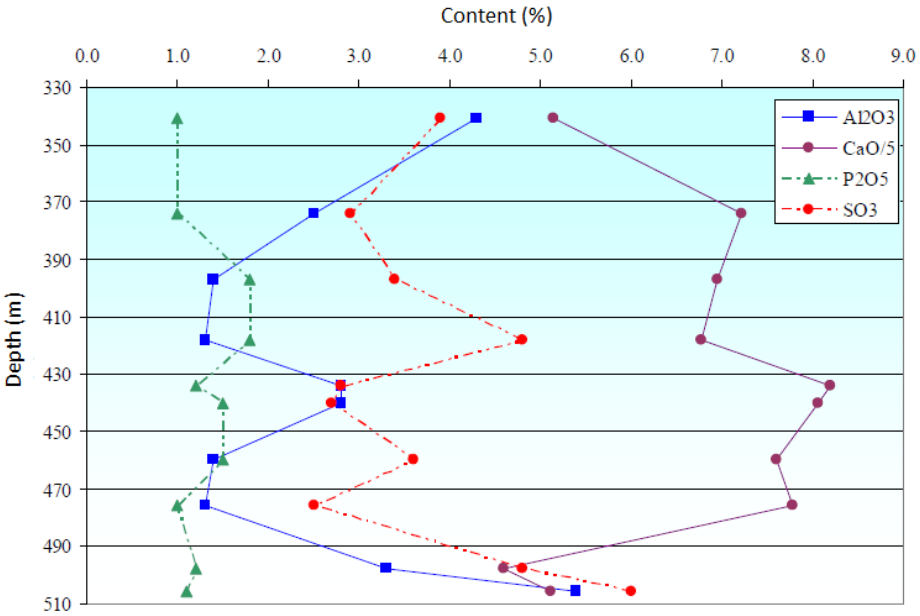

Figure 7: Main chemical components content distribution with depth (Burg et al., 2010).

The distribution of the total organic carbon content (TOC) in the Aderet borehole, as was measured at the BGU geochemical lab by LECO SC632, is shown in Figure 8. The measurement was taken every 1 meter. The TOC values average 15% in the middle of section (350-450 m) and decrease upwards and downwards.

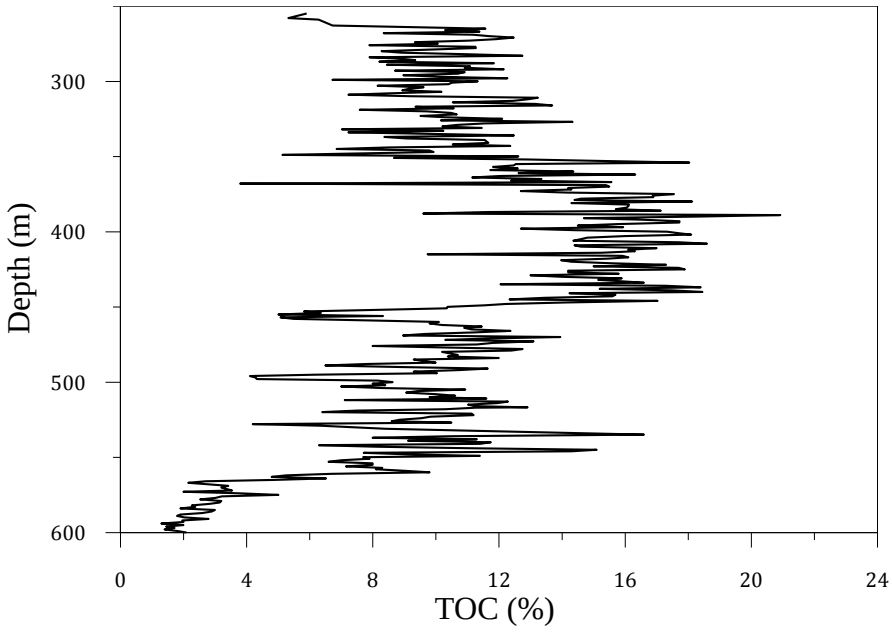

Figure 8: Total organic carbon distribution with depth at the Aderet borehole (data from IEI Ltd.)

Chapter 3- Research Methods

This chapter introduces the methods and the instrumentation used in this work.

All tests were performed at ambient temperature. The geometrical properties of all tested samples are listed in Appendix 1.

3.1 Sample Preparation

3.1.1 Sampling for mechanical and petrophysical measurements

The cores from Aderet borehole were brought to BGU's Geological department sample preparation lab. Each core, length of ca. 100 cm and diameter of 8.4 cm, was originally wrapped in plastic wrap and sealed in plastic tube. During the sample preparation, the sample ends were ground to roughness smaller than 0.01mm.

The oil shale proved to be extremely fragile with a tendency to separate across microscopic bedding plane partings. Heating the material seems to aggravate this problem. When drying was necessary (for petrophysical tests), slow rate of heating was applied- starting with 60°C the temperature was manually increased to 110°C during few hours and then was kept constant for 24 hours (this period of time was chosen after it was noticed that after 24 hours there is no change in the sample's weight, therefore, it was considered to be dry).

The dimensions of the samples prepared vary depending on the required test according to ASTM standards:

1) For the different compression tests, including: hydrostatic compression, uniaxial compression and triaxial compression, 2.12" (54 mm) diameter (NX size) and 42.5" (108 mm) length solid cylinders were prepared. The samples were drilled with their long axis in direction normal to bedding simulating correctly the principal loading direction in the field, such that mechanical test results (Elastic parameters and strength) will be applicable to this direction only. It is reasonable to assume however that the material does possess some inherent anisotropy due to sedimentary bedding. The measurement output from two radial strain transducers mounted on the sample in parallel to the bedding direction will allow determination of transverse isotropy within the bedding plane direction.
2) For Brazilian tests, 2.12" (54 mm) diameter (NX size) and 1.06" (27 mm) length solid cylinders were prepared. These were drilled parallel and perpendicular relative to the

bedding direction. Part of the samples was oven dried at a temperature of 110°C for different periods of time to obtain moisture content diversity.

3) For the porosity and permeability tests, 1" (25.4 mm) diameter and 1" (25.4 mm) length core samples were prepared.
   These samples were oven dried at a temperature of 110°C for 24 h.

3.1.2 Sampling for TOC measurements

Few grams of each sample that was destructively tested were ground and measured for determining the total organic carbon (TOC) at the geochemical laboratory, whereas the samples that were not destroyed during experiments were sampled for TOC from the same core, next to the drilled sample while originally preparing it.

3.2 Compression experiments

The most common method of studying the mechanical static properties like stress-strain behavior, strength, elasticity, effect of confining and hydrostatic pressure etc. is by applying different compression tests.

The compression experiments were performed using triaxial testing system manufactured by TerraTek, model FX-S-33090 (Figure 9- right). The stiff load frame operates using a closed-loop, servo controlled hydraulic system of maximum axial force of 1.4 MN, stiffness of $5x10^9$ N/m, and confining pressure capacity of 70 MPa. Control can be achieved using either load or displacement monitoring. Unconfined and triaxial compression tests were run at constant strain rate of $1x10^{-5}$ sec^{-1}.

Several displacement sensors are updating the servo controlled system:

1. Piston displacement is being monitored using a high sensitivity LVDT (Linear Variable Differential Transformer) located outside the vessel near the piston.

2. Load is being measured by a sensitive load cell located in series with the sample stack having a maximum capacity of 1000 KN and linearity of 0.5% full scale.

3. Sample axial (ε_a) and radial strains (ε_{r1}, ε_{r2}) are being recorded using four arm axial and four arm transverse strain cantilever sets (Figure 9-left), where arm deflection is calibrated to displacement (calibration has been performed prior to the test). The axial cantilever set has a 10% strain range and the radial strain cantilever has a strain range limit of 7%, with 1% linearity full scale for both sets.

Prior to testing, each sample was wrapped by a shrink tube to isolate it from the pressure vessel oil.

The samples were tested at natural water content conditions (after the processes of drilling and grinding which involved use of water). Water content for each sample was determined by weighing it immediately after the test, drying at 110 °C in the oven for 24 hours and weighing it again. The water content (ω) was calculated using the following expression:

$$\omega = (w_b - w_d)/w_d \cdot 100\% \quad (1)$$

where w_b is the bulk weight of the sample and w_d is the dry weight of the sample.

Figure 9: To the right, 1.4 MN stiff load frame and 70 MPa confining pressure vessel located at the Rock Mechanics Laboratory of the Negev. To the left, the four arm radial and axial strain cantilever gauge system.

3.2.1 Stress-strain behavior in compression

In discussing the deformations of rock undergoing compression from various directions, it proves useful to divide the stresses into two parts: Hydrostatic stresses that are compressions equally applied in all directions and Deviatoric stresses that consist of normal and shear stresses that remain after subtracting a hydrostatic stress from each normal stress component. The strong motivation for this division is the fact that deviatoric stresses are those that produce distortion and destruction while non-deviatoric (hydrostatic) stresses generally do not (Goodman, 1989).

As can be seen in Figure 10, with initial application of the deviatoric stress, fissures and some pores begin to close, producing an inelastic, concave-upward stress-strain section. This is followed, at point A, by linear relationships between axial stress and axial strain and between lateral stress and lateral strain. At point *B*, the rate of lateral strain begins to increase relative to the rate of axial strain (Poisson's ratio increases) as new cracks begin to form inside the most critically stresses portions of the specimen. In the region between stress *B* and stress *C*, cracks are considered to be "stable" meaning that with each increment of stress they grow to a finite length, and then stop growing. After point *C*, cracks that form propagate to the edges of the specimen and a system of intersecting, coalescing cracks is developed, which eventually form a semicontinuous rupture surface termed a "fault". The peak load, point *D*, is the usual object of failure criteria. If the volumetric strain is plotted against the deviatoric stress as in Figure 10b, it is seen that the attainment of the crack initiation stress (*B*) is marked by the beginning of an increase in volume associated with sliding and buckling of rock slivers between cracks and opening of new cracks. At a stress level corresponding to stress point *C*, the specimen may have a bulk volume larger than at the start of the test. This increase in volume associated with cracking is termed dilatancy (Goodman, 1989).

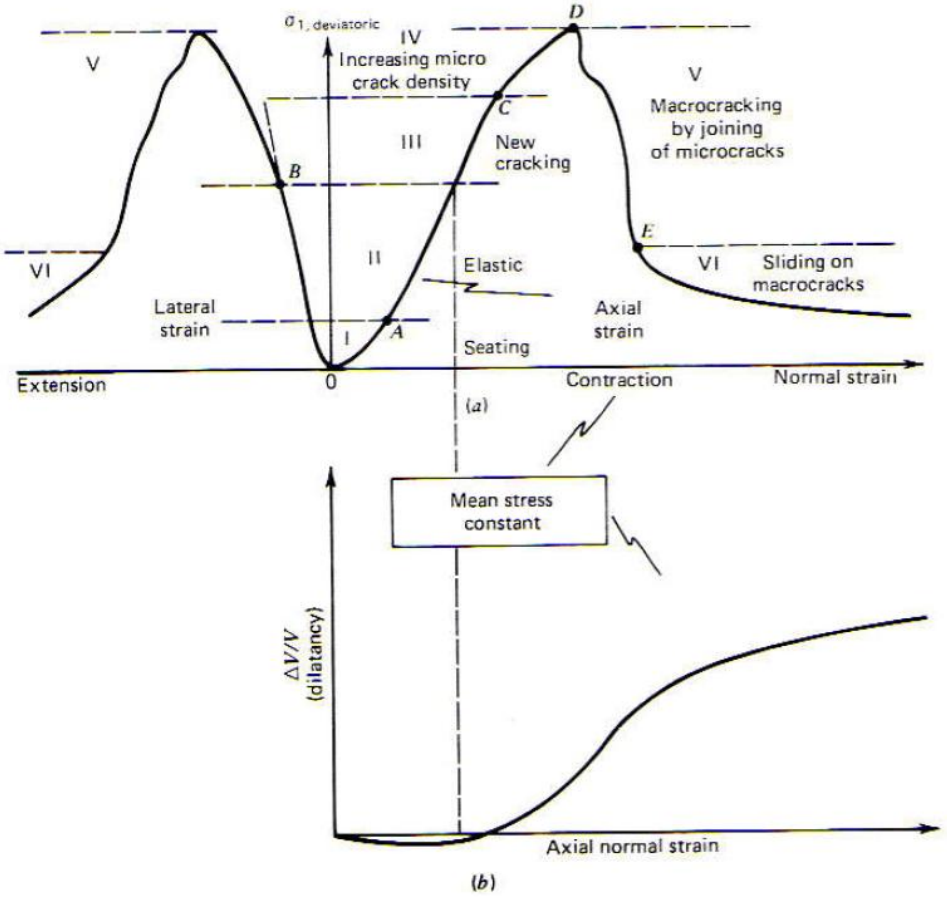

Figure 10: Deformation under increasing deviatoric stress, with constant mean stress (hypothetical curves). (a) Axial and lateral normal strain with increasing deviatoric axial stress. (b) Volumetric strain with increasing axial normal strain (dilatancy) (Goodman, 1989).

Within the research program 8 samples were tested under unconfined compression conditions. The tests were performed under constant strain rate of 10^{-5} s^{-1}. The samples were brought to failure and testing continued beyond peak stress up to 2% axial strain, beyond which unloading was specified. A high data acquisition rate (less than 3 seconds) was used to allow for a data-rich stress-strain curve.

3.2.2 Effect of confining pressure

To study the mechanical behavior under confining pressure, Triaxial compression tests were performed on 7 samples from the same depth interval (335-346 m). During each test, simultaneous compression and axisymmetric confining pressure were applied. This conditions are also describes as Biaxial compression where two of main compression direction are equal to the confining pressure. Each test was performed under initial confining pressure value: 1 MPa, 2 MPa, 3 MPa, 4 MPa, 5 MPa and 10 MPa. The confining pressure

was not kept completely constant during the measurements due to the decrease in the cell volume that contains oil. This was caused by dilation of the sample and entry of the piston into the cell while applying axial compression. The confining pressure pump is manually controlled, so that we were not able to react to the volume changes and maintain the initial values of pressure constant. The samples were brought to failure and testing continued beyond peak stress up to 2% axial strain, beyond which unloading was specified. A high data acquisition rate (less than 3 seconds) was used to allow for a data-rich stress-strain curve.

Under confining pressure, the normal displacement required to move along a jagged rupture path requires additional energy input. That is why most rocks are significantly strengthened by confinement. As the mean applied pressure is increased, the rapid decline in load carrying capacity after the peak load (point D in Figure 10) becomes gradually less striking until, at a value of the mean pressure known as the *brittle-to-ductile transition* pressure, the rock behaves fully plastically (Figure 11). That is, after point D continued deformation of the rock is possible without any decrease in stress. Sometimes "stress-hardening" behavior is observed, meaning that there is actually a strengthening of the rock as it deforms without any "peak stress". The effect of confining pressure is also expressed in changing volumetric strain response as shown in Figure 11b. At successively higher confining pressures, the volumetric strain curves shift smoothly upward and to the right. These curves are the algebraic sum of hydrostatic compression under increasing mean stress (e.g., distance *ac*) and dilatancy under increasing deviatoric stress (*cb*) (Goodman, 1989).

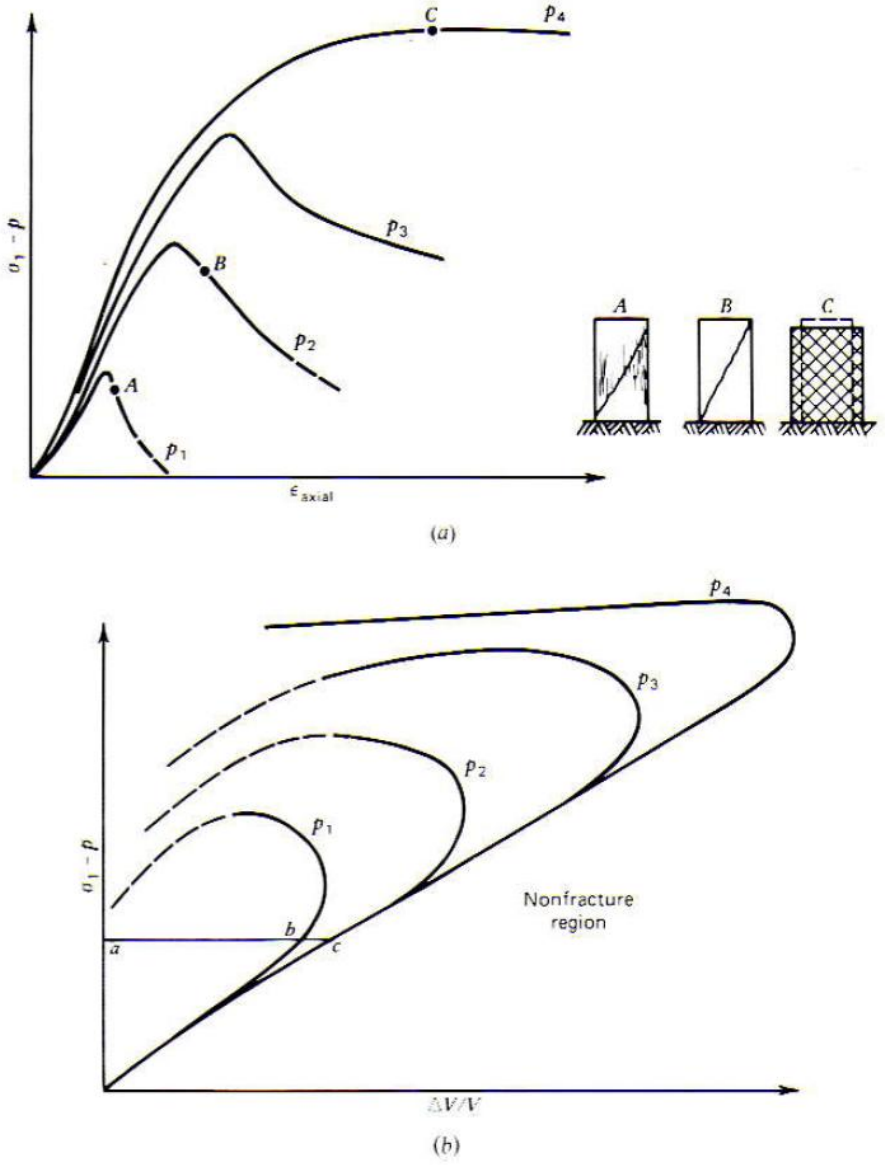

Figure 11: Behavior in triaxail compression. (a) Transition from brittle-to-ductile behavior. (b) Volumetric compression and dilatancy (Goodman, 1989).

The variation of peak stress σ_1 with confining pressure σ_3 is called the rock's criterion of failure (Goodman, 1989). The results of the triaxial measurements were used to fit a failure criterion to the tested material.

The theoretical triaxial strength criteria based on the actual mechanism of fracture do not fit the experimental results properly and to overcome this problem, many empirical criteria have been formulated for rocks. The most commonly used failure criteria are presented next and the adequacy of each criterion to the measurements results is discussed in the discussion chapter.

The Coulomb-Mohr failure criterion

Coulomb- Mohr's classic criterion (Coulomb, 1776) assumes that the strength of the rock is derived from frictional resistance to sliding along inclined planes and the "cohesion" coefficient. In other words, the total shearing resistance of a shear planar fracture which should develop at failure is the sum of the cohesive shear strength (independent of direction) and the product of the effective normal stress and the coefficient of internal friction (a constant independent of normal stress). The inclination of the plane of the shear fracture is a function of the internal friction and it assumed to propagate homogeneously along that plane.

The planar shear fracture is given by:

$$\tau_p = C + \sigma_n tan\varphi \tag{2}$$

Where τ_p is the shear stress at failure, C is the apparent cohesion, σ_n is the normal stress on failure plane at failure and φ is the internal friction of intact rock.

In terms of principal stresses at peak load conditions, the Coulomb-Mohr linear criterion is given by:

$$\sigma_{1,p} = \sigma_c + \sigma_3 tan^2(45 + \frac{\varphi}{2}) \tag{3}$$

Where σ_c is the unconfined compressive strength which equals $2Ctan\left(45 + \frac{\varphi}{2}\right)$, $\sigma_{1,p}$ is the maximum value of major principal stress (peak axial stress) and σ_3 is the minor principal stress (confining pressure).

The Griffith's failure criteria

Griffith suggested that fracture of brittle material (glass) is driven by the concentration of tensile stresses at tips of minute cracks distributes throughout an otherwise isotropic, elastic material. (Griffith, 1921). In extension Griffith found that an elliptical crack of initial length 2c that is perpendicular to the direction of a uniform uniaxial tensile stress σ will extend when:

$$\sigma \geq \sqrt{\frac{2E\gamma}{\pi c}} \tag{4}$$

Where γ is the surface energy per unit area of the crack surface (a fundamental material property) and E is the Elastic modulus of the uncracked material. Griffith extended his theory to the case of applied compressive stresses (Griffith, 1924). He neglected the developed friction on the cracks which will close under compression and assumed that the initial elliptical cracks will propagate from points of maximum tensile stress concentration. He obtained the following criterion for crack extension in plane compression:

$$(\sigma_1 - \sigma_3)^2 - 8T_0(\sigma_1 + \sigma_3) = 0 \;\; if \;\; \sigma_1 + 3\sigma_3 > 0 \tag{5}$$

Where T_0 is the tensile strength. According to Griffith's criterion the unconfined compressive strength σ_c equals $8T_o$; so the criterion can be expressed as following:

$$\sigma_1 = \sigma_3 + \sigma_c \sqrt{\frac{2\sigma_3}{\sigma_c} + 0.25} + 0.5\sigma_c \tag{6}$$

This criterion can also be expressed in terms of the shear stress (τ) and normal stress (σ) acting on the plane containing the major axis of the crack:

$$\tau^2 = 4T_0(\sigma_n + T_0) \tag{7}$$

When σ_n=0, τ=2T_0 which represents the cohesion.

3.2.3 Hydrostatic compression

Two samples were tested under hydrostatic conditions. While loading, hydrostatic pressure was applied to 10 MPa or 30 MPa. Then the load was gradually removed to 0 MPa. The load and the unload processes were done manually and very slowly using the confining pressure pump. This was used to allow for a data-rich stress-strain curve as well.

Applying a non-deviatoric stress to a rock produces a volume decrease and eventually changes the rock fabric permanently, as pores are collapsed. This compression cannot produce a peak load response; the rock can always accept an added increment of load, for as high a pressure as one can generate. In the pressure-volumetric strain space the curve of hydrostatic compression shows four distinct regions (Figure 12). In the first, preexisting fissures are closed and the minerals are slightly compressed. After most of the fissures have closed, further compression produces bulk rock compression, consisting of pore deformation and grain compression at an approximately linear rate. The slope of the curve in this second defined stage is called the bulk modulus, K. In porous rocks, the following stage includes

pore collapse due to stress concentrations around them. Finally, when all the pores have been closed, the only compressible elements remaining are the grains themselves and the bulk modulus becomes progressively higher (Goodman, 1989).

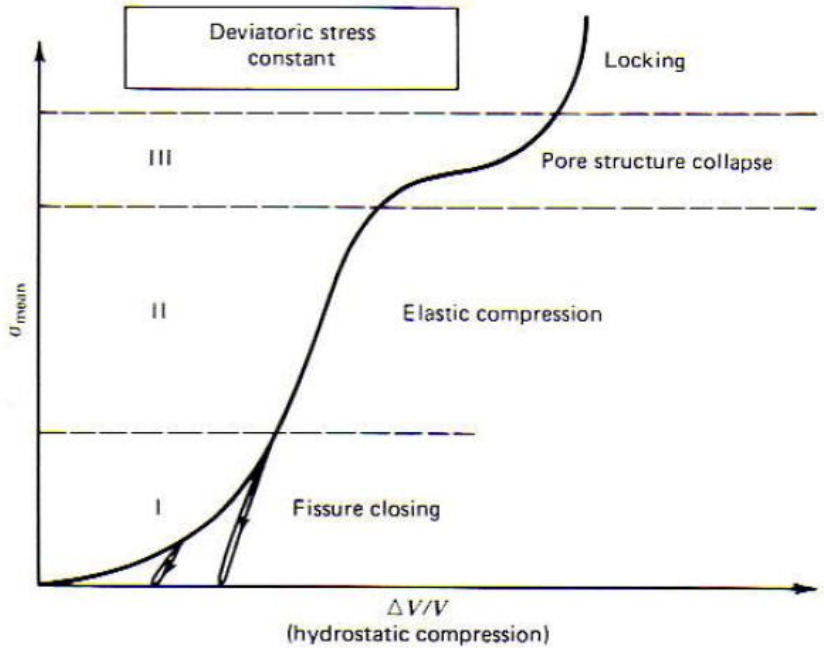

Figure 12: Volumetric compression under increasing mean stress, with constant deviatoric stress (Goodman, 1989).

Using stress-strain curves from the compression tests listed above the following mechanical parameters were determined:

- Uniaxial compressive strength was defined as the peak stress (σ_c) from the uniaxial compression tests.
- The peak "stress difference" (σ_d) as the peak stress difference between the total axial stress applied (σ_1) and the confining pressure at the peak (σ_3) from the triaxial tests.
- The Elastic modulus (E) and Poisson's ratio (ν) were calculated using linear regressions along the linear segment of the axial stress-strain curve from the uniaxial and triaxial tests.
- The crack damage stress (σ_{cd}) was determined from the volumetric stress-strain curve, as the stress where the volumetric strain reached its maximum value from the uniaxial and triaxial tests.

- The bulk modulus (K) was calculated using linear regression along the linear segment of the confining stress-volumetric strain curve from the hydrostatic tests.

3.3 The Brazilian test

A total of 128 indirect tensile (Brazilian) strength tests were performed: 105 samples were tested parallel to bedding direction and 23 samples were tested perpendicular to bedding. The measurements were performed using a manual, hydraulic, mini-load frame manufactured by ELE systems Inc. (SBEL model PLT-75) (Figure 13). Loading was applied by two diametrically opposed concave loading jaws until failure of the sample was achieved.

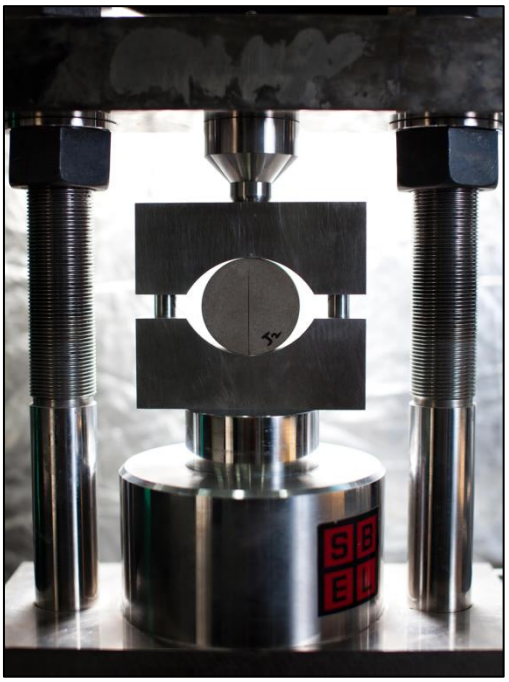

Figure 13: The manual mini–load frame for Brazilian tests- SBEL model PLT-75, with oil shale sample after testing- a typical vertical fracture can be noticed (photo by Yorai Liberman).

This method does not involve the creation of homogeneous state of tensile stress in rock, but rather it involves experimental configuration that leads to inhomogeneous stresses that are tensile in some regions of the specimen (Jaeger et al., 2007).

Fairhurst showed (Fairhurst, 1964) that in a vertically loaded round disk, the horizontal stress is homogenous and tensile while the vertical is heterogeneous and compressive (Figure 14).

The magnitude of the horizontal uniform tensile stresses perpendicular to the loaded diameter is given by:

$$\sigma_{t,B} = \frac{2P}{\pi dt} \tag{8}$$

Where P is the compression load, d is the sample diameter and t is the length of the sample. When the load P reaches its maximum value, $\sigma_{t,B}$ is the Brazilian tensile strength.

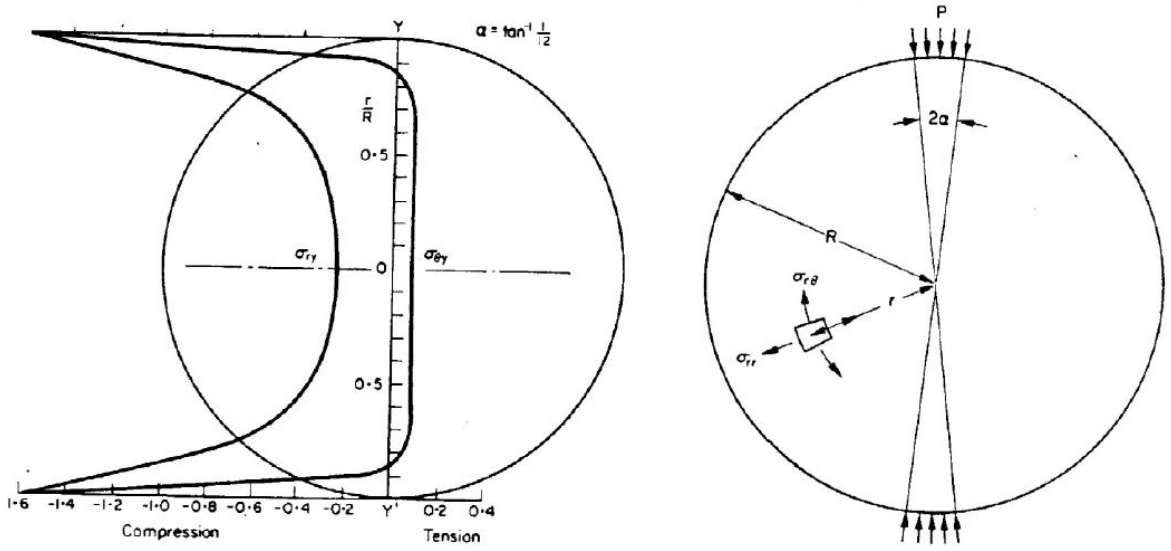

Figure 14: To the left- the disk model in Fairhurst's solution for the Brazilian test; to the right- distribution of tensile and compressive stresses in the disk (Fairhurst, 1964).

The influence of water content on the tensile strength was examined by testing samples at various water content conditions. Water content for each sample was determined by weighing it immediately after the test, drying at 110 °C in the oven for 24 hours and then weighing it again. The water content (ω) was calculated using expression (1). Mechanical anisotropy was tested by measuring the tensile strength parallel and perpendicular to the bedding direction (Figure 15).

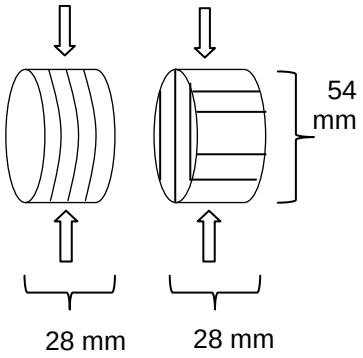

Figure 15: The relationship between loading direction and bedding direction in the indirect tension tests.

3.4 Petrophysical experiments

Porosity (ϕ), Klinkenberg-corrected gas permeability (k_∞), and Klinkenberg slip factor (b) were determined on 236 samples with an unsteady state gas permeameter & porosimeter Coreval 30 device manufactured by Vinci Technologies (Figure 16). Porosity and permeability tests were run in sequence with a single loading of the sample. Anisotropy was examined by measuring the permeability parallel and perpendicular to the bedding direction (Figure 17). The theory and procedures listed below follow mostly the API recommended practice 40 (American Petroleum Institute, 1998).

Figure 16: The Coreval 30 permeameter and porosity meter manufactured by Vinci technologies (photo from www.vinci-technologies.com).

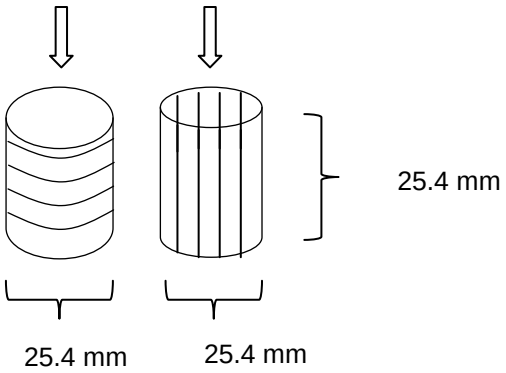

Figure 17: The relationship between flow direction and bedding direction in permeability tests.

3.4.1 Porosity measurement

Porosity is defined as a ratio of the void or pore space volume to the bulk volume of the material. Few definitions must be made: The bulk volume (BV or V_b) is the apparent volume of the measured sample, the grain volume (GV or V_g) is the volume of the grains that compose the sample, the total pore volume (PV or V_p) is the total volume of the voids (linked and unlinked) in the sample and the effective pore volume (PVe) is the volume of only the linked voids in the sample. The definitions are illustrated in Figure 18. Using these definitions of volumes, two types of porosity can be determined: the "total porosity" which is the ratio between the total pore volume and the bulk volume and the "effective porosity" which is the ratio between the effective pore volume and the bulk volume. In this research the effective pore volume is measured directly so that effective porosity is determined, however the term used is just "porosity" (ϕ).

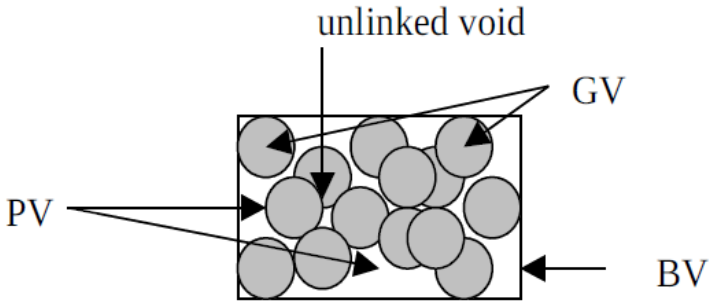

Figure 18: Different volumes of porous material (Coreval30 manual).

The method used in this research for determining the porosity of the Shefela oil shale is called "Boyle's law single cell method for direct void volume". The test procedure begins with the calibration of the porosimeter yielding the reference chamber volume (V_t) and system dead volume (V_d). A dry core sample is then inserted into an elastomer sleeve. An end stem with diameter equal to that of the sample is placed in contact with each end of the sample and confining stress of c.a 400 psi is applied to the external surface of the elastomer.

Nitrogen gas is then admitted into the sample pore volume and equilibrium pressure (P_1) is recorded after stability is reached. The sample pores gas is then vented into a reference cell of known volume (V_t), this results in a lower equilibrium pressure (P_2). The experiment is isothermal and the pore volume of the sample (V_p) can be calculated using the following equations:

Starting with the real gas law,

$$PV = nZRT \tag{9}$$

where P is the pressure of the gas, V is the volume of the gas, n is the number of moles of the gas, Z is the gas deviation factor (which is a function of pressure and temperature of a gas), R is the universal gas constant equals to 8.314 $J \cdot K^{-1} \cdot mol^{-1}$ and T is the temperature of the gas.

In the initial conditions, illustrated in Figure 19, while the nitrogen is filling the pores of the sample, the total number of gaseous moles in the system is the sum of the number of air moles (n_{air}) and the number of nitrogen moles (n_{gas}):

$$n_{total} = \frac{P_a(V_t + V_v)}{Z_a RT} + \frac{P_1\left(V_d + V_p\right)}{Z_{gas1} RT} \tag{10}$$

Where P_a is the absolute atmospheric pressure initially in the refernce reservoir cell of volume V_t, V_v is the volume of the valve, Z_a is the air deviation factor at P_a and T, P_1 is the absolute atmospheric pressure initially in the sample of volume V_p, V_d is the system dead volume and Z_{gas1} is the gas deviation factor at P_1 and T.

In the final conditions, after the nitrogen expanded from the sample pores to the reference cell, the total number of gaseous moles is the number of the mixed gas and air moles:

$$n_{total} = \frac{n_{gas}}{n_{total}} \cdot \frac{P_2\left(V_t + V_v + V_d + V_p\right)}{Z_{gas2} RT} + \frac{n_{air}}{n_{total}} \cdot \frac{P_2\left(V_t + V_v + V_d + V_p\right)}{Z_{air2} RT} \tag{11}$$

Where P_2 is the absolute expanded pressure, Z_{gas2} is the gas deviation factor at P_2 and T and Z_{air2} is the air deviation factor at P_2 and T.

The following simplification can be made:

$$P_1 \gg P_a \quad and \quad n_{gas} \gg n_{air} \tag{12}$$

Thus it follows that:

$$\frac{n_{gas}}{n_{total}} \cong 1 \quad and \quad \frac{n_{air}}{n_{total}} \cong 0 \tag{13}$$

Hence, the final materials balance is:

$$n_{total} = \frac{P_2\left(V_t + V_v + V_d + V_p\right)}{Z_{gas2}RT} \tag{14}$$

Finally, with the combination of expressions (10) and (14) the pore volume (V_p) is calculated. The bulk volume is measured using a caliper with precision of 0.01 mm and the porosity is then found by dividing the pore volume by the bulk volume.

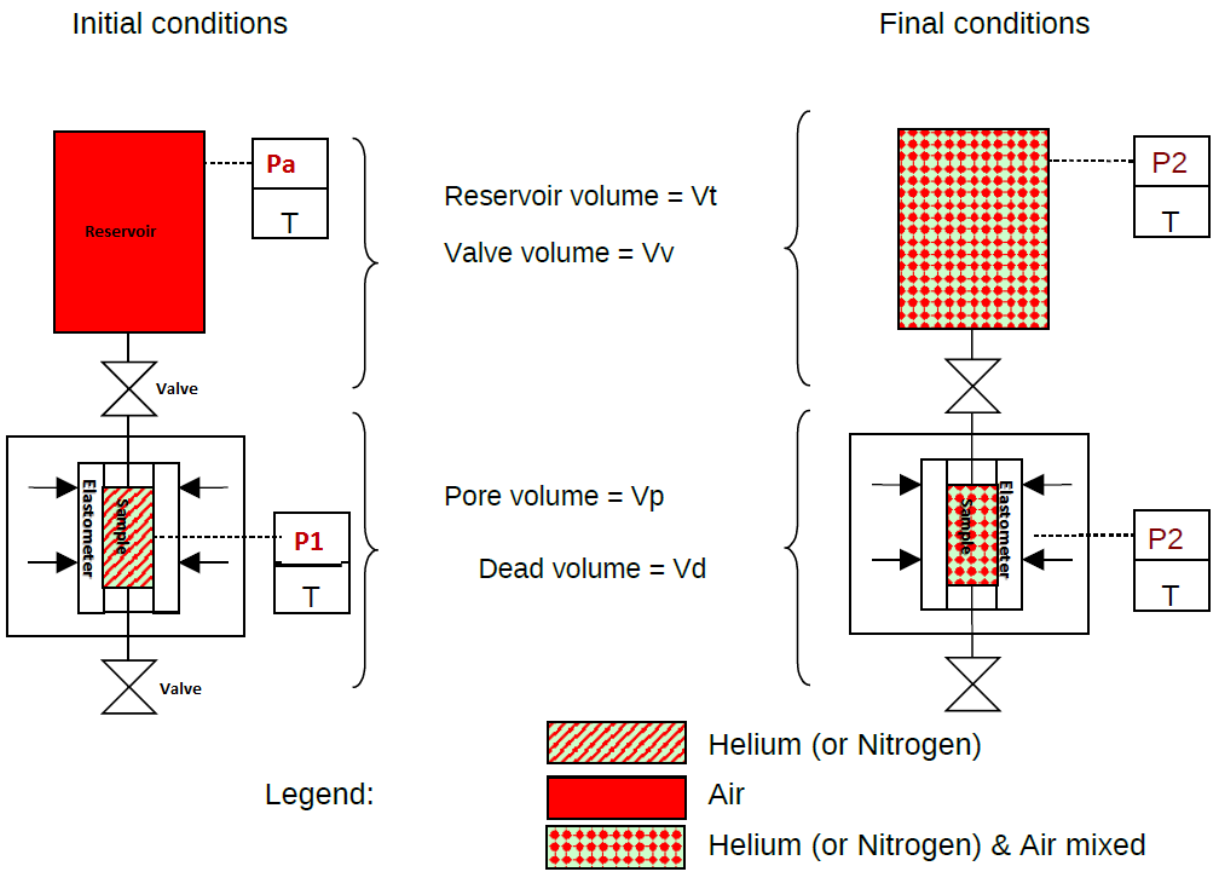

Figure 19: Schematic of isostatic load cell for direct pore volume determination; to the left, the initial conditions of the pore volume measurement and to the right, the final conditions (modified from the Coreval30 manual).

Advantages of this method include:

The operation is quick and simple; harmful reactions between the rock and saturating fluid are eliminated by use of non-reactive gas; direct measurement of the pore volume eliminates

the sensitivity of the pore volume to errors in the measurement of either BV or GV, where both BV and GV are large numbers relative to the pore volume, and PV = BV – GV.

Limitations of this method include:

The system must be carefully calibrated for dead volume; the sample must be a good quality right cylinder with no surface vugs or chipped corners (vugs will yield erroneously low pore volume and non-parallel ends will yield high pore volume); the sample must be clean of hydrocarbons and dry, otherwise erroneously low pore volume will be determined; porosity is determined at low confining stress, which results in a porosity higher than present in the reservoir.

3.4.2 Permeability measurement

Permeability is a property of a porous medium and is a measure of its ability to transmit fluids. The measurement of permeability of a porous rock, or stratum, is a measurement of the fluid conductivity of the particular material. Measurement of the flow of fluid through a sample in a particular direction yields permeability of the sample in that direction. The effective permeability of a porous media is defined as a measure of its fluid conductivity to a particular phase of a multi-phase fluid system residing within the medium, where the saturation of each phase is specified. The relative permeability is the ratio between the effective permeability to some arbitrary reference permeability. The fundamental SI unit of permeability is m^2, and it is defined as follows: a permeability of one meter squared will permit a flow of 1 m^3/s of fluid of 1 Pa·s viscosity through an area of 1 m^2 under a pressure gradient of 1 Pa/m. The common unit used is Darcy, where 1 Darcy equals 0.986823 x 10^{-12} m^2.

In the mid-nineteenth century, Darcy established (Darcy, 1856) the relationship between the permeability of a porous media and the potential gradient observed during the flow of a fluid through it known now as Darcy's Law. It states that the volumetric rate of flow per unit cross-sectional area of permeable medium (the volumetric flux) is directly proportional to the potential gradient, and inversely proportional to the viscosity of the fluid; the coefficient of proportionality is permeability:

$$-\frac{dP}{dx} = \mu \frac{V}{k} \tag{15}$$

Where μ is the dynamic viscosity of the fluid, V is the volumetric flux of the fluid per unit area A, k is the permeability and dP/dx is the potential gradient.

The work of Forchheimer (Forchheimer, 1901) showed that Darcy's law is restricted to the case of low volumetric fluxes. At higher fluxes, Forchheimer observed that the potential gradient required for a given volumetric flux is greater than that predicted by Darcy's law by an amount proportional to the product of the fluid's density, ρ, and the square of its volumetric flux, V. The coefficient of proportionality is the inertial resistivity of the porous medium, β (ft^{-1}). This additional form of Darcy's law is known as the Forchheimer equation:

$$-\frac{dP}{dx} = \mu \frac{V}{k} + \beta \rho V^2 \tag{16}$$

Inertial energy dissipation is due to accelerations that a fluid undergoes as it travels tortuous paths through a porous medium. These accelerations cause secondary flow patterns, in which, part of the flow energy is converted to heat through viscous shear. The flow energy provided by the pressure differential is, in this case, not only used for the movement of the fluid as a whole but also spent on internal movements. These internal movements can be characterized by the kinetic energy of the fluid (ρV^2).

Even when inertial effects are properly accounted for, the permeability of a porous medium to gas is dependent upon the mean free path of the flowing gas, hence among other things, upon its absolute pressure. When a gas is flowing along a solid wall, the layer of gas next to the surface is in motion with respect to the wall. As a consequence the quantity of gas flowing through a capillary is larger than would be expected for a liquid in which molecular velocities are assumed to be zero along the pore walls. This effect is called 'slip' and was applied to the flow of gas through a capillary whose radius is large compared with the mean free path of the gas molecules (Kundt and Warburg, 1875; Warburg, 1876). Klinkenberg applied the theory to a model of flow of gas through an idealized porous medium in which all capillaries are of the same diameter and are oriented randomly (Klinkenberg, 1941). He came into a relation between the apparent permeability k_g (pressure dependent) and true permeability k_∞ of an idealized porous system.

$$k_g = k_\infty \left(1 + \frac{4c\bar{\lambda}}{r}\right) \tag{17}$$

Where *c* is a proportionality factor (slightly less than 1), λ is mean free path of the gas molecules and *r* is the radius of capillary. As the mean free path is inversely proportional to the pressure, the relation can be written as:

$$k_g = k_\infty \left(1 + \frac{b}{\bar{p}}\right) \tag{18}$$

Where *p* is the mean gas pressure and *b* is the slip factor constant that is inversely proportional to the radius of capillary (pore throat radius).

When gas slip is ignored, permeability calculated from the Forchheimer equation, or from Darcy's Law (provided that inertial resistance is negligible), is higher than that obtained using a non-reactive liquid. This difference is small for high permeability samples, but becomes progressively larger with decreasing permeability. It is minimized by using high mean pore pressures in gas permeability measurements. To avoid the problem of obtaining pore-pressure-dependent gas permeabilities, Klinkenberg presented a method in which gas permeability measurements made at several different mean pore pressures can be extrapolated to infinite pore pressure. He showed that this extrapolated gas permeability (now called "Klinkenberg-corrected gas permeability", k_∞) is equal to the permeability obtained using a non-reactive liquid, such as a clean, refined hydrocarbon.

Single-phase permeability measurements can be separated into four major categories: those utilizing flowing gas or liquid under steady-state or unsteady-state (transient) conditions. In this research Klinkenberg-corrected gas permeabilities were determined using the pressure-falloff, axial gas flow technique (under unsteady-state conditions). The permeability measurement was taken automatically in a sequence after the porosity measurement as explained next.

Unsteady-State Gas Permeability Determination technique

The advent of high speed data-acquisition systems, accurate pressure transducers, and digital computers has made it convenient to measure permeability under transient or unsteady-state flow conditions. Transient measurements employ fixed-volume reservoirs for gas or liquid. Using gas is preferable because it has low heat capacity and work-related temperature changes can be virtually eliminated by fabricating reservoirs from material of high thermal

conductivity and packing them with copper tubes parallel to the flow axis. This technique has a useful permeability range of 0.001 to 30,000 millidarcys (through the use of multiple upstream gas reservoirs and pressure transducers).

The Coreval30 system used in this research is characterized by upstream reservoir from which the gas (nitrogen) flows into the core sample. The downstream end of the sample is vented to atmospheric pressure (Figure 20). The maximum upstream pressure used is fairly low, 10 to 250 psig (pressure relative to atmospheric pressure), varying inversely with the permeability to be measured.

An accurate pressure transducer that measures gauge pressure is connected to the manifold at the upstream of the sample holder (P1 at Figure 20). As the measurement begins, the reservoir, manifold, and the whole sample (to the outlet valve) are filled with gas. The outlet valve is then opened to initiate the pressure transient. When the upstream pressure has decayed to about 85 percent of the fill pressure, during which time a smooth pressure profile is established throughout the length of the sample, data collection begins. Pressures at selected intervals and corresponding elapsed times are read and recorded. A single transient pressure falloff produces data for 6 to 30 separate permeability calculations, each at a different flow velocity and mean pore pressure. Adequate variation of flow conditions during a single transient test makes possible the calculation of slip-corrected (Klinkenberg) permeability (k_∞), Klinkenberg slip factor (b), and inertial resistivity (β) of the porous medium.

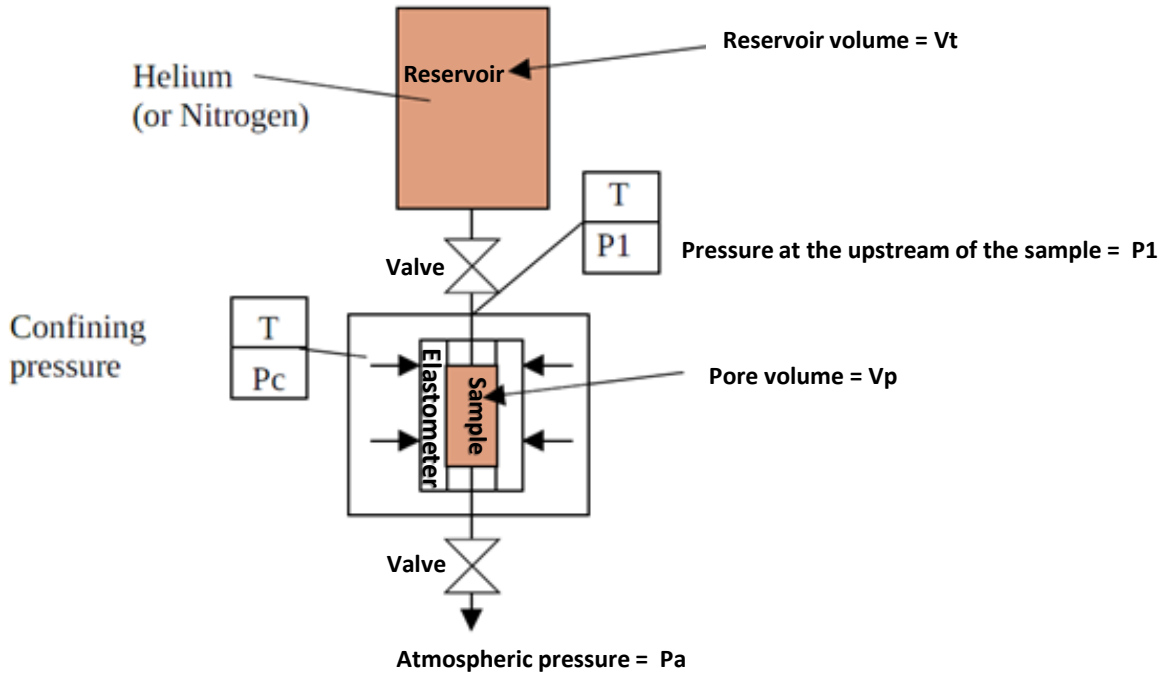

Figure 20: Schematic of pressure falloff gas permeameter (modified from the Coreval30 manual)

Procedures for calculating the k∞, b and β

S.C. Jones proposed in 1972 the equation for axial flow used with the pressure falloff method and established the Pressure-Falloff, Axial Gas Flow Measurements (Jones, 1972). He started from the expression of the axial volumetric flow rate *V [s,t]* of a perfect gas coming from a reservoir of volume V_t through a core sample. The following equation gives the volumetric flow rate of the gas at any position into the core sample and at any time:

$$V[x,t] = \frac{-V_t(1+\delta f[c,g])}{(P[x,t]+P_a)} \cdot \frac{\partial P_0(t)}{\partial t} \qquad (19)$$

where δ and *f[c,g]* are correction factors accounting for the variation of the mass flow with the position into the core sample, *P(x,t)* is the pressure at any time and any location in the sample, *Pa* is the atmospheric pressure.

The factor δ takes into account the difference of volume between the reservoir and the pore volume of the core sample. When working with smaller reservoir, this correction will be greater. It is given by:

$$\delta = \frac{2}{3}\frac{V_p}{V_t} \tag{20}$$

Where *Vp* is the pore volume of the sample and *Vt* is the volume of the reservoir.
The *f[c,g]* factor is a function of the pressure and the position in the core sample, it is given by:

$$f[c,g] = (c+1)(1-2c) + (2c-g)\sqrt{(c+1)(c+g)} \tag{21}$$

At first Jones substituted (18) and (19) into Darcy's law (15) and after integration on length *L* he obtained:

$$\frac{-V_t(1+\delta G[c])}{P_0(t)}\left(\frac{\partial P_0(t)}{\partial t}\right) = \frac{k_\infty A}{29.39\mu L}(P_0(t) + 2(P_a + b)) \tag{22}$$

Where *G[c]* is the integrated form of *f[c,g]* and is within:

$$0.5 < G[c] < 0.6 \tag{23}$$

The right-hand term of equation (22) forms a straight line when expressed as a function of the pressure at *t*, P_0(t). The slope *m* and the intercept *i* of this line are:

$$m = \frac{k_\infty A}{29.39\mu L} \tag{24}$$

$$i = 2(P_a + b)m \tag{25}$$

The left-hand term of the equation (22) is termed the "corrected instantaneous flow rate function", $y_c(P_{gn})$. The solution of which requires the calculation of the pressure-time derivatives. This is calculated using the pressure falloff curve obtained from a single measurement:

Let P_{gn} be the geometrical mean of two pressures P_{n-1} and P_n on the pressure falloff curve:

$$P_{g_n} = \sqrt{P_{n-1}P_n} \tag{26}$$

Then,

$$y(p_{g_n}) = \frac{V_t ln\left[\frac{P_{n-1}}{P_n}\right]}{t_n - t_{n-1}} \tag{27}$$

Where t_n and t_{n-1} are the time points on the pressure falloff curve corresponding to P_n and P_{n-1} (Figure 21).

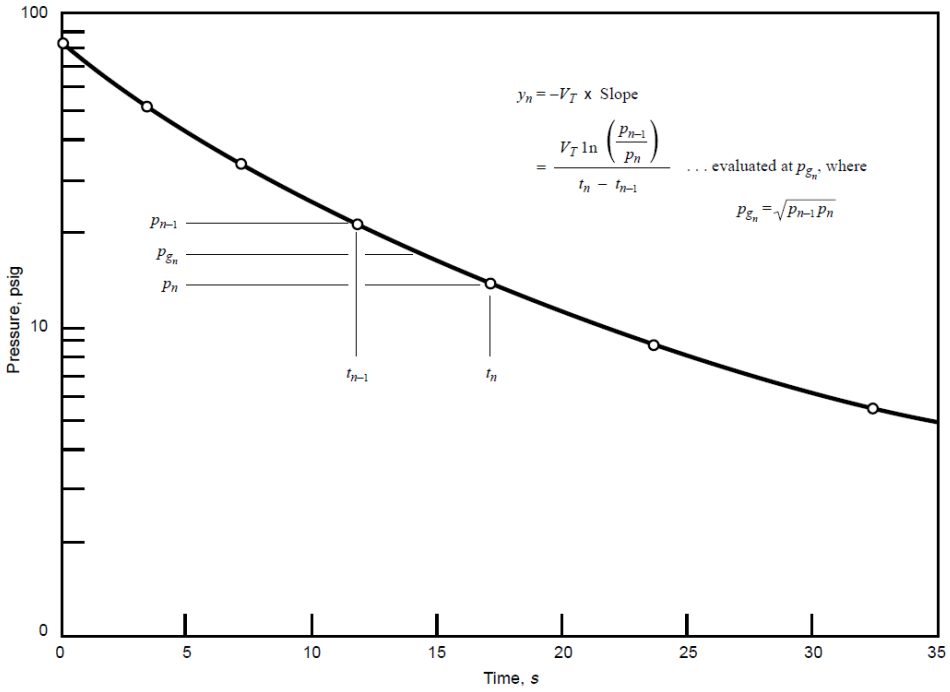

Figure 21: Construction of flow variables $y(P_{gn})$ and P_{gn} from the pressure falloff curve (American Petroleum Institute, 1998)

And the corrected instantaneous flow rate function $y_c(P_g)$ is now:

$$y_c(P_{g_n}) = y(P_{g_n})(1 + \delta G[c]) \tag{28}$$

Hence, equation (22) can be written as followed:

$$y_c(P_{g_n}) = i + mP_{g_n} \tag{29}$$

The linearity of the representation of y_c versus P_{gn} indicates that the gas flows into the core sample by following Darcy's law. Deviations from linearity where observed for higher flow

rate of the gas because of inertial thermal effects. Jones proposed (Jones, 1972) to use the Forchheimer equation (16) to account for these second order effects. By an equivalent development he obtained the following simplified equation:

$$z = \frac{1000}{k_\infty} + \frac{\alpha}{k_\infty} x \tag{30}$$

z and *x* are functions that are strongly dependent on the slip factor *b*. When looking at the graphical representation of z = f(x) (Figure 22) it is evident that linearity is only obtained for a unique value of *b*. This optimal value of *b* is necessary to assume the linearity of the correlation. To get this value, the API recommended practice 40 (American Petroleum Institute, 1998) proposes an iterative program based on 12 steps. While following these steps, one is trying several values of *b* by increment or decrement of 10%, calculating the slope and the intercept of the main equation by linear regression and the standard error of linear regression. The program converges quickly to the optimal *b* value, where the standard error is minimal. Once the optimal *b* value is reached, the permeability k_∞ and the inertial resistivity factor β are deduced from the equation of a straight line (Equation 30).

The whole calculation process is programmed in the Coreval30 device.

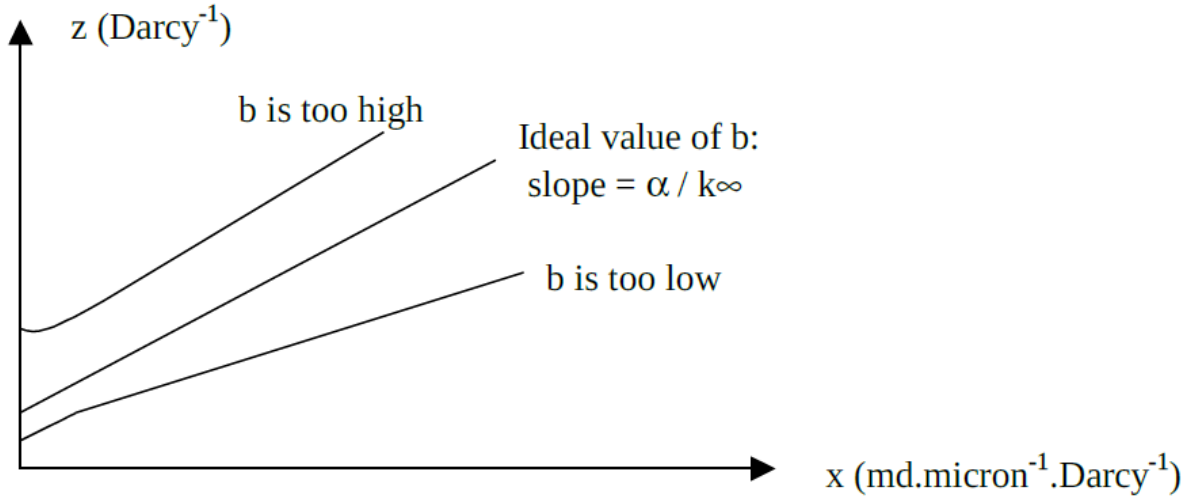

Figure 22: Graphical schematic representation of z=f(x), equation 30 (Coreval30 manual).

Advantages of the technique include:

Non-slip-corrected permeability, k_g, can be calculated from these results for any desired gas at any mean pore pressure for purposes of comparison with conventional measurements; no flow meters are required for the method, flow rates are calculated from pressure-time measurements.

Limitations of this method include:

The technique requires high quality pressure transducers, fast data acquisition equipment, and a high computational demand; low permeability samples require a leak-tight system (for this or any other technique), and no bypass in the sample holder (past the rubber sleeve).

Chapter 4- Results

4.1 Mechanical tests results

This section presents the mechanical test results including all compression and Brazilian tests. All the compression tests were performed at a constant strain rate of 5 x 10^{-5} s^{-1}.

4.1.1 Unconfined (Uniaxial) compression tests

Uniaxial compression tests were performed on 8 samples from selected depth intervals of the Aderet borehole. The obtained stress-strain curves for the samples are shown in Figure 23 (a)-(h). The Elastic modulus (E) and Poisson's ratio (ν) were calculated using linear regressions along the linear segment of the axial stress-strain curve which is shown in each diagram. The static Elastic modulus, the Poisson's ratio and the obtained uniaxial strength are summarized in Table 2.

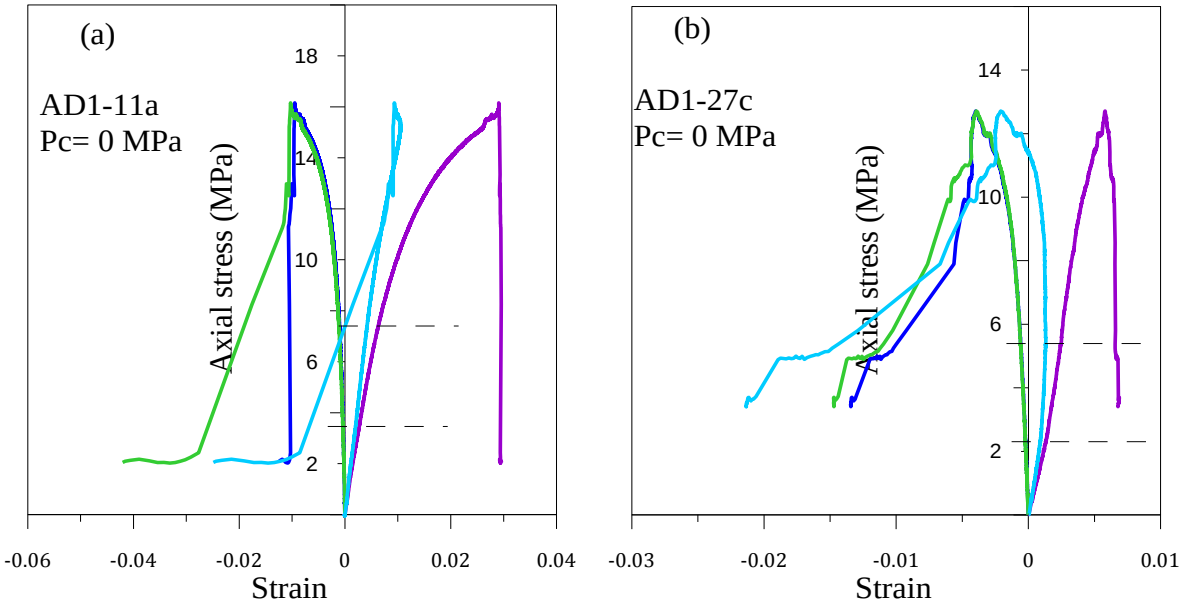

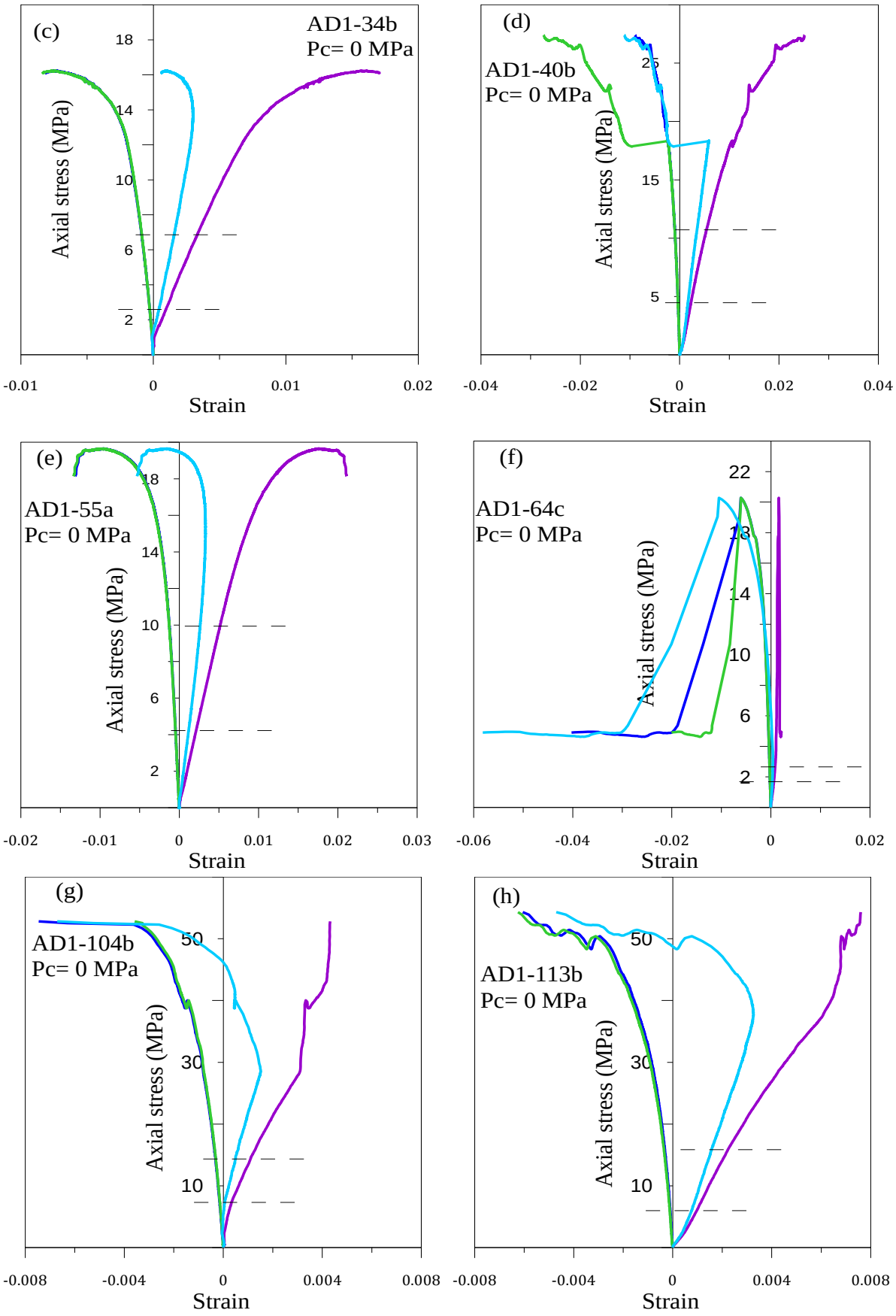

Figure 23: Stress strain curves for uniaxial compression tests of samples AD1-11b, 27c, 34b, 40b, 55a, 64c, 104b and 113b, (a)-(h) respectively. Legend: -- axial strain, -- radial strain1, -- radial strain2, -- volumetric strain, the dashed line in each graph represents the linear segment.

Table 2: Concentrated results for Uniaxial compression tests

Sample	Depth, m	σ_c, MPa	E, GPa	ν	ω, %	ρ_t, gr/cm^3	TOC, %
AD1-11a	291.4-292.95	16.15	1.11	0.20	5.41	1.44	12.54
AD1-27c	338.7-341.75	12.71	2.75	0.32	23.93	1.80	7.62
AD1-34b	356.9-359.95	16.24	1.76	0.27	13.92	1.60	10.37
AD1-40b	375-378.3	27.47	1.98	0.21	1.65	1.34	16.78
AD1-55a	420-423	19.65	1.90	0.26	25.49	1.67	17.14
AD1-64c	447-450	20.78	2.82	0.26	23.00	1.74	12.35
AD1-104b	570.65-573.7	52.83	9.18	0.21	0.64	1.87	3.30
AD1-113b	598.1-601.15	54.68	8.05	0.18	1.15	2.02	1.94

Legend: σ_c is Uniaxial compressive strength, E and ν are Young's modulus and Poisson's ratio, ω is water content at which the test was performed, ρ_t is bulk density and TOC is total organic carbon in wt%.

4.1.2 Confined (Triaxial) compression tests

Triaxial compression tests were performed on 7 samples from 335-346 m depth. Each test was performed under different initial confining pressure value: 1 MPa, 2 MPa, 3 MPa, 4 MPa, 5 MPa and 10 MPa. Stress-strain curves obtained from the triaxial tests are shown in Figure 24 (a)-(f) where "stress difference" stands for the difference between the total axial stress applied (σ_1) and the confining pressure (σ_3). In the last two measurements, Figure 24(f) and Figure 24(g), a problem in the test setup was detected (the samples reached the maximum stress difference almost immediately and no linear behavior was observed). The static Elastic modulus, the Poisson's ratio and the obtained stress difference at peak ($\Delta\sigma_c$) are summarized in Table 3.

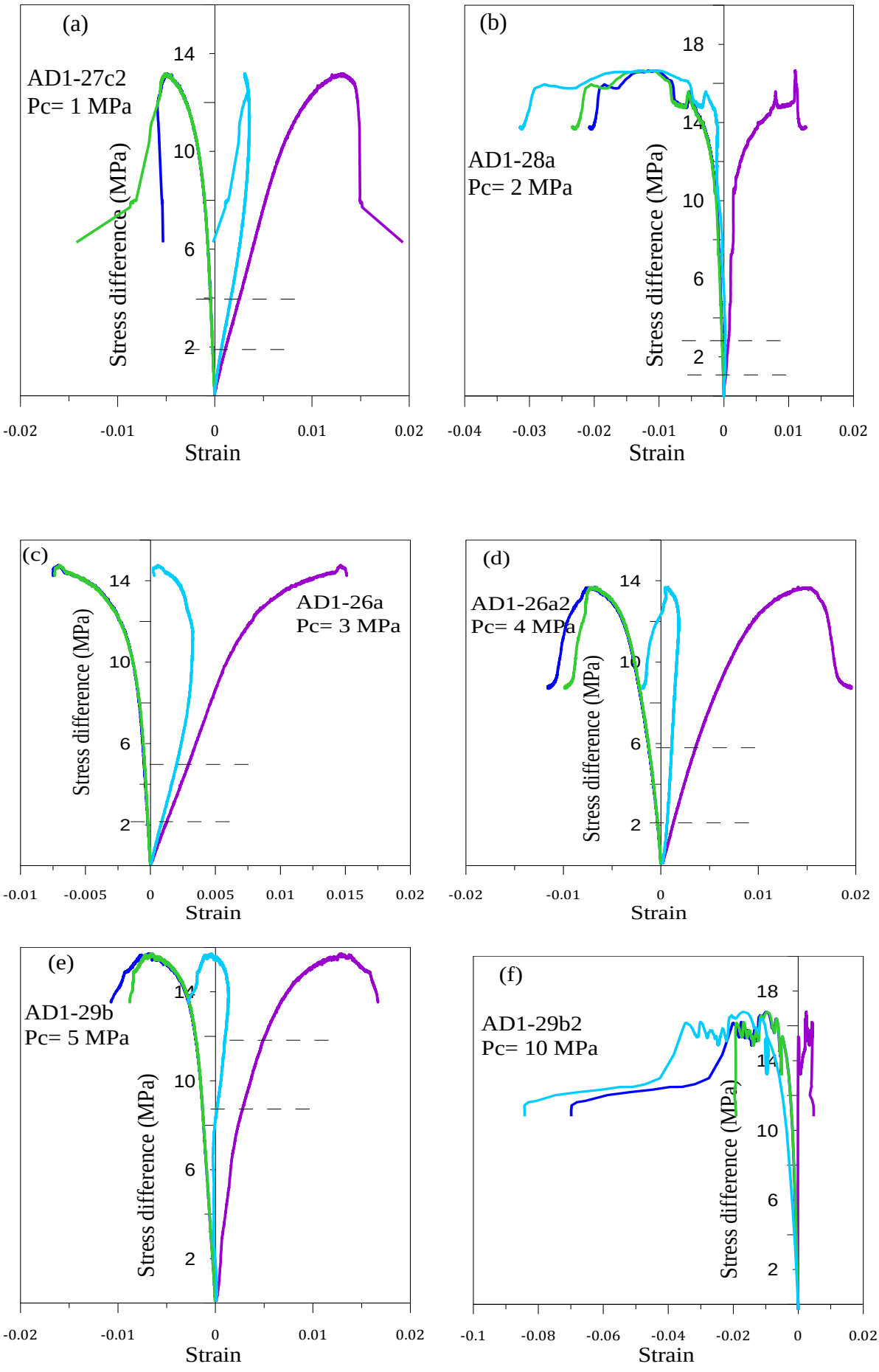
(a)
AD1-27c2
Pc= 1 MPa
Stress difference (MPa)
Strain
(b)
AD1-28a
Pc= 2 MPa
Stress difference (MPa)
Strain
(c)
AD1-26a
Pc= 3 MPa
Stress difference (MPa)
Strain
(d)
AD1-26a2
Pc= 4 MPa
Stress difference (MPa)
Strain
(e)
AD1-29b
Pc= 5 MPa
Stress difference (MPa)
Strain
(f)
AD1-29b2
Pc= 10 MPa
Stress difference (MPa)
Strain

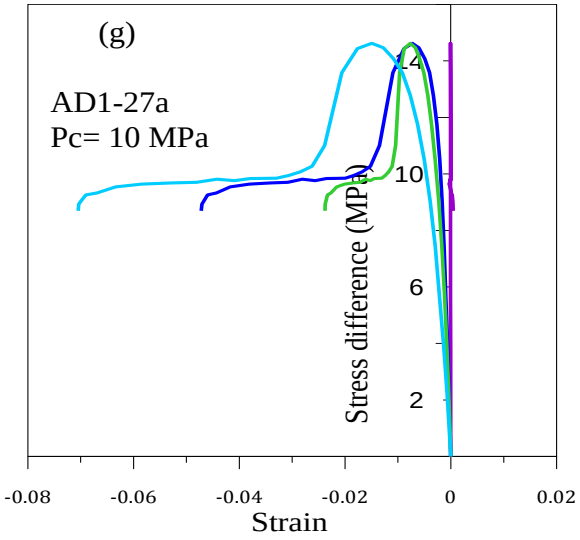

Figure 24: Stress strain curves for triaxial compression tests of samples AD1-27c2, 28a, 26a, 26a2, 29b, 29b2, and 27a, (a)-(g) respectively. Legend: -- axial strain, -- radial strain1, -- radial strain2, -- volumetric strain, the dashed line in each graph represents the linear segment. In figure 23 (e) the 0-8 MPa segment is a test artifact.

Table 3: Results for Triaxial compression tests

Sample	Depth, m	P_c i, MPa	$\Delta\sigma_c$, MPa	E, GPa	ν	ω, %	ρ_t, gr/cm^3	TOC, %
AD1-27c2	338.7-341.75	1	13.20	1.44	0.16	26.45	1.81	9.90
AD1-28a	341.75-344.8	2	16.65	4.11	0.40	21.40	1.71	9.10
AD1-26a	335.65-338.7	3	14.77	1.69	0.16	24.32	1.88	9.11
AD1-26a2	335.65-338.7	4	13.70	1.63	0.40	24.13	1.85	8.50
AD1-29b	344.8 - 347.85	5	15.69	1.49	0.29	26.17	1.79	10.93
AD1-29b2	344.8 - 347.85	10	16.22	NA	NA	24.74	1.83	9.53
AD1-27a	338.7-341.75	10	14.60	NA	NA	25.86	1.81	9.90

Legend: $\Delta\sigma_c$ is the peak stress difference, P_c i is the confining pressure at starting point of the test, E and ν are Young's modulus and Poisson's ratio, ω is water content at which the test was performed, ρ_t is bulk density and TOC is total organic carbon in wt%; NA stands for - not determined Elastic static constants.

4.1.3 Hydrostatic compression tests

Sample AD1-4c and sample AD1-27b were subjected to hydrostatic compression to a maximum confining pressure values of Pc=10 MPa and 30 MPa respectively. The static bulk modulus (*K*) is obtained by linear regression along the linear segment of the hydrostatic pressure vs. total volumetric strain response curve. For sample AD1-4c one linear segment is detected, while sample AD1-27b that was hydrostatically compressed to 30 MPa shows 3 different linear segments. The slope of each segment is getting progressively higher indicating the increase in bulk modulus (K_1, K_2, K_3) with the increase in hydrostatic pressure. The results are summarized in Table 4 and Table 5.

Table 4: Results for hydrostatic test of sample AD1-4c

Sample	Depth, m	K, MPa	ω, %	TOC, %
AD1-4c	271.6-274.65	1293	2.93	8.66

Table 5: Results for hydrostatic test of sample AD1-27b

Sample	Depth, m	K_1, MPa	K_2, MPa	K_3, MPa	ω, %	TOC, %
AD1-27b	338.7-341.75	1471	3287	4850	24.69	7.28

Legend: K is the static bulk modulus, ω is water content at which the test was performed and TOC is total organic carbon in wt%.

The entire load and unload history is shown in Figure 25 and Figure 26 below.

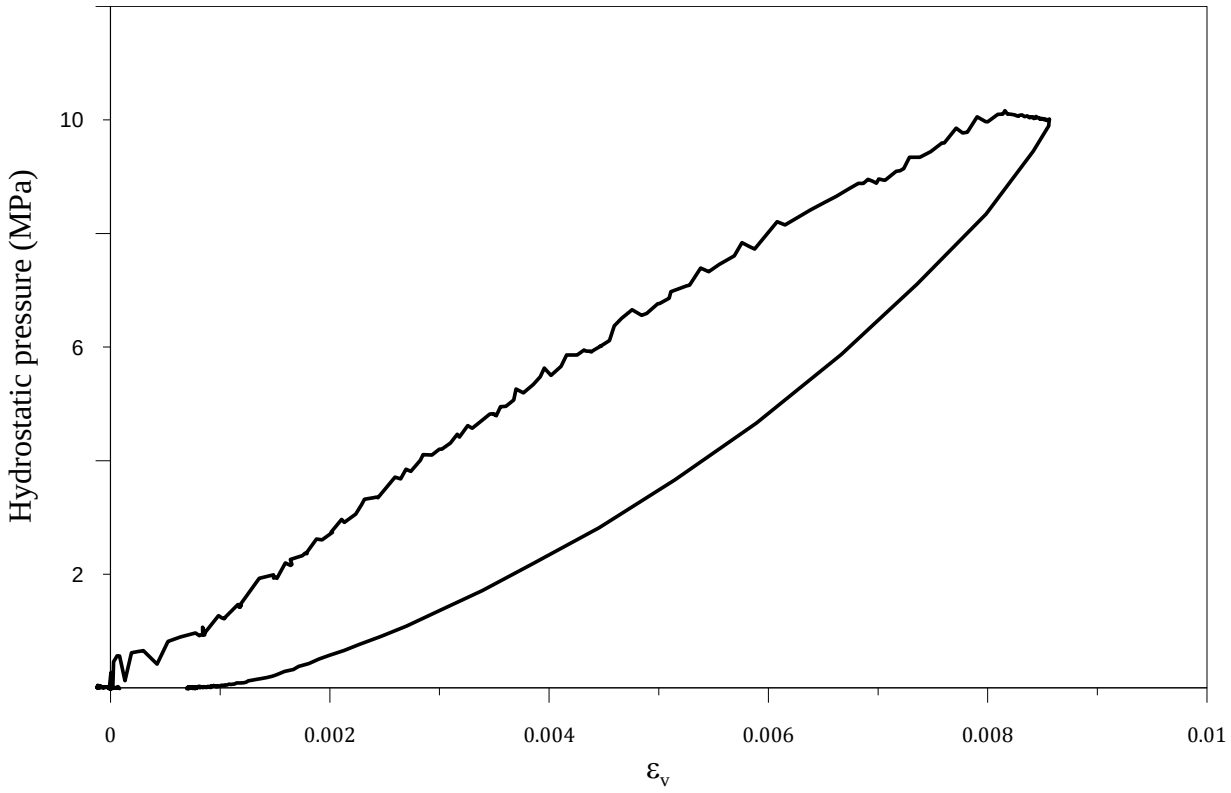

Figure 25: Load and unload for sample AD1-4c.

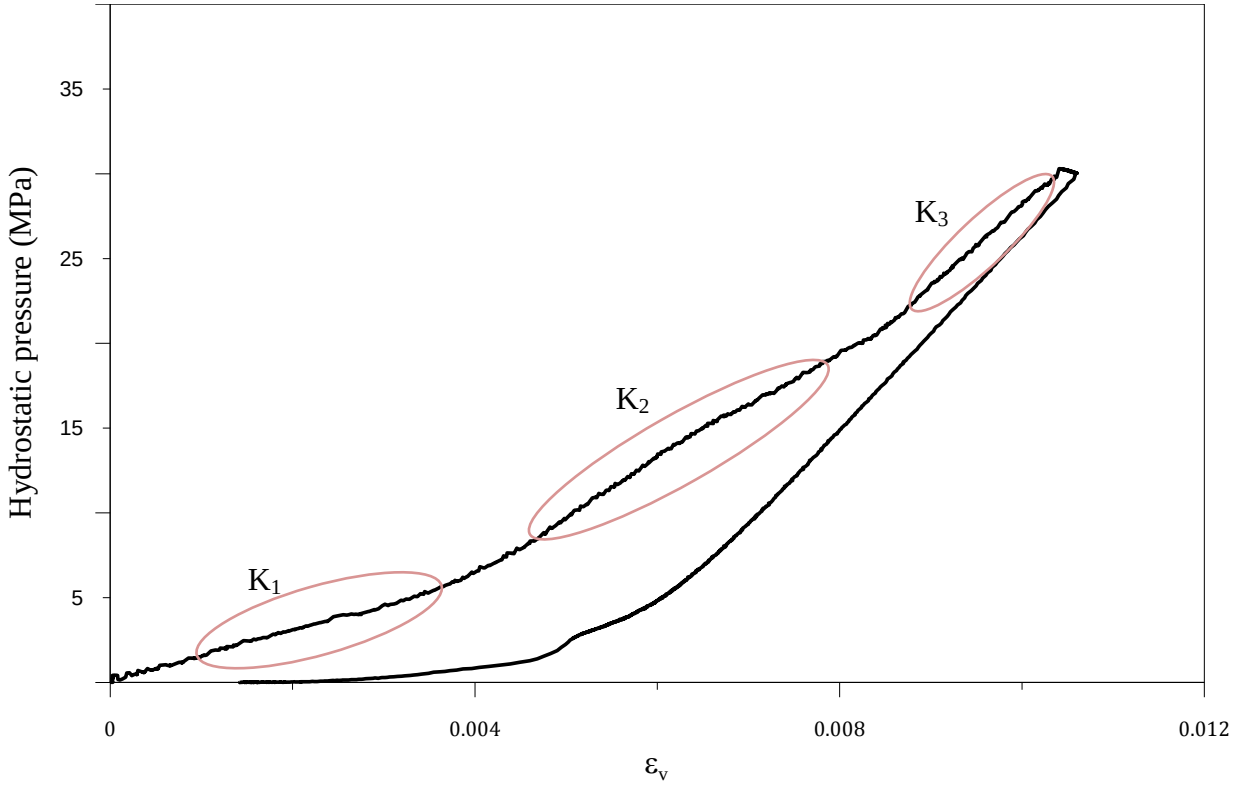

Figure 26: Load and unload for sample AD1-27b.

It can be seen in Figure 26 that the first segment (up to 8 MPa) indicates the closure of micro-cracks, the slope for this segment (K_1) is similar to the bulk modulus of sample AD1-4c. The next segment of a steeper slope (K_2) is obtained between 8 and 20 MPa. It indicates higher density caused by the first compaction phase. Finally, the steepest slope in this measurement is obtained between 20 and 30 MPa (K_3) indicating initiation of irreversible compaction but not yet pore collapse.

4.1.4 Brazilian tensile strength

A total of 128 Brazilian tensile strength tests were performed. The results are summarized in Table 6.

Table 6: Results for Brazilian tests

Sample	Depth, m	σ_t, MPa	ω, %	TOC, %	bedding orientation
AD1-1-a	265.3-266.8	3.36	Dry	NA	II
AD1-1-a	265.3-266.8	4.58	Dry	NA	II
AD1-1-a	265.3-266.8	3.19	Dry	NA	II
AD1-1-a	265.3-266.8	2.42	Dry	NA	II
AD1-4-c	271.6-274.65	1.74	25.77	8.30	II
AD1-4-c	271.6-274.65	1.62	25.96	8.30	II
AD1-4-c	271.6-274.65	2.72	0.82	8.30	II
AD1-4-c	271.6-274.65	3.11	0.89	8.30	II
AD1-11-a	291.4-292.95	2.95	0.86	12.94	II
AD1-11-a	291.4-292.95	2.47	0.88	12.94	II
AD1-24a	329.55-332.6	2.52	19.35	9.69	II
AD1-24a	329.55-332.6	2.58	20.15	9.69	II
AD1-24a	329.55-332.6	1.76	19.21	9.69	+
AD1-26a	335.65-338.7	2.35	16.01	10.60	II
AD1-26a	335.65-338.7	2.16	10.07	10.60	II
AD1-26a	335.65-338.7	1.87	24.78	10.60	+
AD1-27c	338.7-341.75	2.84	7.77	8.61	II
AD1-27c	338.7-341.75	1.93	25.54	8.61	+
AD1-28-a	341.75-344.8	2.42	8.00	11.45	II
AD1-28-a	341.75-344.8	2.32	7.78	11.45	II
AD1-28b	341.75-344.8	1.45	6.33	10.09	+
AD1-29-c	344.8 - 347.85	2.09	6.82	10.00	II
AD1-29-c	344.8 - 347.85	1.93	6.51	10.00	II
AD1-30-a	348.77-350.82	3.99	2.16	3.48	II
AD1-30-a	348.77-350.82	3.97	3.20	3.48	II
AD1-31-a	350.82-352	2.51	6.38	8.96	II
AD1-31-a	350.82-352	2.01	6.76	8.96	II
AD1-32-a	352-353	3.86	2.05	12.53	II
AD1-32-a	352-353	3.93	2.30	12.53	II

AD1-32-a	352-353	3.68	2.33	12.53	II
AD1-32-a	352-353	3.03	8.85	12.53	II
AD1-33-a	353.81-356.4	4.36	4.10	13.18	II
AD1-33-a	353.81-356.4	4.23	4.04	13.18	II
AD1-33-a	353.81-356.4	3.66	3.67	13.18	II
AD1-34-b	356.9-359.95	2.84	10.81	10.50	II
AD1-34-b	356.9-359.95	2.48	9.54	10.50	II
AD1-35-c	359.95-363	3.01	10.42	10.47	II
AD1-35-c	359.95-363	2.70	10.98	10.47	II
AD1-36-a	363-366.05	2.35	9.26	12.70	II
AD1-36-a	363-366.05	1.91	9.64	12.70	II
AD1-38-c	369.3-372.3	2.22	5.40	13.29	II
AD1-38-c	369.3-372.3	2.76	5.04	13.29	II
AD1-39-b	372.3-375.3	4.36	4.54	11.20	II
AD1-39-b	372.3-375.3	3.31	5.18	11.20	II
AD1-40-b	375-378.3	3.56	10.15	15.24	II
AD1-40-b	375-378.3	3.67	9.70	15.24	II
AD1-42-b	381.3-384.3	2.75	7.02	13.92	II
AD1-42-b	381.3-384.3	3.74	7.56	13.92	II
AD1-42-b	381.3-384.3	4.03	7.60	13.92	II
AD1-43-b	384.3-387.1	4.27	7.73	16.30	II
AD1-43-b	384.3-387.1	2.64	8.55	16.30	II
AD1-43-b	384.3-387.1	4.14	9.17	16.30	II
AD1-45-a	390.1-393.1	5.35	8.26	15.20	II
AD1-45-a	390.1-393.1	5.08	8.53	15.20	II
AD1-47a	396.1-399	3.20	24.29	18.03	II
AD1-47a	396.1-399	4.78	12.77	18.03	II
AD1-51a	408-411	3.22	8.19	11.31	+
AD1-52b	411-414	1.76	6.85	16.70	+
AD1-54-c	417-420	3.07	8.64	16.48	II
AD1-54-a	417-420	2.49	3.12	15.17	II
AD1-54-a	417-420	3.84	10.62	15.17	II
AD1-55-a	420-423	3.41	6.23	16.52	II
AD1-57b	426-429	3.98	11.73	15.84	II
AD1-57b	426-429	4.16	7.08	15.84	II
AD1-57b	426-429	2.75	10.24	15.84	+
AD1-58b	429-432	3.33	10.15	14.81	II
AD1-58b	429-432	2.75	5.65	14.81	II
AD1-58b	429-432	1.93	11.43	14.81	+
AD1-61b	438-441	4.20	25.00	18.97	II
AD1-61b	438-441	4.91	8.14	18.97	II
AD1-61b	438-441	3.32	25.43	18.97	+
AD1-62c	441-444	3.57	23.52	13.56	II
AD1-62c	441-444	2.98	15.79	13.56	II
AD1-62c	441-444	2.36	24.96	13.56	+

AD1-65c	450-453	3.38	17.34	6.58	II
AD1-65c	450-453	3.01	10.58	6.58	II
AD1-65c	450-453	3.13	17.08	6.58	+
AD1-67c	456-459	3.03	15.47	4.66	II
AD1-67c	456-459	3.03	10.07	4.66	II
AD1-67c	456-459	0.84	16.99	4.66	+
AD1-71c	468-471	2.74	24.72	10.37	II
AD1-71c	468-471	3.00	20.75	10.37	II
AD1-71c	468-471	1.96	24.41	10.37	+
AD1-72a	471-474	5.19	1.18	11.25	II
AD1-72a	471-474	4.94	1.13	11.25	II
AD1-72a	471-474	1.68	1.20	11.25	+
AD1-73c	474-477	4.41	1.02	7.95	II
AD1-73c	474-477	4.93	1.00	7.95	II
AD1-73c	474-477	2.35	1.05	7.95	+
AD1-77a	486-489	2.99	4.13	8.70	II
AD1-77a	486-489	3.34	4.30	8.70	II
AD1-77a	486-489	0.92	3.75	8.70	+
AD1-79c	492-495	3.11	9.02	7.00	II
AD1-79c	492-495	3.15	6.36	7.00	II
AD1-81a	498-501	2.59	15.93	10.19	II
AD1-81a	498-501	1.83	15.92	10.19	II
AD1-81a	498-501	0.73	15.50	10.19	+
AD1-83c	504-507	4.49	1.63	8.27	II
AD1-83c	504-507	4.77	1.62	8.27	II
AD1-86b	513-516	3.52	8.36	12.00	II
AD1-86b	513-516	3.20	7.25	12.00	II
AD1-86b	513-516	1.63	6.40	12.00	+
AD1-88a	519-522	6.51	0.92	7.09	II
AD1-89a	522-525	3.31	4.69	10.66	II
AD1-89a	522-525	3.29	4.64	10.66	II
AD1-89a	522-525	1.68	3.97	10.66	+
AD1-94-b	540-542.5	7.23	4.89	10.90	II
AD1-94-b	540-542.5	7.08	4.40	10.90	II
AD1-96c	546-549	3.98	16.15	11.21	II
AD1-96c	546-549	4.16	16.70	11.21	II
AD1-96c	546-549	2.84	20.22	11.21	+
AD1-97c	549-552	3.64	15.07	6.72	II
AD1-97c	549-552	2.90	8.27	6.72	II
AD1-97c	549-552	4.04	2.65	6.72	+
AD1-99b	555-558	3.80	18.55	9.97	II
AD1-99b	555-558	2.93	8.60	9.97	II
AD1-99b	555-558	2.06	2.33	9.97	+
AD1-102b	564-567.6	4.16	13.34	3.86	II
AD1-102b	564-567.6	3.38	5.10	3.86	II

AD1-102b	564-567.6	2.87	11.72	3.86	+
AD1-104-b	570.65-573.7	5.35	1.15	3.62	II
AD1-104-b	570.65-573.7	5.41	1.23	3.62	II
AD1-104-b	570.65-573.7	4.73	1.25	3.62	II
AD1-104-b	570.65-573.7	5.00	1.38	3.62	II
AD1-113-b	598.1-601.15	3.66	4.64	2.20	II
AD1-113-b	598.1-601.15	4.45	5.59	2.20	II
AD1-113-b	598.1-601.15	4.39	6.80	2.20	II
AD1-113-b	598.1-601.15	4.67	5.13	2.20	II

Legend: σ_t is the Brazilian tensile strength, ω is water content at which the test was performed, TOC is total organic carbon in wt%, bedding orientation is symbol II for σ_t parallel to bedding and + for σ_t normal to bedding and NA is for not available data.

4.2 Petrophysical tests results

4.2.1 Raw petrophysical properties

The porosity, Klinkenberg-corrected gas permeability and slip factor values as measured for 236 samples of the Aderet borehole are summarized in Table 7.

Table 7: Results for petrophysical properties

Sample	Depth, m	ϕ, %	K∞, mD	b[n2], psi	TOC, %	bedding orient.
AD1-1a-b	265.3-266.8	38.70	0.05	64.18	8.82	II
AD1-2a-a	266.8-269.3	42.34	0.24	15.25	8.38	II
AD1-2a-b	266.8-269.3	42.27	0.12	32.29	8.38	II
AD1-3a-a	269.5-271	41.79	0.09	40.93	10.65	II
AD1-3a-b	269.5-271	41.30	0.08	54.18	10.65	II
AD1-3a-o1	269.5-271	31.35	0.03	37.08	10.65	+
AD1-4c-a	271.6-274.65	39.56	0.07	59.69	11.00	II
AD1-4c-b	271.6-274.65	39.45	0.06	62.24	11.00	II
AD1-4c-o	271.6-274.65	39.53	0.02	68.43	11.00	+
AD1-4c-o	271.6-274.65	41.91	0.04	25.28	11.00	+
AD1-5b-a	274.65-277.7	41.88	0.08	40.02	8.69	II
AD1-5b-b	274.65-277.7	43.09	0.08	39.88	8.69	II
AD1-5b-o2	274.65-277.7	38.03	0.04	15.17	8.69	+
AD1-6c-a	277.7-280.75	41.29	0.05	66.94	9.16	II
AD1-6c-b	277.7-280.75	42.09	0.06	51.15	9.16	II
AD1-6c-o1	277.7-280.75	37.52	0.04	0.10	9.16	+
AD1-7b-a	280.75-283.8	42.12	0.18	4.83	9.46	II
AD1-7b-b	280.75-283.8	41.17	0.12	26.68	9.46	II
AD1-7b-o1	280.75-283.8	39.08	0.01	55.66	9.46	+
AD1-8b-a	283.8-286.85	41.42	0.12	41.95	8.03	II
AD1-8b-b	283.8-286.85	41.40	0.13	19.22	8.03	II
AD1-8b-o1	283.8-286.85	36.73	0.02	0.00	8.03	+
AD1-9a-a	286.85-289.9	37.29	0.09	25.48	7.80	II

AD1-9a-b	286.85-289.9	37.00	0.50	0.92	7.80	II
AD1-9a-o1	286.85-289.9	31.23	0.01	7.51	7.8	+
AD1-10a-b	289.9-291.4	35.83	1.34	6.69	11.77	II
AD1-11a-a	291.4-292.95	39.92	0.12	25.90	10.94	II
AD1-11a-b	291.4-292.95	31.11	0.05	33.85	10.94	II
AD1-11a-o	291.4-292.95	35.92	0.01	69.24	10.94	+
AD1-11b-a	291.4-292.95	37.27	0.43	2.93	12.12	II
AD1-11b-b	291.4-292.95	38.28	0.23	9.90	12.12	II
AD1-11b-o1	291.4-292.95	32.91	0.03	1.24	12.12	+
AD1-12b-a	292.95-296	40.63	0.13	26.32	10.82	II
AD1-12b-b	292.95-296	39.58	0.11	38.04	10.82	II
AD1-12b-o1	292.95-296	34.39	0.01	42.12	10.82	+
AD1-13b-a	296-299.05	39.08	0.10	45.19	11.21	II
AD1-13b-b	296-299.05	40.13	0.12	35.73	11.21	II
AD1-13b-o1	296-299.05	37.19	0.01	53.81	11.21	+
AD1-14a-a	299.05-302.1	40.52	0.07	54.64	7.58	II
AD1-14a-o2	299.05-302.1	37.77	0.03	19.03	7.58	+
AD1-15a-a	302.1-305.15	42.98	0.15	27.73	10.26	II
AD1-15a-b	302.1-305.15	40.12	0.13	35.38	10.26	II
AD1-15a-o1	302.1-305.15	37.43	0.04	4.77	10.26	+
AD1-16a-a	305.15-308.2	41.82	0.13	33.07	9.5	II
AD1-16a-b	305.15-308.2	41.15	0.12	35.08	9.5	II
AD1-16a-o1	305.15-308.2	37.48	0.03	0.00	9.5	+
AD1-17a-a	308.2-311.25	40.21	0.09	26.30	7.63	II
AD1-17a-b	308.2-311.25	40.30	0.11	23.94	7.63	II
AD1-17a-o1	308.2-311.25	36.88	0.02	0.00	7.63	+
AD1-19b-o1	314.3-317.35	33.03	0.02	8.33	13.85	+
AD1-20a-a	317.35-320.4	39.48	0.05	50.20	8.50	II
AD1-20a-a1	317.35-320.4	41.96	0.08	22.05	8.5	II
AD1-20a-b	317.35-320.4	41.25	0.11	11.20	8.5	II
AD1-20a-o	317.35-320.4	39.62	0.03	1.94	8.50	+
AD1-20c-b	317.35-320.4	39.33	0.10	3.48	10.59	II
AD1-20c-o1	317.35-320.4	35.33	0.01	0.00	10.59	+
AD1-22b-o1	323.45-326.5	43.25	0.01	0.00	11.29	+
AD1-23a-a	326.5-329.55	40.97	0.06	52.80	9.78	II
AD1-23a-b	326.5-329.55	44.14	0.06	39.80	9.78	II
AD1-23a-o1	326.5-329.55	36.59	0.02	0.00	9.78	+
AD1-24a-a	329.55-332.6	46.18	0.06	45.48	11.63	II
AD1-24a-b	329.55-332.6	39.89	0.13	20.39	11.63	II
AD1-24a-o1	329.55-332.6	35.40	0.01	0.00	11.63	+
AD1-26a-a	335.65-338.7	38.77	0.18	22.60	11.1	II
AD1-26a-b	335.65-338.7	40.05	0.18	25.92	11.1	II
AD1-26a-o1	335.65-338.7	33.87	0.01	16.95	11.1	+
AD1-27c-a	338.7-341.75	36.90	1.06	5.44	13.21	II
AD1-27c-o1	338.7-341.75	32.44	0.06	29.88	13.21	+

AD1-28a-a	341.75-344.8	40.99	0.38	14.24	9.28	II
AD1-28a-b	341.75-344.8	40.06	0.84	7.83	9.28	II
AD1-28a-o1	341.75-344.8	37.11	0.02	0.00	9.28	+
AD1-29c-a	344.8 - 347.85	40.93	0.23	21.19	10.20	II
AD1-29c-b	344.8 - 347.85	41.66	0.20	29.51	10.20	II
AD1-29c-o1	344.8 - 347.85	36.96	0.05	0.65	10.2	+
AD1-30a-a	348.77-350.82	27.26	0.01	80.63	4.75	II
AD1-30a-b	348.77-350.82	27.64	0.01	77.73	4.75	II
AD1-30a-o1	348.77-350.82	15.93	0.00	0.00	4.75	+
AD1-30a-o2	348.77-350.82	14.60	0.00	7.68	4.75	+
AD1-31a-a	350.82-352	42.32	0.13	37.01	11.12	II
AD1-31a-b	350.82-352	42.87	0.11	47.35	11.12	II
AD1-31a-o1	350.82-352	39.38	0.04	47.13	11.12	+
AD1-31a-o2	350.82-352	36.95	0.07	4.16	11.12	+
AD1-32a-a1	352-353	36.29	0.04	62.40	12.61	II
AD1-32a-a2	352-353	35.86	0.04	60.28	12.61	II
AD1-32a-b	352-353	35.34	0.04	58.07	12.61	II
AD1-32a-o	352-353	36.52	0.01	68.26	12.61	+
AD1-33a-a	353.81-356.4	35.05	0.05	44.42	11.15	II
AD1-33a-b	353.81-356.4	33.52	0.03	65.43	11.15	II
AD1-33a-o	353.81-356.4	39.17	0.02	56.34	11.15	+
AD1-33a-o1	353.81-356.4	37.09	0.04	0.31	11.15	+
AD1-34b-b	356.9-359.95	40.94	0.17	28.15	11.25	II
AD1-34b-o	356.9-359.95	41.17	0.02	70.42	11.25	+
AD1-35c-a	359.95-363	41.25	0.17	34.57	11.78	II
AD1-35c-b	359.95-363	42.24	0.26	21.99	11.78	II
AD1-35c-o1	359.95-363	38.20	0.05	44.48	11.78	+
AD1-36a-a	363-366.05	40.18	0.13	33.76	10.36	II
AD1-36a-b	363-366.05	39.01	0.17	31.40	10.36	II
AD1-36a-o	363-366.05	39.36	0.02	66.39	10.36	+
AD1-36a-o1	363-366.05	33.57	0.17	14.25	10.36	+
AD1-37b-a	366.3-369.3	8.31	0.00	0.00	3.20	II
AD1-37b-b	366.3-369.3	6.33	0.00	0.00	3.20	II
AD1-37b-o1	366.3-369.3	6.13	0.00	0.00	3.20	+
AD1-38c-a	369.3-372.3	39.57	0.26	23.95	14.00	II
AD1-38c-b	369.3-372.3	39.33	0.29	23.83	14.00	II
AD1-38c-o	369.3-372.3	39.31	0.06	9.31	14.00	+
AD1-38c-o2	369.3-372.3	44.73	0.09	6.98	14.00	+
AD1-39b-o1	372.3-375.3	37.74	0.03	45.18	14.54	+
AD1-40b-a	375-378.3	41.70	0.27	31.99	15.08	II
AD1-40b-b	375-378.3	41.21	0.27	26.84	15.08	II
AD1-40b-o	375-378.3	39.82	0.12	39.10	15.08	+
AD1-40b-o1	375-378.3	38.01	0.08	33.88	15.08	+
AD1-42b-b	381.3-384.3	42.24	0.19	11.41	14.25	II
AD1-42b-o1	381.3-384.3	34.81	0.02	0.24	14.25	+

AD1-43b-a	384.3-387.1	38.36	0.22	18.57	17.48	II
AD1-43b-b	384.3-387.1	37.36	0.23	24.40	17.48	II
AD1-43b-o	384.3-387.1	44.69	0.03	4.09	17.48	+
AD1-47a-a	396.1-399	36.48	0.17	30.95	16.85	II
AD1-47a-b	396.1-399	40.08	0.12	26.41	16.85	II
AD1-47a-o1	396.1-399	31.10	0.01	34.22	16.85	+
AD1-49b-a	402.1-405.1	37.63	0.06	45.39	14.95	II
AD1-49b-b	402.1-405.1	37.97	0.12	26.38	14.95	II
AD1-49b-o1	402.1-405.1	34.61	0.01	30.59	14.95	+
AD1-50c-a	405-408	43.63	0.15	17.71	18.05	II
AD1-50c-b	405-408	37.22	0.14	31.74	18.05	II
AD1-50c-o1	405-408	34.49	0.02	16.54	18.05	+
AD1-51a-a	408-411	41.28	0.04	57.46	NA	II
AD1-51a-b	408-411	40.47	0.04	47.05	NA	II
AD1-51a-o1	408-411	35.25	0.04	12.71	NA	+
AD1-54a-a	417-420	37.92	0.11	39.80	12.79	II
AD1-54a-b	417-420	39.09	0.09	47.06	12.79	II
AD1-54a-o1	417-420	33.42	0.01	12.65	12.79	+
AD1-54c-a	417-420	38.00	0.18	34.13	NA	II
AD1-54c-b	417-420	37.89	0.21	28.20	NA	II
AD1-55a-a	420-423	39.09	0.12	38.60	15.88	II
AD1-55a-b	420-423	39.51	0.11	42.44	15.88	II
AD1-55a-o1	420-423	36.32	0.03	58.85	15.88	+
AD1-55b-a	420-423	38.35	0.14	33.19	16.13	II
AD1-55b-b	420-423	38.32	0.15	36.83	16.13	II
AD1-55b-o1	420-423	34.85	0.02	61.06	16.13	+
AD1-56a-a	423-426	39.46	0.04	57.27	17.92	II
AD1-56a-o1	423-426	34.84	0.04	8.33	17.92	+
AD1-57b-a	426-429	38.36	0.08	27.91	16	II
AD1-57b-o1	426-429	34.94	0.02	46.10	16	+
AD1-58b-a	429-432	39.02	0.12	18.87	15.06	II
AD1-58b-b	429-432	39.32	0.22	24.25	15.06	II
AD1-58b-o1	429-432	36.51	0.04	19.54	15.06	+
AD1-61b-a	438-441	38.30	0.05	20.64	19.17	II
AD1-61b-b	438-441	38.58	0.08	6.80	19.17	II
AD1-61b-o1	438-441	34.04	0.03	2.87	19.17	+
AD1-62c-a	441-444	40.08	0.05	46.73	15.82	II
AD1-62c-b	441-444	38.25	0.06	31.21	15.82	II
AD1-62c-o1	441-444	34.62	0.06	2.51	15.82	+
AD1-64b-a	447-450	40.96	0.12	44.14	12.59	II
AD1-64b-b	447-450	40.40	0.11	45.16	12.59	II
AD1-64b-o1	447-450	38.04	0.04	34.12	12.59	+
AD1-64c-o1	447-450	35.36	0.03	28.04	11.3	+
AD1-64c-o2	447-450	35.91	0.02	50.11	11.3	+
AD1-65c-a	450-453	35.67	0.04	54.97	7.94	II

AD1-65c-b	450-453	40.37	0.05	47.46	7.94	II
AD1-65c-o1	450-453	33.44	0.05	8.58	7.94	+
AD1-67c-a	456-459	34.44	0.10	1.20	5.33	II
AD1-67c-o1	456-459	30.06	0.02	67.58	5.33	+
AD1-68a-a	459-462	34.73	0.06	8.92	6.05	II
AD1-68a-b	459-462	34.82	0.07	0.15	6.05	II
AD1-68a-o1	459-462	31.75	0.03	13.01	6.05	+
AD1-71c-a	468-471	38.51	0.19	8.22	12.12	II
AD1-71c-b	468-471	39.49	0.06	3.92	12.12	II
AD1-71c-o1	468-471	35.95	0.02	1.04	12.12	+
AD1-72a-b	471-474	42.46	0.05	51.44	9.50	II
AD1-72a-o1	471-474	35.76	0.03	45.69	9.5	+
AD1-73c-a	474-477	33.99	0.07	23.11	7.19	II
AD1-73c-b	474-477	33.40	0.06	23.66	7.19	II
AD1-73c-o1	474-477	31.24	0.06	24.63	7.19	+
AD1-75b-a	480-483	38.46	0.05	46.73	9.26	II
AD1-75b-b	480-483	38.25	0.06	28.23	9.26	II
AD1-75b-o1	480-483	36.44	0.05	6.68	9.26	+
AD1-76b-a	483-486	39.38	0.07	33.43	10.18	II
AD1-76b-b	483-486	40.19	0.08	14.90	10.18	II
AD1-76b-o1	483-486	37.56	0.02	66.77	10.18	+
AD1-77a-a	486-489	40.15	0.19	3.51	9.287	II
AD1-77a-b	486-489	40.98	0.12	22.88	9.287	II
AD1-77a-o1	486-489	36.79	0.04	7.32	9.287	+
AD1-78b-b	489-492	36.92	0.13	26.90	9.91	II
AD1-78b-o1	489-492	32.40	0.01	0.00	9.91	+
AD1-79c-a	492-495	36.81	0.02	0.00	9.55	II
AD1-79c-b	492-495	36.33	0.02	31.05	9.55	II
AD1-79c-o1	492-495	27.15	0.00	0.00	9.55	+
AD1-80a-a	495-498	27.84	0.01	35.09	5.00	II
AD1-80a-b	495-498	27.83	0.02	9.85	5.00	II
AD1-80a-o1	495-498	21.42	0.00	0.00	5	+
AD1-81a-a	498-501	33.62	0.43	5.85	10	II
AD1-81a-b	498-501	34.44	0.76	4.41	10	II
AD1-81a-o1	498-501	26.28	0.00	0.00	10	+
AD1-83c-b	504-507	36.70	0.07	2.14	8.12	II
AD1-83c-o1	504-507	32.93	0.01	5.81	8.12	+
AD1-84c-a	507-510	35.85	0.03	11.51	9.40	II
AD1-84c-b	507-510	31.94	0.03	9.29	9.40	II
AD1-84c-o1	507-510	28.32	0.02	6.61	9.4	+
AD1-85b-a	510-513	31.83	0.02	31.32	11.56	II
AD1-85b-b	510-513	31.57	0.01	29.59	11.56	II
AD1-85b-o1	510-513	15.82	0.00	0.00	11.56	+
AD1-86b-b	513-516	32.96	0.16	14.01	9.96	II
AD1-86b-o1	513-516	32.43	0.02	1.84	9.96	+

AD1-87b-a	516-519	35.69	0.08	24.05	13.1	II
AD1-87b-b	516-519	36.25	0.17	6.54	13.1	II
AD1-87b-o1	516-519	31.15	0.01	5.96	13.1	+
AD1-88a-a	519-522	41.03	0.06	1.08	7.09	II
AD1-88a-b	519-522	31.02	0.06	13.79	7.09	II
AD1-88a-o1	519-522	36.94	0.03	0.81	7.09	+
AD1-88a-o2	519-522	30.00	0.02	0.48	7.09	+
AD1-89a-o1	522-525	32.04	0.02	0.44	10.95	+
AD1-91a-a	528-531	35.13	0.29	2.60	7.14	II
AD1-91a-o1	528-531	33.12	0.06	26.99	7.14	+
AD1-96c-a	546-549	32.62	0.14	5.51	12.7	II
AD1-96c-o1	546-549	28.34	0.01	4.47	12.7	+
AD1-97c-a	549-552	33.81	0.05	1.09	6.23	II
AD1-97c-b	549-552	31.87	0.05	1.04	6.23	II
AD1-97c-o1	549-552	27.29	0.01	22.59	6.23	+
AD1-99b-a	555-558	33.61	0.04	36.99	8.02	II
AD1-99b-b	555-558	33.73	0.05	22.86	8.02	II
AD1-99b-o1	555-558	32.80	0.02	13.89	8.02	+
AD1-101b-b	561-564	27.47	0.05	0.16	3.82	II
AD1-101b-o1	561-564	26.87	0.02	3.10	3.82	+
AD1-102b-a	564-567.6	28.93	0.07	7.55	2.72	II
AD1-102b-b	564-567.6	28.80	0.08	4.74	2.72	II
AD1-102b-o1	564-567.6	25.64	0.03	27.51	2.72	+
AD1-104b-a	570.65-573.7	28.16	0.02	66.24	3.83	II
AD1-104b-b	570.65-573.7	29.75	0.03	67.35	3.83	II
AD1-104b-o	570.65-573.7	32.60	0.01	72.82	3.83	+
AD1-104c-a	570.65-573.7	27.98	0.03	55.95	2.70	II
AD1-104c-b	570.65-573.7	28.23	0.03	56.63	2.70	II
AD1-104c-o	570.65-573.7	26.36	0.02	62.73	2.70	+
AD1-113b-a	598.1-601.15	24.60	0.02	64.03	1.91	II
AD1-113b-3a	598.1-601.15	26.20	0.02	69.88	1.91	II
AD1-113b-b	598.1-601.15	28.74	0.02	70.03	1.91	II
AD1-113b-o	598.1-601.15	35.19	0.01	67.11	1.91	+

Legend: φ is the porosity, κ_∞ is the Klinkenberg-corrected gas permeability, b is the Klinkenberg slip factor, TOC is total organic carbon in wt% and bedding orientation is symboled II for flow along the bedding planes and + for flow normal to bedding planes; NA is for not available data.

4.2.2 Results of petrophysical properties after thermal conversion

The effect of thermal conversion of the kerogen and the release of volatile matter formed (e.g. H2O, CO2, H, H2S, N and liquid and gaseous hydrocarbons) on the petrophysical properties is described by performing retort experiments (pyrolysis) and measuring their effect on the petrophysical properties. The retort experiments were performed using pressure regulated semi-batch reactors manufactured by Parr Instruments Inc. (Model 4622) and

situated at the geochemistry laboratory (Figure 27). Three sets of samples (a total of 137) were chosen randomly for these experiments. Each set was uniformly heated at a constant heating rate and back pressure to full conversion. A small percentage of samples broke during the pyrolysis, so that the petrophysical properties could not be measured again.

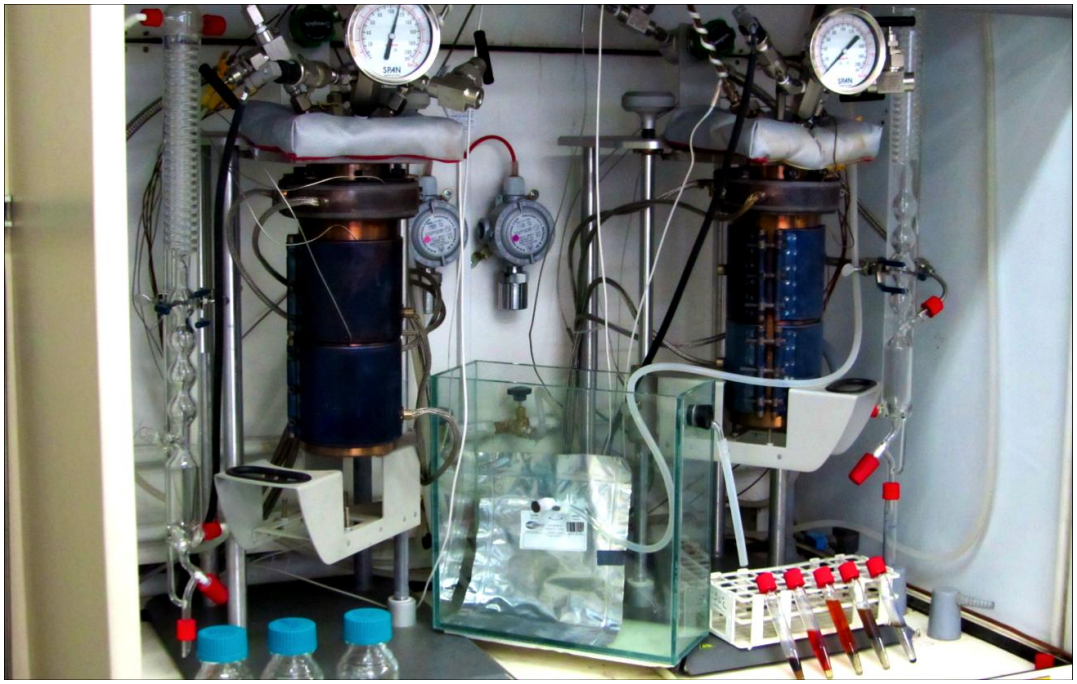

Figure 27: Pressure-regulated semi-batch reactors located at the Geochemistry Laboratory at BGU.

After thermal conversion most of the samples stayed intact while a change in color was detected (Figure 28). Their color changed from light brown-gray to a much darker tone due to the remaining organic matter (formation of residual organic matter).

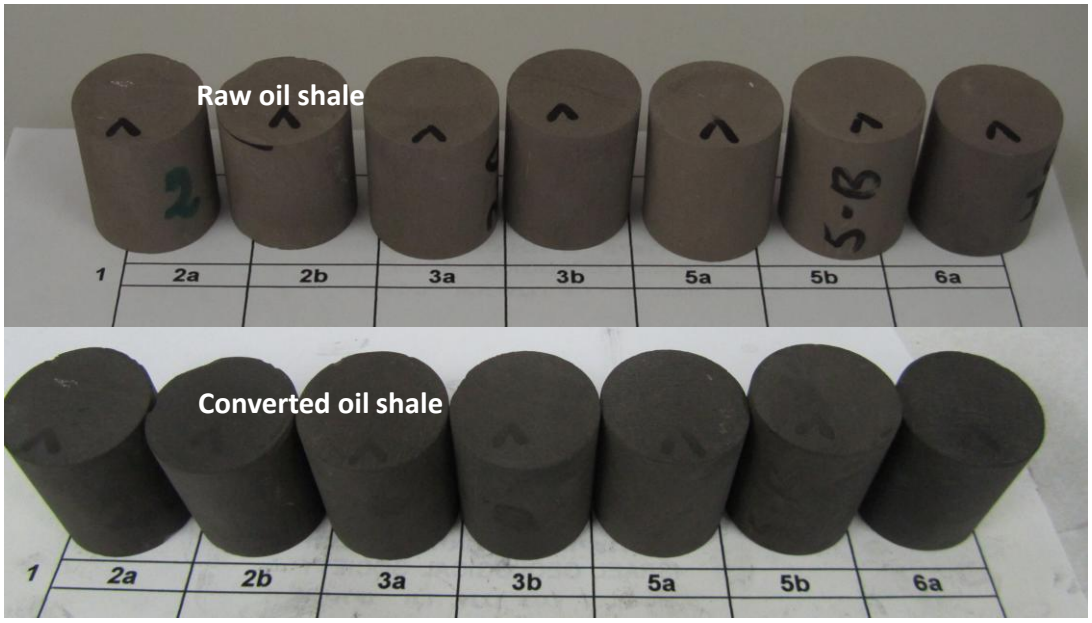

Figure 28: Samples before (top row) and after (bottom row) thermal conversion.

Pyrolysis 1:

This retort experiment was performed on 44 samples. Starting with ~ 200°C they were heated up to 430°C in ramp rate of 5°C per hour with no back pressure applied (0 psi). A total of 43 samples remained whole after the process; their petrophysical properties after the pyrolysis are summarized in Table 8.

Table 8: Results for petrophysical properties pre and post pyrolysis no. 1

Sample	ϕ, %	K∞, mD	b[n2], psi	TOC, %	ϕ', %	K∞', mD	b[n2]', psi	TOC', %
AD1-4c-a	39.56	0.07	59.69	11.00	50.91	0.21	47.36	NA
AD1-4c-b	39.45	0.06	62.24	11.00	51.26	0.22	45.17	4.22
AD1-11a-a	39.92	0.12	25.90	10.94	56.17	0.42	29.27	6.92
AD1-11a-b	31.11	0.05	33.85	10.94	51.66	0.46	25.31	NA
AD1-28a-a	40.99	0.38	14.24	9.28	53.23	1.05	15.54	6.76
AD1-28a-b	40.06	0.84	7.83	9.28	52.16	1.53	8.16	7.48
AD1-29c-b	41.66	0.20	29.51	10.20	51.97	0.55	25.58	6.06
AD1-30a-a	27.26	0.01	80.63	4.75	34.50	0.05	56.68	3.21
AD1-30a-b	27.64	0.01	77.73	4.75	39.31	0.05	55.59	3.22
AD1-31a-a	42.32	0.13	37.01	11.12	53.20	0.57	29.95	5.25
AD1-31a-b	42.87	0.11	47.35	11.12	52.91	0.55	31.18	5.42
AD1-32a-a1	36.29	0.04	62.40	12.61	51.75	0.38	28.80	NA
AD1-32a-a2	35.86	0.04	60.28	12.61	49.69	0.27	38.05	6.62
AD1-32a-b	35.34	0.04	58.07	12.61	49.73	0.41	32.90	7.88
AD1-33a-a	35.05	0.05	44.42	11.15	50.17	0.53	27.75	9.51
AD1-33a-b	33.52	0.03	65.43	11.15	51.09	0.57	25.50	9.32
AD1-34b-b	40.94	0.17	28.15	11.25	51.43	0.69	28.06	6.35
AD1-35c-a	41.25	0.17	34.57	11.78	51.36	0.88	25.80	6.27

AD1-35c-b	42.24	0.26	21.99	11.78	51.73	0.88	23.98	6.22
AD1-36a-a	40.18	0.13	33.76	10.36	49.11	0.50	30.39	6.71
AD1-36a-b	39.01	0.17	31.40	10.36	48.63	0.60	23.53	6.21
AD1-40b-a	41.70	0.27	31.99	15.08	55.65	2.25	17.09	8.67
AD1-40b-b	41.21	0.27	26.84	15.08	54.61	2.26	16.35	NA
AD1-54a-a	37.92	0.11	39.80	12.79	54.72	2.24	15.69	NA
AD1-54a-b	39.09	0.09	47.06	12.79	54.25	2.18	16.36	10.77
AD1-54c-a	38.00	0.18	34.13	NA	55.26	2.82	14.07	NA
AD1-54c-b	37.89	0.21	28.20	NA	53.77	2.75	14.62	8.15
AD1-55a-a	39.09	0.12	38.60	15.88	59.67	2.43	14.85	8.11
AD1-55a-b	39.51	0.11	42.44	15.88	56.70	2.44	14.81	NA
AD1-55b-a	38.35	0.14	33.19	16.13	53.32	2.61	15.66	9.59
AD1-55b-b	38.32	0.15	36.83	16.13	56.02	2.69	15.10	NA
AD1-64b-a	40.96	0.12	44.14	12.59	52.70	1.39	19.89	6.21
AD1-64b-b	40.40	0.11	45.16	12.59	61.40	1.25	21.04	6.12
AD1-104b-a	28.16	0.02	66.24	3.83	45.02	0.11	34.82	NA
AD1-104b-b	29.75	0.03	67.35	3.83	36.68	0.19	12.94	NA
AD1-104b-o	32.60	0.01	72.82	3.83	41.42	0.12	3.64	2.12
AD1-104c-a	27.98	0.03	55.95	2.70	32.16	0.09	45.27	1.69
AD1-104c-b	28.23	0.03	56.63	2.70	32.74	0.10	39.49	1.24
AD1-104c-o	26.36	0.02	62.73	2.70	32.08	0.08	26.51	NA
AD1-113b-a	24.60	0.02	64.03	1.91	29.10	0.09	6.57	NA
AD1-113b-3a	26.20	0.02	69.88	1.91	28.86	0.04	58.23	1.57
AD1-113b-b	28.74	0.02	70.03	1.91	29.74	0.05	42.98	1.16
AD1-113b-o	35.19	0.01	67.11	1.91	29.93	0.06	5.10	2.12

Legend: φ is the porosity, κ_∞ is the Klinkenberg-corrected gas permeability, b is the Klinkenberg slip factor and TOC is total organic carbon in wt%; the superscript, ', refers to post pyrolysis measurement and NA is for not available data.

Pyrolysis 2:

This retort experiment was performed on 49 samples. Starting with ~ 200°C they were heated up to 430°C in ramp rate of 5°C per hour with applying back pressure of 150 psi. A total of 45 samples remained whole after the process; their petrophysical properties after the pyrolysis are summarized in Table 9.

Table 9: Results for petrophysical properties pre and post pyrolysis no. 2

Sample	ϕ, %	K∞, mD	b[n2], psi	TOC, %	ϕ', %	K∞', mD	b[n2]', psi	TOC', %
AD1-2a-a	42.34	0.24	15.25	8.38	49.63	0.36	35.03	5.26
AD1-2a-b	42.27	0.12	32.29	8.38	49.12	0.28	45.06	NA
AD1-3a-a	41.79	0.09	40.93	10.65	50.23	0.50	33.61	6.31
AD1-3a-b	41.30	0.08	54.18	10.65	50.08	0.50	33.41	6.30
AD1-5b-a	41.88	0.08	40.02	8.69	51.22	0.31	42.61	5.43

AD1-5b-b	43.09	0.08	39.88	8.69	50.82	0.32	39.61	NA
AD1-6c-a	41.29	0.05	66.94	9.16	49.04	0.25	44.31	NA
AD1-6c-b	42.09	0.06	51.15	9.16	51.49	0.26	43.39	5.62
AD1-7b-a	42.12	0.18	4.83	9.46	49.79	0.23	45.80	NA
AD1-7b-b	41.17	0.12	26.68	9.46	49.50	0.30	30.55	5.93
AD1-8b-a	41.42	0.12	41.95	8.03	50.08	0.29	32.45	5.05
AD1-11b-a	37.27	0.43	2.93	12.12	48.64	0.78	20.06	7.71
AD1-13b-a	39.08	0.10	45.19	11.21	49.79	0.48	26.61	NA
AD1-13b-b	40.13	0.12	35.73	11.21	49.95	0.51	24.16	7.43
AD1-14a-a	40.52	0.07	54.64	7.58	47.99	0.24	45.26	4.92
AD1-15a-a	42.98	0.15	27.73	10.26	49.85	0.70	20.79	6.78
AD1-15a-b	40.12	0.13	35.38	10.26	49.11	0.50	27.82	6.59
AD1-17a-a	40.21	0.09	26.30	7.63	48.78	0.24	46.41	NA
AD1-17a-b	40.30	0.11	23.94	7.63	48.58	0.30	33.48	4.82
AD1-20a-a	39.48	0.05	50.20	8.50	48.64	0.21	45.00	5.62
AD1-23a-a	40.97	0.06	52.80	9.78	48.99	0.29	41.52	NA
AD1-23a-b	44.14	0.06	39.80	9.78	52.84	0.29	40.19	6.22
AD1-24a-a	46.18	0.06	45.48	11.63	49.82	0.36	38.34	8.16
AD1-24a-b	39.89	0.13	20.39	11.63	50.45	0.44	31.56	8.43
AD1-27c-a	36.90	1.06	5.44	13.21	47.64	6.17	9.51	8.51
AD1-37b-a	8.31	0.00	0.00	3.20	12.84	0.05	19.43	NA
AD1-37b-b	6.33	0.00	0.00	3.20	12.77	0.05	12.94	1.81
AD1-38c-b	39.33	0.29	23.83	14.00	49.86	3.50	11.83	8.84
AD1-42b-b	42.24	0.19	11.41	14.25	50.25	1.54	17.64	9.67
AD1-43b-b	37.36	0.23	24.40	17.48	49.47	2.84	14.57	11.66
AD1-47a-b	40.08	0.12	26.41	16.85	52.28	1.01	22.54	NA
AD1-50c-b	37.22	0.14	31.74	18.05	51.12	4.59	11.23	11.57
AD1-61b-a	38.30	0.05	20.64	19.17	50.86	6.46	8.99	12.96
AD1-61b-b	38.58	0.08	6.80	19.17	50.40	6.41	8.99	13.00
AD1-62c-a	40.08	0.05	46.73	15.82	54.69	4.83	10.47	10.90
AD1-62c-b	38.25	0.06	31.21	15.82	51.57	4.89	10.52	10.78
AD1-65c-a	35.67	0.04	54.97	7.94	43.07	0.98	20.89	NA
AD1-65c-b	40.37	0.05	47.46	7.94	42.70	1.07	20.49	5.50
AD1-72a-b	42.46	0.05	51.44	9.50	49.04	0.58	26.89	6.76
AD1-80a-a	27.84	0.01	35.09	5.00	31.77	0.06	15.59	3.78
AD1-80a-b	27.83	0.02	9.85	5.00	30.79	0.06	50.84	NA
AD1-84c-a	35.85	0.03	11.51	9.40	44.78	0.89	20.43	NA
AD1-84c-b	31.94	0.03	9.29	9.40	40.84	0.94	20.85	5.49
AD1-85b-a	31.83	0.02	31.32	11.56	41.66	0.15	41.64	7.51
AD1-85b-b	31.57	0.01	29.59	11.56	41.80	0.12	50.68	7.47

Legend: φ is the porosity, κ_∞ is the Klinkenberg-corrected gas permeability, b is the Klinkenberg slip factor and TOC is total organic carbon in wt%; the superscript, ', refers to post pyrolysis measurement and NA is for not available data.

Pyrolysis 3:

This retort experiment was performed on 49 samples. Starting with ~ 240°C they were heated up to 430°C in ramp rate of approximately 4°C per day with no back pressure applied (0 psi). The petrophysical properties of the 46 remained samples after the pyrolysis are summarized in Table 10.

Table 10: Results for petrophysical properties pre and post pyrolysis no. 3

Sample	ϕ, %	K∞, mD	b[n2], psi	TOC, %	ϕ', %	K∞', mD	b[n2]', psi	TOC', %
AD1-8b-b	41.40	0.13	19.22	8.03	49.68	0.21	40.37	4.70
AD1-12b-a	40.63	0.13	26.32	10.82	51.56	0.41	30.52	6.67
AD1-12b-b	39.58	0.11	38.04	10.82	50.60	0.44	30.06	NA
AD1-16a-b	41.15	0.12	35.08	9.50	50.80	0.29	33.89	5.54
AD1-20a-a1	41.96	0.08	22.05	8.50	50.87	0.18	47.12	5.31
AD1-20a-b	41.25	0.11	11.20	8.50	49.93	0.19	43.53	NA
AD1-20c-b	39.33	0.10	3.48	10.59	49.99	0.16	42.76	6.64
AD1-26a-a	38.77	0.18	22.60	11.10	50.24	0.90	13.16	7.51
AD1-26a-b	40.05	0.18	25.92	11.10	50.40	0.75	15.34	7.52
AD1-49b-a	37.63	0.06	45.39	14.95	51.31	0.82	20.63	NA
AD1-49b-b	37.97	0.12	26.38	14.95	51.81	1.02	19.10	9.37
AD1-51a-a	41.28	0.04	57.46	NA	62.30	0.97	23.68	6.92
AD1-51a-b	40.47	0.04	47.05	NA	52.41	0.87	23.95	7.04
AD1-56a-a	39.46	0.04	57.27	17.92	52.80	1.72	17.00	10.61
AD1-57b-a	38.36	0.08	27.91	16.00	52.74	1.92	16.07	9.63
AD1-58b-a	39.02	0.12	18.87	15.06	53.02	2.15	15.94	NA
AD1-58b-b	39.32	0.22	24.25	15.06	53.43	2.64	13.53	9.53
AD1-67c-a	34.44	0.10	1.20	5.33	40.81	0.19	31.30	3.20
AD1-68a-a	34.73	0.06	8.92	6.05	41.74	0.18	39.73	3.77
AD1-68a-b	34.82	0.07	0.15	6.05	43.80	0.18	39.53	3.87
AD1-71c-a	38.51	0.19	8.22	12.12	49.94	0.52	22.80	7.38
AD1-71c-b	39.49	0.06	3.92	12.12	51.45	0.45	26.33	7.90
AD1-73c-a	33.99	0.07	23.11	7.19	42.64	0.53	26.89	4.64
AD1-73c-b	33.40	0.06	23.66	7.19	40.29	0.41	26.51	4.87
AD1-75b-a	38.46	0.05	46.73	9.26	48.50	0.39	33.68	4.83
AD1-75b-b	38.25	0.06	28.23	9.26	48.06	0.42	31.47	5.02
AD1-76b-a	39.38	0.07	33.43	10.18	50.40	0.69	21.32	5.83

AD1-76b-b	40.19	0.08	14.90	10.18	51.80	0.65	26.95	5.59
AD1-77a-a	40.15	0.19	3.51	9.29	50.20	0.51	20.92	NA
AD1-77a-b	40.98	0.12	22.88	9.29	50.76	0.44	27.26	5.29
AD1-78b-b	36.92	0.13	26.90	9.91	47.76	0.49	18.77	6.07
AD1-79c-a	36.81	0.02	0.00	9.55	47.10	0.16	32.61	5.71
AD1-79c-b	36.33	0.02	31.05	9.55	47.18	0.27	5.77	5.59
AD1-81a-a	33.62	0.43	5.85	10.00	43.17	1.65	5.80	6.56
AD1-83c-b	36.70	0.07	2.14	8.12	46.20	0.15	39.68	5.33
AD1-86b-b	32.96	0.16	14.01	9.96	46.83	0.85	16.90	7.00
AD1-87b-b	36.25	0.17	6.54	13.10	49.26	0.59	23.51	7.21
AD1-88a-b	31.02	0.06	13.79	7.09	40.40	0.23	31.18	3.76
AD1-91a-a	35.13	0.29	2.60	7.14	41.72	1.15	15.60	4.28
AD1-96c-a	32.62	0.14	5.51	12.70	47.27	0.84	13.68	7.20
AD1-97c-a	33.81	0.05	1.09	6.23	42.95	0.22	3.67	NA
AD1-97c-b	31.87	0.05	1.04	6.23	41.45	0.22	0.84	3.67
AD1-99b-b	33.73	0.05	22.86	8.02	43.24	0.24	35.09	4.23
AD1-101b-b	27.47	0.05	0.16	3.82	33.30	0.20	1.06	2.10
AD1-102b-a	28.93	0.07	7.55	2.72	32.06	0.19	15.90	NA
AD1-102b-b	28.80	0.08	4.74	2.72	32.20	0.16	15.50	1.56

Legend: φ is the porosity, κ_∞ is the Klinkenberg-corrected gas permeability, b is the Klinkenberg slip factor and TOC is total organic carbon in wt%; the superscript, ‘, refers to post pyrolysis measurement and NA is for not available data.

Chapter 5- Mechanical behavior of Shefela oil shale: discussion

5.1 Strength and deformability

The static Young's modulus (*E*) of the Shefela oil shale increases with depth up to a value of 2.8 GPa at the bottom of the Ghareb Formation at 460 m, reaching higher values of up to 9.2 GPa at the underlying Mishash Formation. These higher values are attributed to the change in lithology from bituminous chalk at the Ghareb formation to silicified chalk with lower organic content and lower porosity at the Mishash formation.

The uniaxial compressive strength shows a similar trend, with an average value of 19.4 MPa at the tested interval of the Ghareb Formation (260-460 m) and of 53.8 MPa at the Mishash Formation. The strength (σ_c) and deformability (E) results are plotted against depth in (Figure 29).

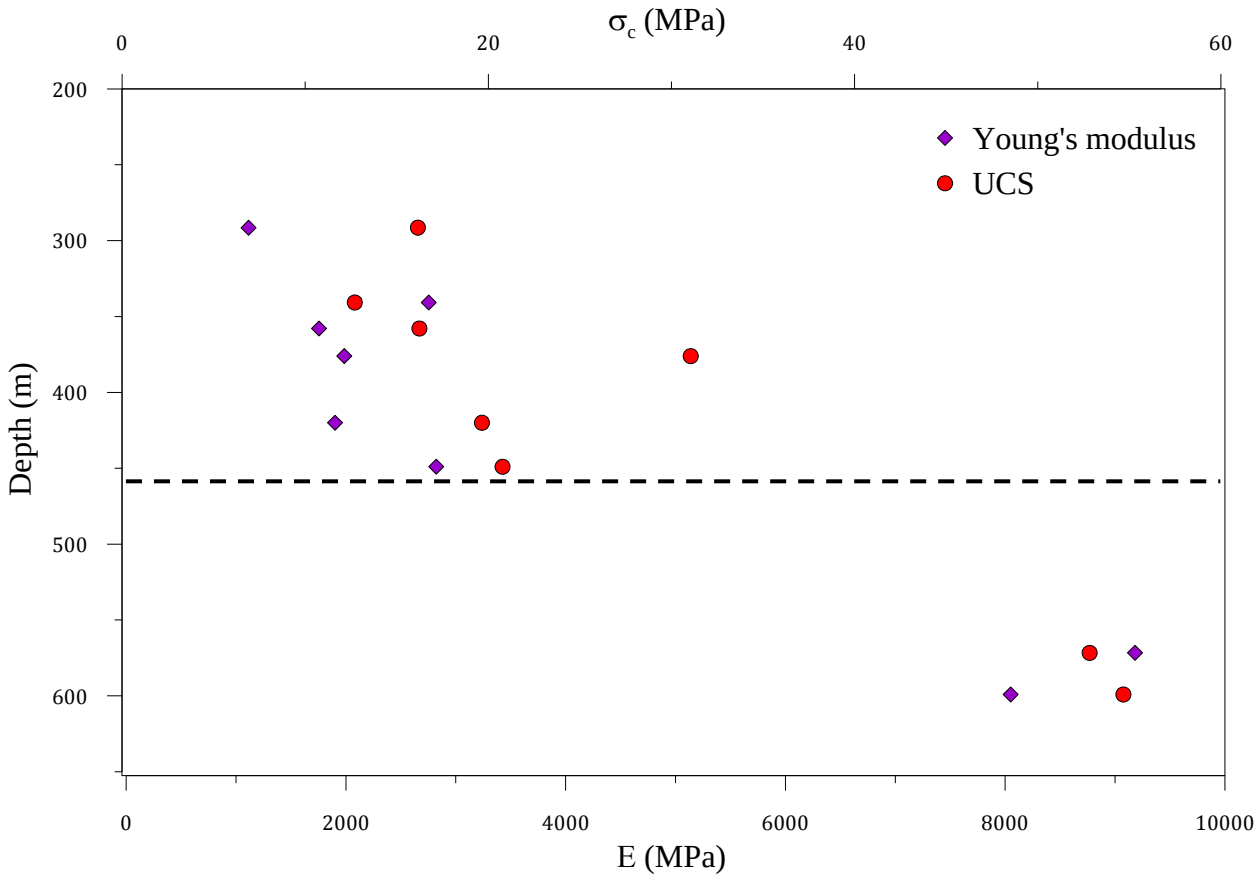

Figure 29: Variation of Uniaxial Compressive Strength and Young's modulus with depth; the dashed line represents the boundary between the Ghareb and the Mishash Formations.

5.2 The effect of water content on the tensile strength

Generally in chalks, the tensile strength decreases with increasing water content. Talesnick et al. (2001) studied the elasticity, strength and anisotropy of high porosity Maresha chalk. To study the tensile strength they performed Brazilian tests, where the tensile component of stress developed in parallel to bedding direction. The influence of water content on the tensile strength was researched as well. The peak tensile strength was found to be maximum ~1 MPa at water content of 3%, then it was drastically reduced over the water content range of ω=3%-10% and finally the tensile strength reduced in a much lower extent over the water content range of ω= 10% - 40% to a minimum value of ~0.3 MPa at ω= ~45%. This trend is well confirmed by our experimental results for the Shefela oil shale (Figure 30). The rate of change in tensile strength seems to decrease with increasing water content, as found in other chalks where this issue was studied (e.g. (Talesnick et al., 2001)). Our results indicate that this behavior is mostly apparent in Mishash silicified and less bituminous chalks (Figure 30b,c), while the tensile strength of Ghareb formation bituminous chalks seems less sensitive to changes in water content (Figure 30a).

When examining each lithology separately, the tensile strength when tested parallel to the bedding appears to be higher than when tested normal to the bedding. In Ghareb the results tend to overlap a bit, but in the upper and lower Mishash this trend is clear. The tensile strength parallel to the bedding is higher by 1.7 on average for Ghareb and by 2.2 on average for Mishash (the compared results were taken from similar depth and water content). This well-defined mechanical anisotropy is observed in the entire range of tested water contents.

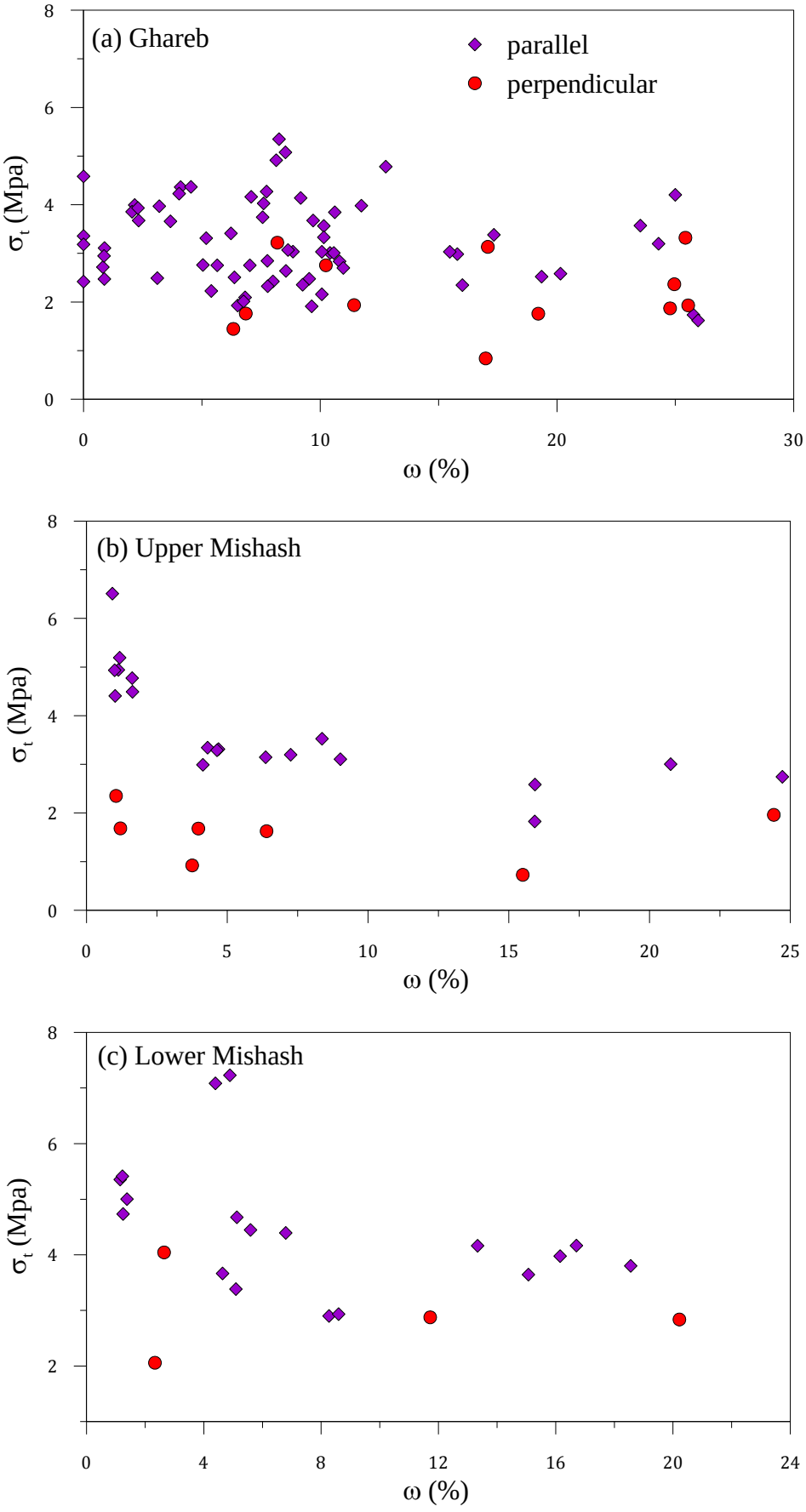

Figure 30: Tensile strength as a function of water content both parallel (purple diamonds) and perpendicular (red circles) to bedding direction: (a) Ghareb Formation; (b) Upper Mishash Formation; (c) Lower Mishash Formation.

5.3 An empirical failure criterion for Shefela oil shale

The results of seven Triaxial compression tests (Figure 31) and one Uniaxial compression test are used to establish an empirical failure criterion for the Shefela oil shale. The empirical failure criterion is developed here for samples extracted from reservoir interval of 335-346 meters.

Two samples that were tested under high confining pressure of 10 MPa (Figure 24f and Figure 24g) exhibited non elastic behavior from onset of loading and therefore were not used in the development of the empirical failure criterion and for the construction of the empirical failure envelope. A linear regression is fitted to the results, showing high applicability of the linear Coulomb-Mohr failure criterion in principal stresses space (Figure 32). The cohesion and the angle of internal friction obtained by regression from the linear Coulomb-Mohr failure criterion are 5.51 MPa and 10.7°, respectively.

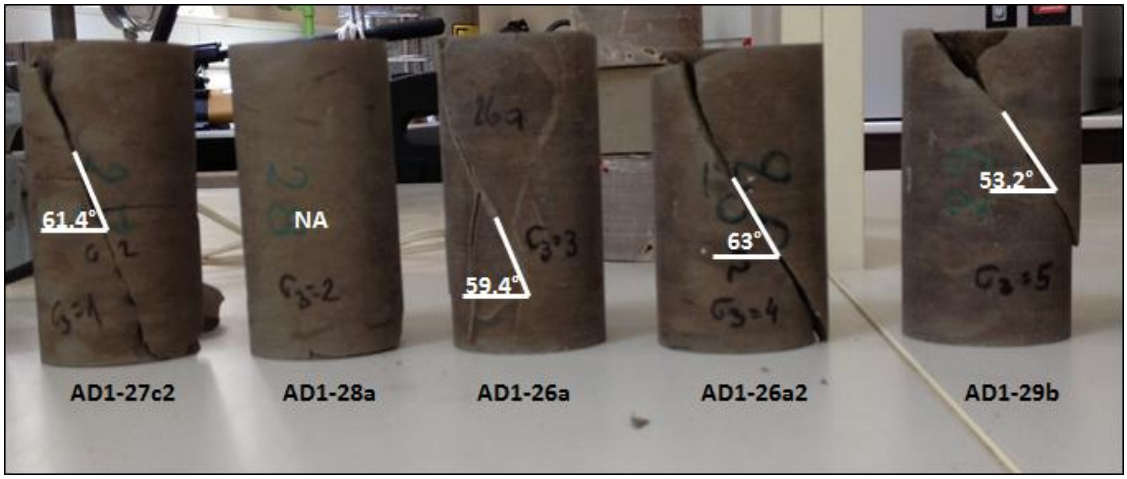

Figure 31: Samples after Triaxial compression tests. The measured angle between the major stress direction and the plane of failure (θ) is marked in white.

Assuming the linear Coulomb – Mohr failure criterion applies, theoretically the angle between the major principal stress axis and the normal to the plane across which shear deformation concentrates is supposed to be $\Theta = 45 + \phi/2 = 55^{o}$. However, the average value of Θ as measured on the sheared cylinders is 59.25° (Figure 31) suggesting an actual internal friction angle of ϕ= 28.5°, if we assume the Coulomb – Mohr failure criterion applies for the Shefela oil shale. This is more than twice the value obtained from linear regression through the peak stresses at failure (Figure 32). This discrepancy indicates that the linear Coulomb – Mohr failure criterion does not capture very well the actual mechanical strength of the Shefela oil shale.

The Griffith failure criterion with its modification for compression (e.g. (Brady and Brown, 2004)) may be more suitable for the following reasons: a) Griffith's criterion has a rigorous theoretical basis, b) it is valid also in the tensile regime, and c) it is not linear in shear stress / normal stress space. Griffith's failure criterion for compression is expressed as follows:

$$\tau^2 = 4T_0(\sigma_n + T_0) \tag{31}$$

Where T_0 is the tensile strength, τ is the shear stress and σ_n is the normal stress. To apply Griffith's criterion for compression an average value of 1.75MPa is assumed for the tensile strength (T_0) of intact rock based on averaging the tensile strength measured with Brazilian tests on samples of the same depth interval (samples AD1-26a, AD1-27c and AD1-28b normal to bedding direction). The obtained Griffith's criterion is plotted in Figure 33.

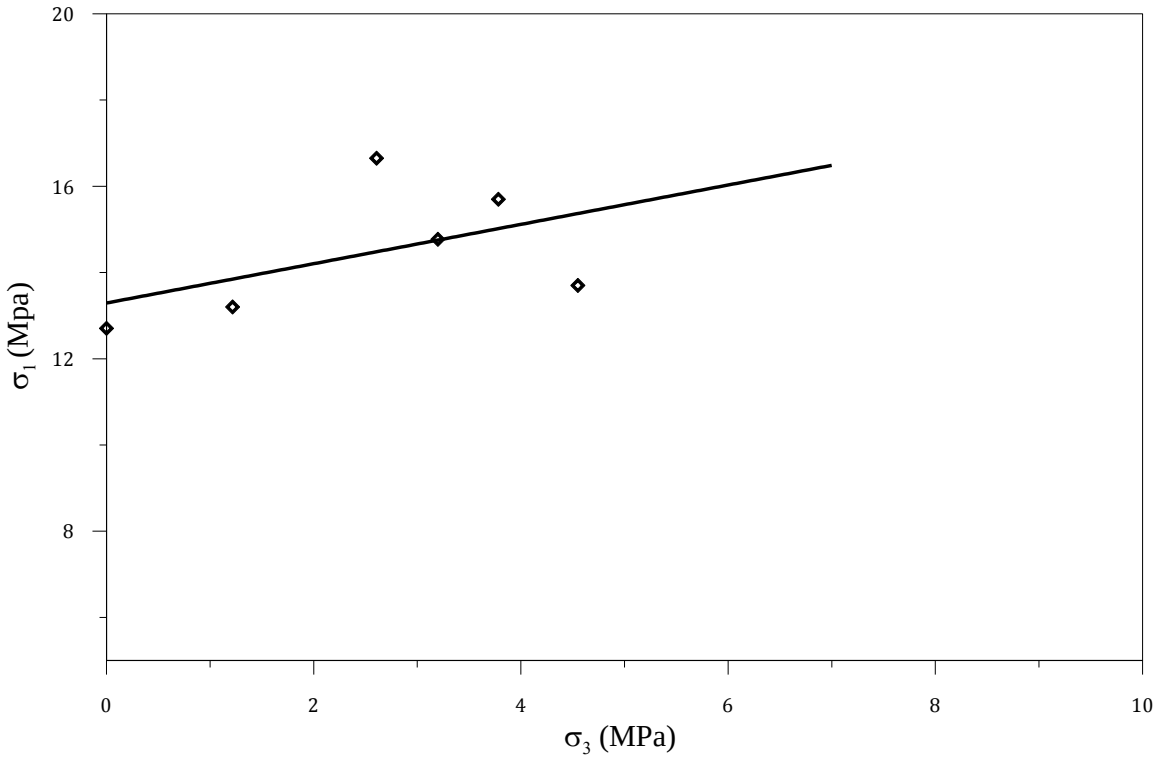

Figure 32: Fitted Coulomb-Mohr criterion in principal stresses space (R square value of 0.78).

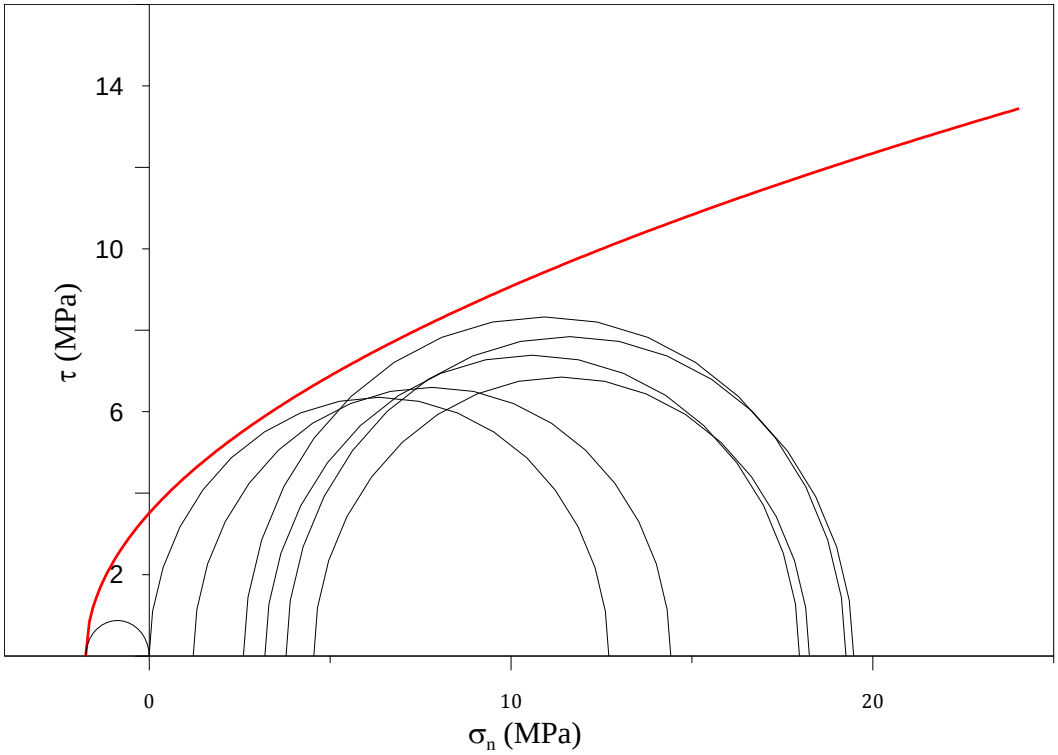

Figure 33: Mohr circles of the measurements in black and fitted Griffith's failure criterion in red, both represented in shear and normal stresses space.

Inspection of Figure 33 reveals that Griffith's criterion is valid for the Shefela oil shale up to a maximum principal compressive stress of σ_1 = 19.5 MPa beyond which the modified Griffith's criterion for compression over predicts the actual strength and is therefore un conservative. Because the rocks *in situ* are not expected to be subjected to stresses greater than 20 MPa it is considered here safe to adopt this failure criterion for the Shefela oil shale. Note that using the average value obtained for the tensile strength results in slight overestimation of the available strength, namely the failure envelope plotted in Figure 33 is slightly un-conservative. This issue can easily be addressed by using some factor of safety when assessing the mean tensile strength.

5.4 Compression-dilation boundary

The anticipated *in situ* production of oil from the oil shale beds in Shefelat Yehuda region will involve drilling vertical and horizontal boreholes for the heating elements and the production processes. Generally, opening an underground space will increase the stresses around that newly created space due to stress concentrations. If the anticipated stress concentrations will exceed the limit between compressional and dilatational behavior of the rock, as defined in lab tests where volumetric strain has been monitored, dilation will ensue,

prompting local permeability increase in areas around the cavities where transition from compressional to dilatational behavior is anticipated. To analyze that possible scenario, an empirical compression-dilation (C-D) boundary is defined here for the Shefela oil shale, using the results of the compression tests (Uniaxial and Triaxial) performed on solid cylinders in direction normal to bedding. Then, the initial *in-situ* stresses and the stress concentrations around an imaginary horizontal tunnel-like opening are calculated for a specific depth, and the expected volume behavior is analyzed.

Hatzor and Heyman (1997) studied the dilation of anisotropic rock salt. they have summarized three empirical compression-dilation boundary models that were previously reviewed by Van Sambeek et al. (1993) and suggested a model for the Mount Sedom rock salt diapir that incorporates anisotropy.

Previous studies introduced empirical compression-dilation boundaries based on data collected from compression tests (Unconfined, True Triaxial and Biaxial) that were performed on different rock salt bodies from across the world. The general form of the boundary in terms of stress invariants is:

$$\sqrt{J_2} = aI^2 + bI + c \tag{32}$$

Where *a*, *b* and *c* are fitting coefficients, I_1 and J_2 are the first and second stress invariants, the values of which are taken here at the point of minimum volume, and defined as:

$$I_1 = \sigma_1 + \sigma_2 + \sigma_3 \tag{33}$$

$$\sqrt{J_2} = \sqrt{\frac{(\sigma_2 - \sigma_3)^2 + (\sigma_3 - \sigma_1)^2 + (\sigma_1 + \sigma_2)^2}{6}} \tag{34}$$

Where σ_1, σ_2, and σ_3 are principal stresses taken at onset of dilation. Four empirical compression-dilation boundary criteria are plotted in Figure 34 including data points that were obtained in this study (the fitting coefficients for the models are summarized in

Table 11). It can be noticed that for low mean normal stress ($\sigma_m=(1/3)I_1$) levels ($0<I_1<50$ MPa; $0<\sigma_m<17$ MPa) the predictions are nearly similar for all criteria as argued by Van Sambeek et al. (1993), however for higher mean stress levels ($I_1>60$ MPa) the deviation between the polynomial expression of Cristescu and Hunsche (1992) and the linear expressions of Spiers et al. (1988) and Ratigan et al. (1991) is large. Hatzor and Heyman

(1997) suggested to use two approximately linear boundaries for low mean stress, an upper for normal compression and a lower for parallel compression and for a large range of mean stress ($0<I_1<100$ MPa) to use two second-order polynomial laws, an upper for normal compression and a lower for parallel compression.

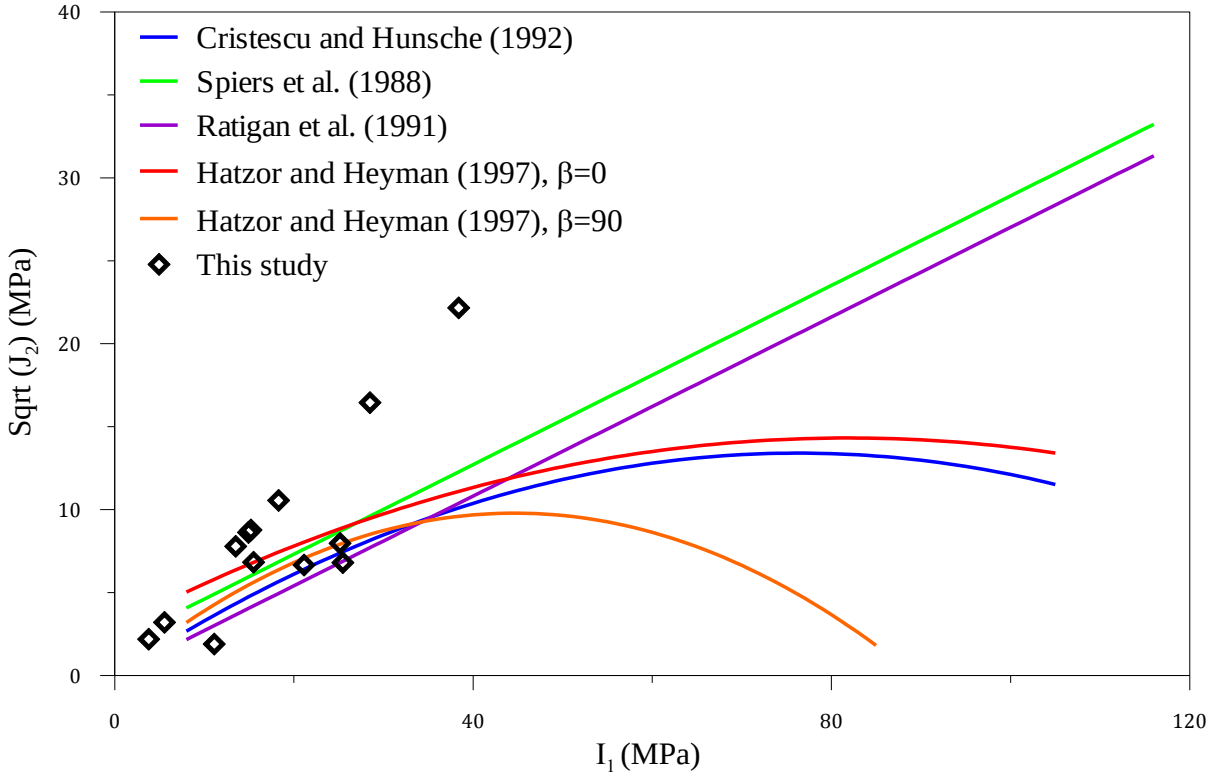

Figure 34: Different models for compression-dilation boundary (after Van Sambeek et al. (1993) and Hatzor and Heyman (1997)) and results of this study.

All the compression tests in this study were performed normal to bedding. The data collected in this research are for relatively low mean normal stress levels (σ_m here is up to ~13 MPa and I_1 is up to ~40 MPa), for normal compression ($\beta=0°$). Our results clearly follow a linear compression – dilation boundary, as generally suggested by Ratigan et al. (1991) and Spiers et al. (1988) and as found specifically for normal compression by Hatzor and Heyman (1997) for low mean normal stress levels. Naturally, since the rock material tested here is chalk, the actual values of the fitting parameters are different. Nevertheless, for relatively low mean normal stress levels of $0< \sigma_m<7$ MPa ($0<I_1<22$ MPa), the C-D boundary for the materials tested here follows closely previously published criteria for rock salts.

Table 11: Summary of coefficients values for the different CD boundaries in terms of stress invariants, the coefficients fit an equation from the form $\sqrt{J_2} = aI_1^2 + bI_1 + c$; β represents the angle between the axis of maximum stress and the anisotropy (bedding) direction (β=0° is compression normal to bedding direction and β=90° is compression parallel to bedding direction)

Model	a	b	c (MPa)
Cristescu and Hunsche (1992)	-0.0023	0.3511	0
Spiers et al. (1988)	0	0.27	1.9
Ratigan et al. (1991)	0	0.27	0
Hatzor and Heyman (1997); β=0°	-0.0017	0.28	2.9
Hatzor and Heyman (1997); β=90°	-0.0048	0.44	0

The best-fit linear curve for the results of this study is shown in Figure 35. The curve separates the sqrt(J2) – I1 space into two zones, the lower is the compression zone and the upper is the dilation zone. The fitting coefficients values for the linear C-D boundary are summarized in Table 12.

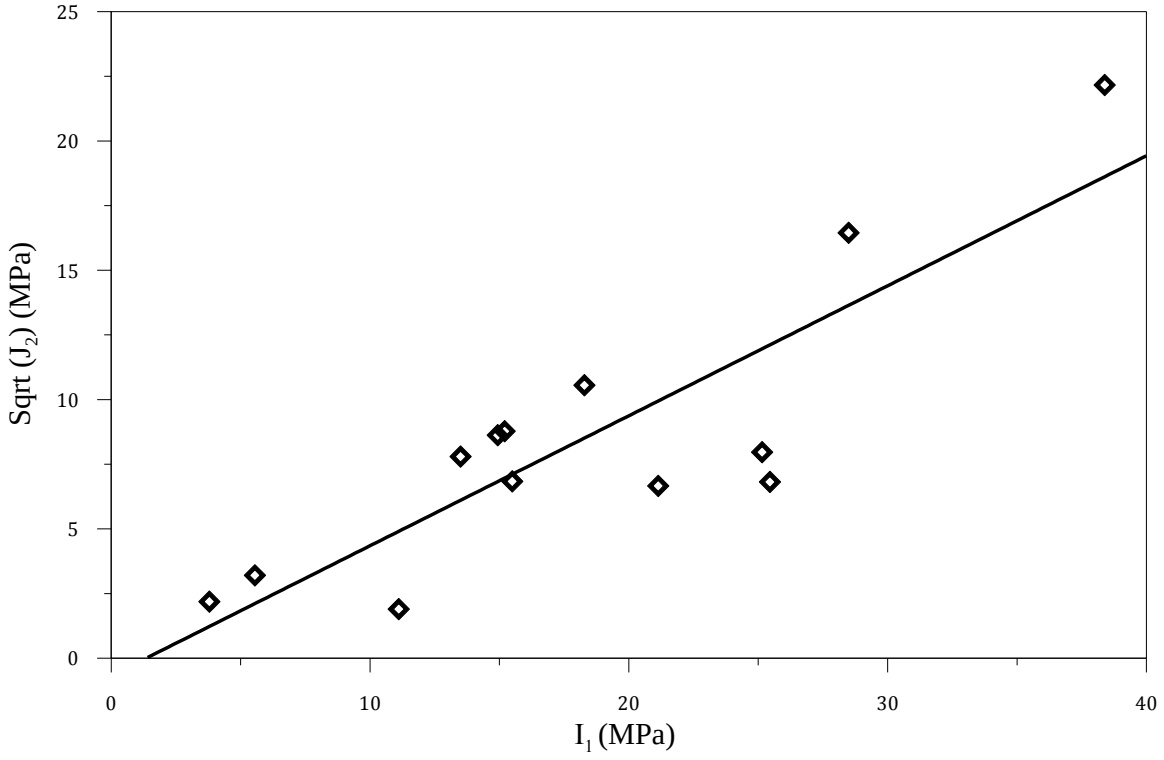

Figure 35: Best-fit linear curve for compression-dilation boundary as found in this study for the Shefela oil shale (R squared value of 0.73).

Table 12: Fitting coefficients values for the C-D boundary of the Shefela oil shale in terms of stress invariants, the coefficients fit an equation from the form of $\sqrt{J_2} = aI_1^2 + bI_1 + c$;

Model	a	b	c (MPa)
Shefela oil shale	0	0.5026	-0.69

The selected depth for the volume change analysis is 450 meters; this is the bottom of the rich zone of the Aderet section, where the TOC values average ~14% (Figure 8). The section includes the Adulam and the Taqyie formations, with combined thickness of 265 meters and an assumed average dry unit weight (γ_d) of 18 kN/m^3. Underlying the Taqyie is the 185 meters thick Ghareb formation with calculated saturated unit weight of 18 (γ_{sat}) kN/m^3.

We assume that the vertical and horizontal stresses are principal stresses, as follows:

$$\sigma_z = \sigma_v = \sigma_1 = \Sigma \gamma_i z_i \tag{35}$$

Where σ_v is the vertical stress that equals the sum of products of unit weights and thicknesses of stratum layers. With the given stratigraphy and densities at 450 meters depth the magnitude of the initial vertical stress is assumed to be σ_v =8.1 MPa. Assuming uniaxial strain conditions ($\varepsilon_h = 0$), then by Hoek's law the horizontal stress is:

$$\sigma_x = \sigma_y = \sigma_h = \sigma_3 = \sigma_v \frac{\nu}{1-\nu} \tag{36}$$

Where σ_h is the horizontal stress and ν is Poisson's ratio which is assumed here to be transversely isotropic ($\nu_x = \nu_y = \nu$), as inferred from our lab tests. From our laboratory experiments the average value of ν is 0.27; then at 450 meters depth the anticipate level of initial horizontal stress is σ_h = 3 MPa. The initial state of stresses is displayed on the stress invariants space, it is clear that the rock is initially in a compressive state (Figure 37).

In 1898 G. Kirsch derived the solution for the stress distribution around a circular hole in a much larger thin plate where far field principal stresses are applied on the boundaries (Kirsch, 1898). The full solution for the stresses around that hole is:

$$\sigma_{rr} = \frac{\sigma_1 + \sigma_3}{2}\left(1 - \frac{a^2}{r^2}\right) - \frac{\sigma_1 - \sigma_3}{2}\left(1 - 4\frac{a^2}{r^2} + 3\frac{a^4}{r^4}\right)cos2\theta \tag{37}$$

$$\sigma_{\theta\theta} = \frac{\sigma_1 + \sigma_3}{2}\left(1 + \frac{a^2}{r^2}\right) + \frac{\sigma_1 - \sigma_3}{2}\left(1 + 3\frac{a^4}{r^4}\right)cos2\theta$$

$$\sigma_{r\theta} = \frac{\sigma_1 - \sigma_3}{2}\left(1 + 2\frac{a^2}{r^2} - 3\frac{a^4}{r^4}\right) sin2\theta$$

Where σ_{rr}, $\sigma_{\theta\theta}$ and $\sigma_{r\theta}$ are total radial, tangential, and shear stresses after the hole is created, r is the radius of the hole, a is the distance from the center of the hole and θ is the orientation angle (see Figure 36).

Using Kirsch solution, let us now examine the change in volumetric behavior of the rock at the side wall and at the roof of an imaginary, circular, horizontal tunnel drilled in the studied basin. From Kirsch's solution the total stresses on the edge of the circular tunnel (r=a) are:

$$\sigma_{\theta\theta} = \sigma_1 + \sigma_3 + 2(\sigma_1 - \sigma_3)cos2\theta \quad (38)$$

$$\sigma_{rr} = 0$$

$$\sigma_{r\theta} = 0$$

For an imaginary horizontal tunnel with a diameter of 10 meters the stress concentrations at the center of the side wall (red dot 1 in Figure 36) are $\sigma_{\theta\theta}$= 21.38 MPa, σ_{rr} =$\sigma_{r\theta}$=0, whereas the stress concentrations at the center of the roof (red dot 2 in Figure 36) are $\sigma_{\theta\theta}$= 0.89 MPa, σ_{rr} =$\sigma_{r\theta}$=0.

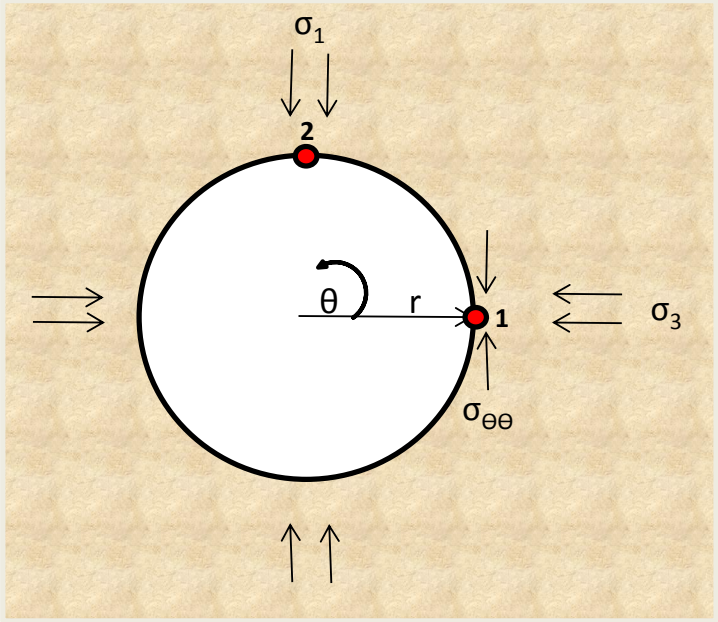

Figure 36: The geometry of the problem for Kirsch's solution. The red dots represent the chosen calculated cases (r=a, θ=0°, 90°).

Represented in a stress invariants space (Figure 37), the rock is now in the dilation region of the linear compression-dilation boundary for both cases. It can be concluded that at the specific chosen depth, tunnel diameter and orientations on the tunnel circumference, upon tunnel construction the deformational regime transfers from compressional to dilational behavior, a process that could prompt permeability increase in the rock mass at close proximity to the tunnel. A more comprehensive analysis can be made to study the volumetric behavior of the rock in other different locations around the opening periphery. Additional Triaxial compression tests should be made to refine the compression – dilation boundary and expand it to larger mean stress values.

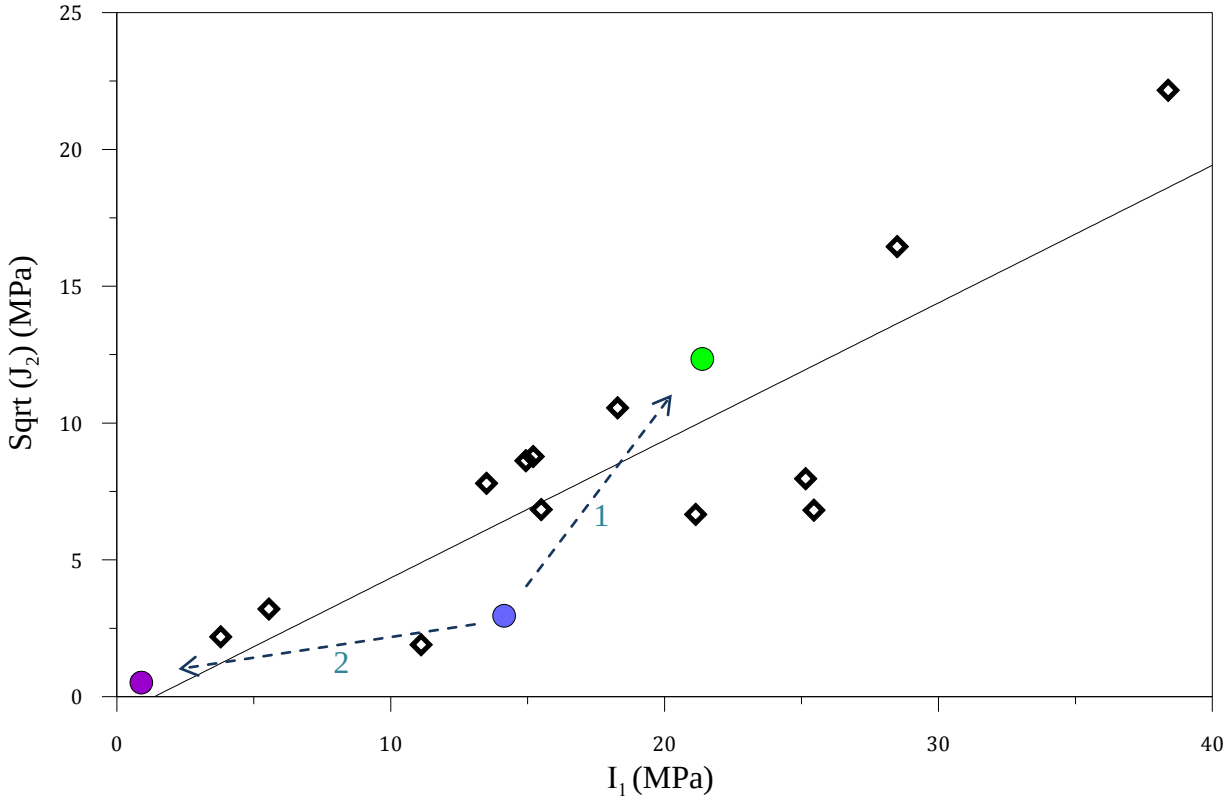

Figure 37: The linear compression-dilation boundary for this study; blue dot is the initial state of stresses, green dot and purple dot are the stresses at the center of the side wall (θ=0°) and the center of the roof (θ=90°) of a horizontal tunnel, respectively.

Chapter 6- Petrophysical behavior: discussion

First, we shall make several definitions. In the raw state of the oil shale the phases that constitute a dry sample are the rock mineralogical matrix, the total organic matter (TOM), mainly kerogen and minor percentage of bitumen, that accumulates contemporaneously with the mineralogic mass and form together the solid phase of the rock and the fluid containing pores. For convenience, we relate to the organic matter as 'kerogen' and neglect the bitumen phase. We define the relative volume of fluid containing pores with respect to the total volume of the sample as fluid porosity ϕ_f , or the measured porosity, and the relative volume of kerogen as kerogen porosity ϕ_k , as illustrated in Figure 38. After pyrolysis the phases constituting the sample are the rock matrix which is assumed here to be the same as in the raw state, the remaining organic matter and the fluid porosity which is expected to increase. The kerogen consists of several elements including carbon, hydrogen, nitrogen, oxygen and sulfur. Therefore, to calculate the kerogen volume relative to the total volume (kerogen porosity) we use the portions of each element measured directly from the kerogen and the known carbon content from the TOC measurements (elemental analysis was performed in Weatherford laboratories, Houston, Texas by IEI Ltd.). The carbon content (TOC) divided by its portion will give the kerogen content (TOM). For the raw oil shale the carbon portion in the kerogen is ~65%, therefore the kerogen weight percentage is TOM (wt%) = 1.54 x TOC (wt%) and for the converted oil shale the carbon portion in the remaining organic matter is ~78%, therefore the TOM (wt%) = 1.28 x TOC (wt%). Finally, to calculate the ϕ_k the TOM is multiplied by the bulk density and divided by the kerogen density, which is assumed to be an average value of 1.03 gr/cm^3.

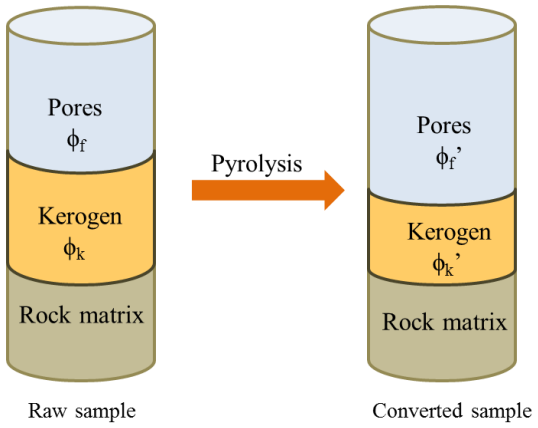

Figure 38: Schematic illustration of the sample's phases before and after thermal conversion.

6.1 Petrophysical properties of the raw Shefela oil shale

Our porosity measurements show relatively high fluid porosity ϕ_f, averaging 37 % at the Ghareb and decreasing with depth most likely due to compaction. A decrease in fluid porosity also appears as the lithology changes in the transition from Ghareb Fm. to Mishash Fm. at ~460 m, averaging 32% at the Mishash (Figure 39). The fluid porosity is relatively independent of kerogen content as can be inferred from Figure 40.

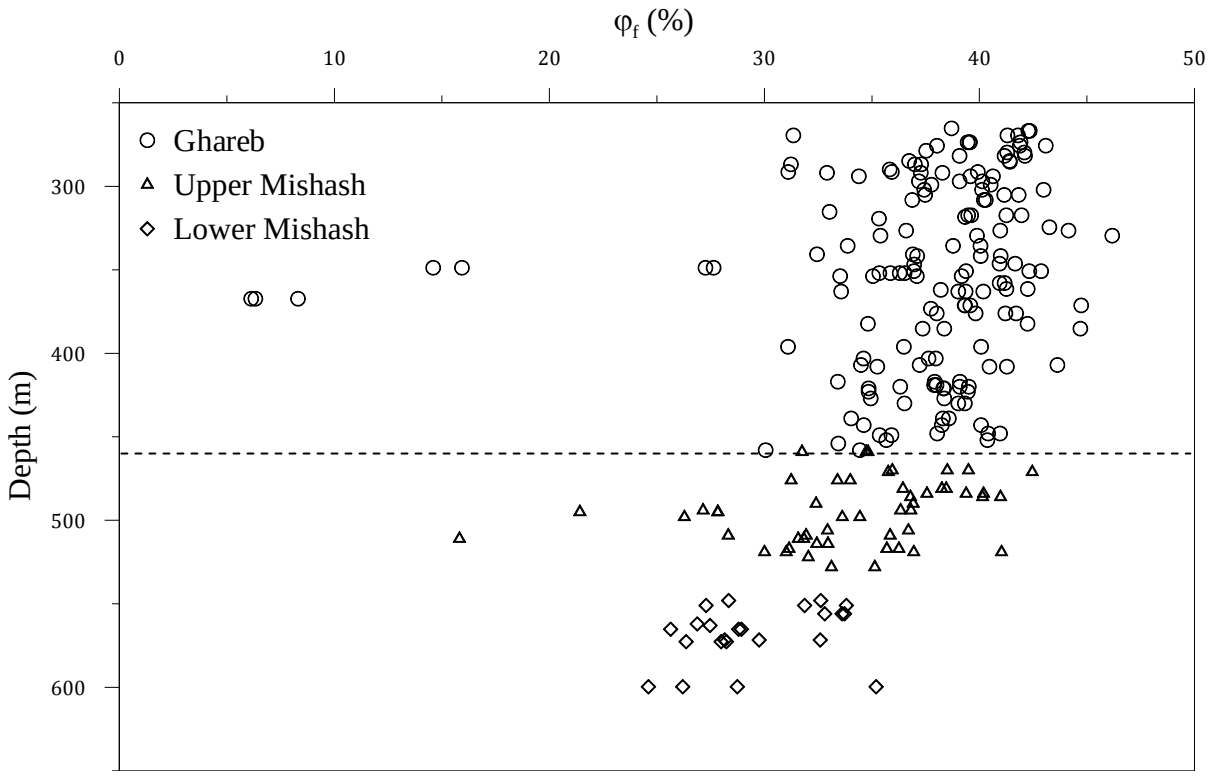

Figure 39: The variation of porosity φ_f with depth; the dashed line represents the boundary between the Ghareb and the Mishash Formations.

The Klinkenberg-corrected gas permeability k_∞ is very low, ranging between 0.001 mD and 1 mD (Figure 41). In the Ghareb the average value of k_∞ is 0.15 mD for parallel to bedding flow and 0.03 mD for normal to bedding flow. In the Mishash the k_∞ decreases to an average value of 0.09 mD for parallel to bedding flow and an average value of 0.02 mD for normal to bedding flow.

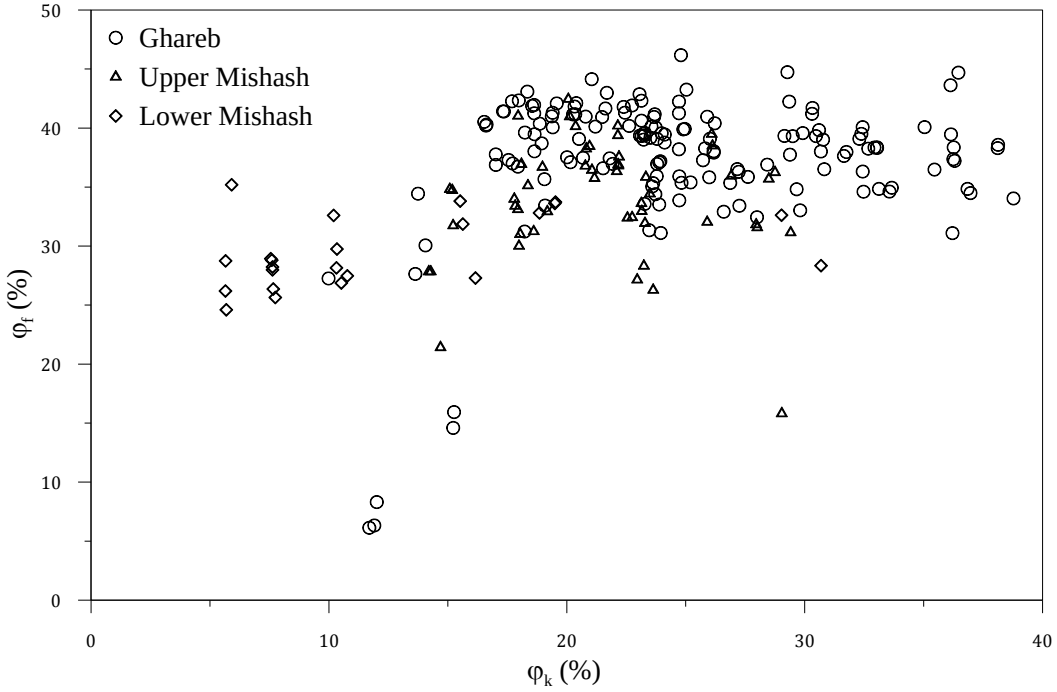

Figure 40: The variation of porosity φ_f with kerogen content (kerogen porosity φ_k).

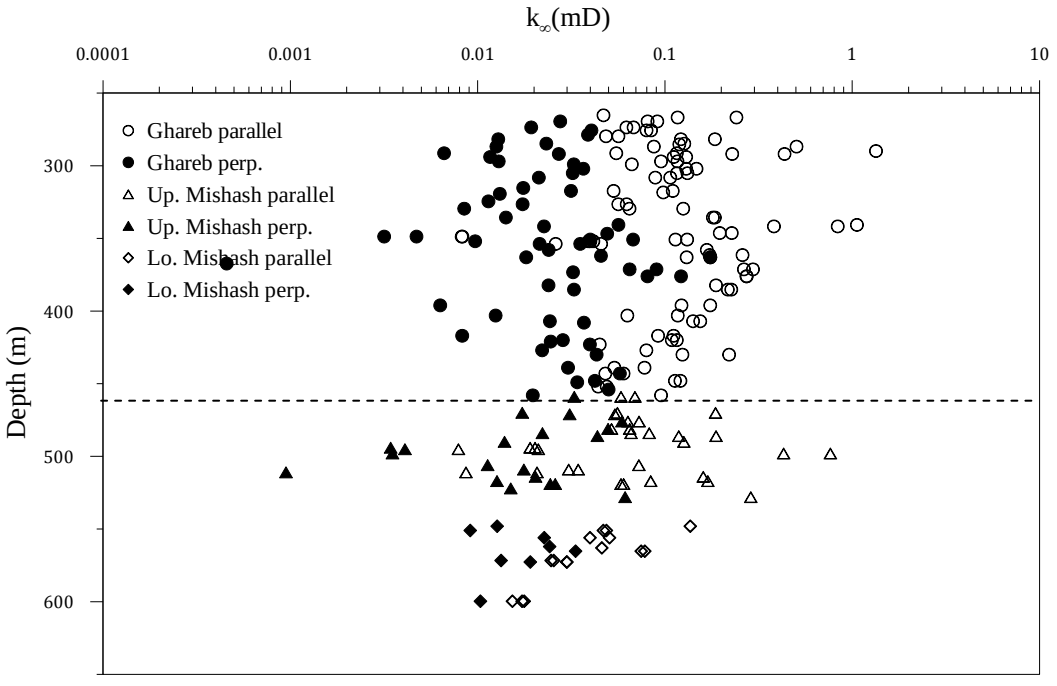

Figure 41: The variation of Klinkenberg-corrected gas permeability k_∞ with depth; the dashed line represents the boundary between the Ghareb and the Mishash Formations.

As would be intuitively expected the Klinkenberg-corrected gas permeability k_∞ when tested parallel to bedding is higher than when tested normal to bedding flow. Our results indicate that the k_∞ for parallel to bedding flow is higher by 5 times on average all along the Aderet

borehole (Figure 42). When examining each lithology separately, the k_∞ for parallel to bedding direction flow is higher by 6.6 on average for the bituminous chalk of the Ghareb formation, by 5.1 on average for the bituminous chalk of the upper Mishash formation and by 3.4 on average for the somewhat silicified (Burg et al., 2010) lower Mishash formation.

The relationship between Klinkenberg-corrected gas permeability k_∞ and fluid porosity ϕ_f is plotted in Figure 43. In Figure 44 these relationships are plotted separately for each stratigraphic segment, indicating a positive relationship between these two variables in both parallel and perpendicular to bedding directions. An exception to this behavior can be noticed in the 'lower Mishash perpendicular to bedding' trend (Figure 44c), however this may be due to the relatively lower number of data points and thus lower resolution; more tests should be made to refine that relationship.

The relative independence of Klinkenberg-corrected gas permeability k_∞ of kerogen content that can be seen in Figure 45 and the relationship between Klinkenberg-corrected gas permeability k_∞ and fluid porosity ϕ_f (Figures 43, 44) suggest that pore structure is the dominant factor influencing the permeability, and not the kerogen content.

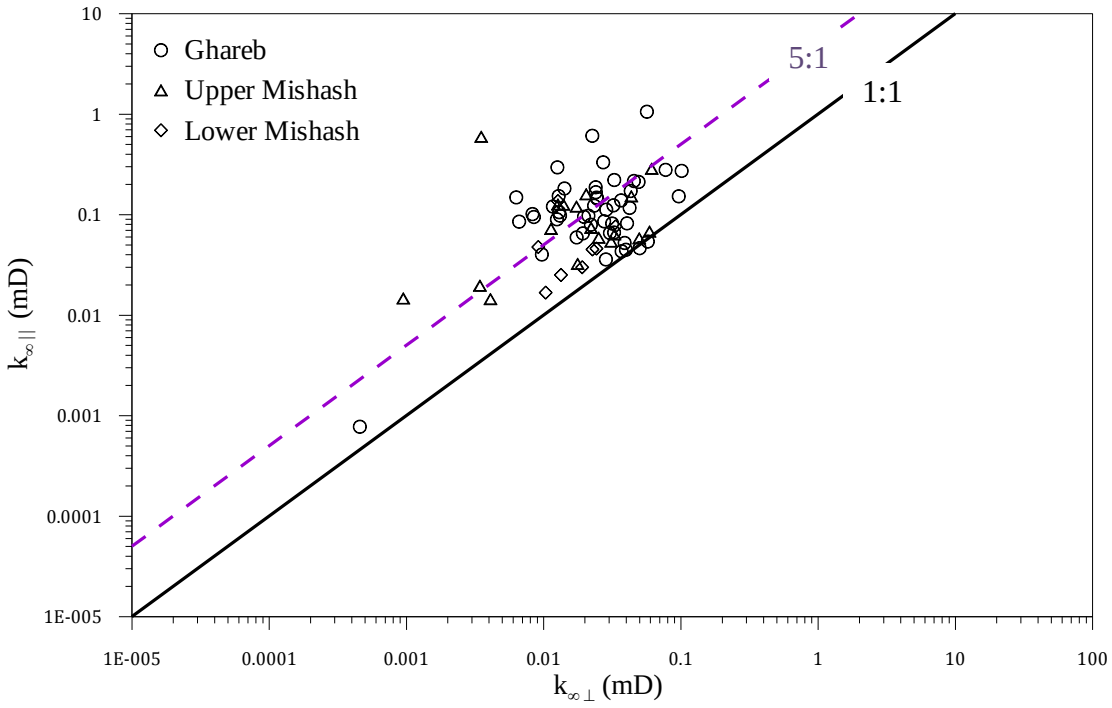

Figure 42: Bedding parallel Klinkenberg-corrected gas permeability $k_{\infty\,II}$ against bedding normal Klinkenberg-corrected gas permeability $k_{\infty}\perp$; black line represents 1:1 reference and purple dashed line represents 5:1 relation.

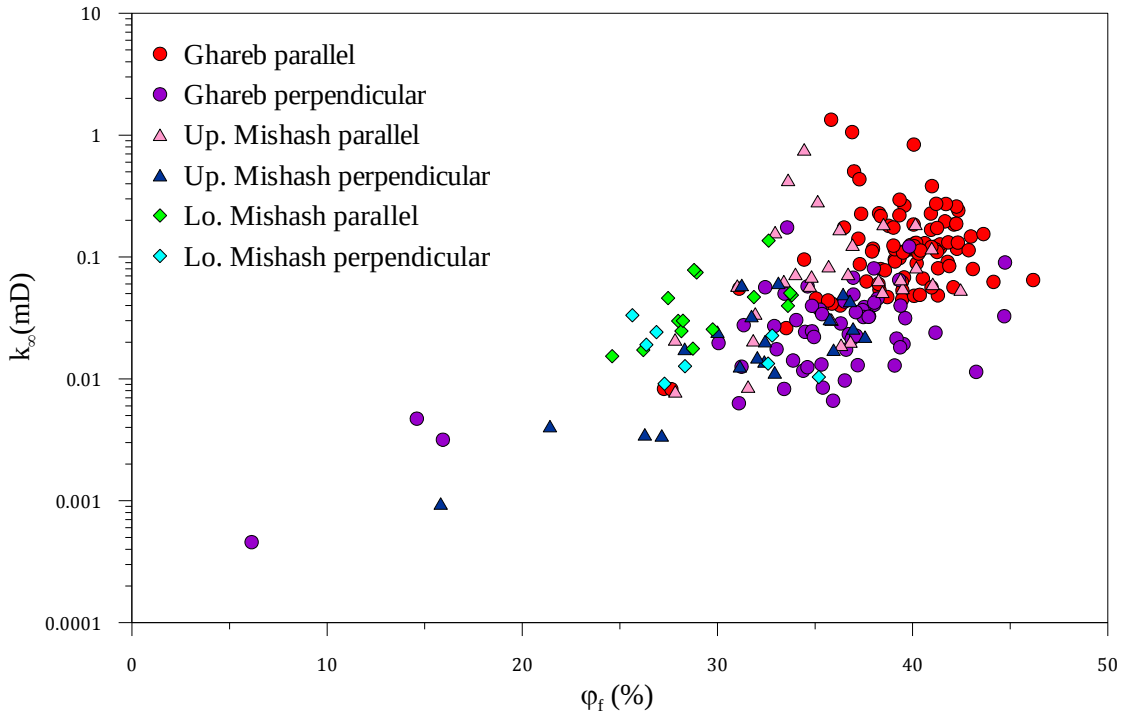

Figure 43: The Klinkenberg-corrected gas permeability k_∞ as a function of fluid porosity φ_f for the whole Aderet borehole.

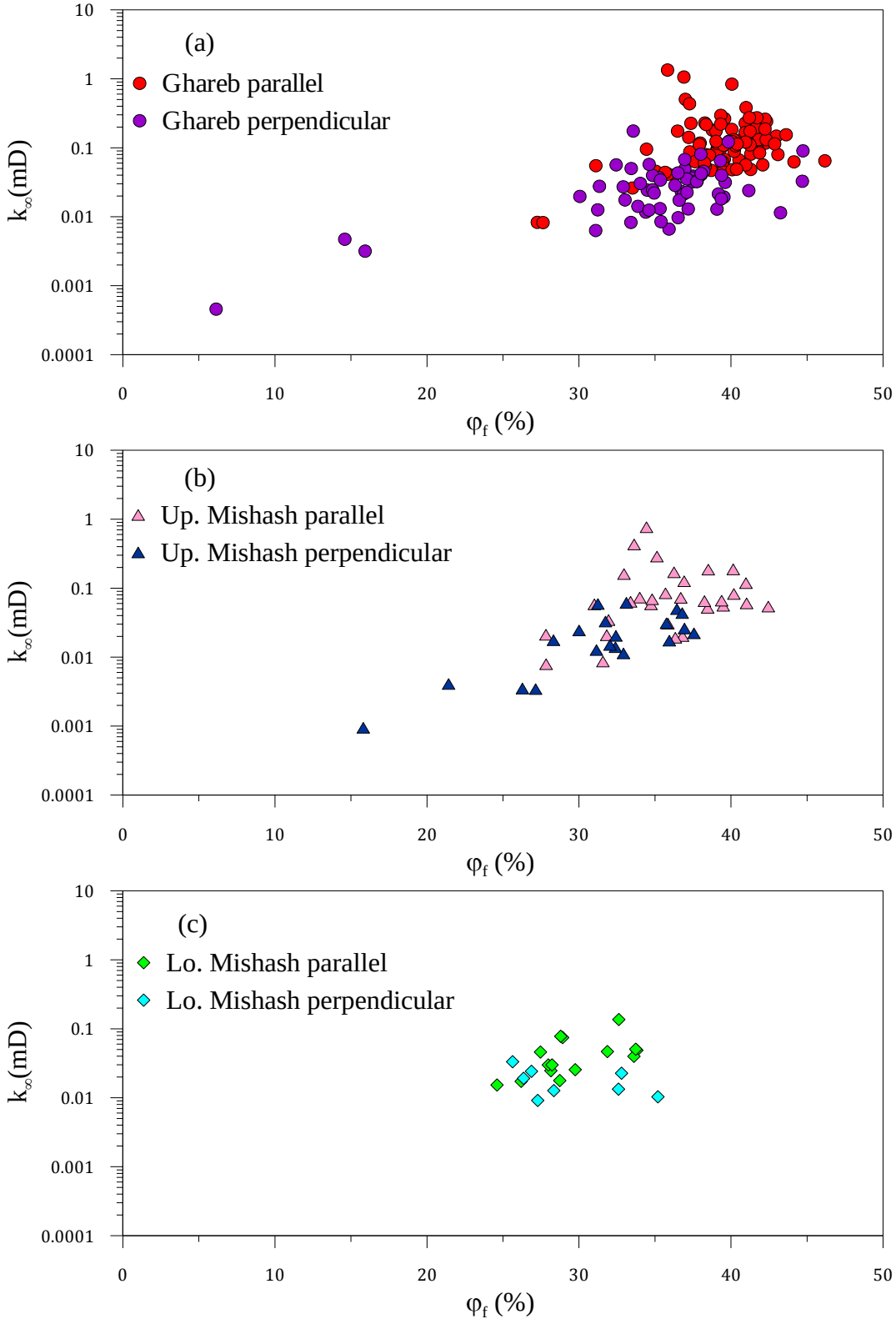

Figure 44: The k_∞- φ_f relationships for: a) Ghareb; b) Upper Mishash; c) Lower Mishash.

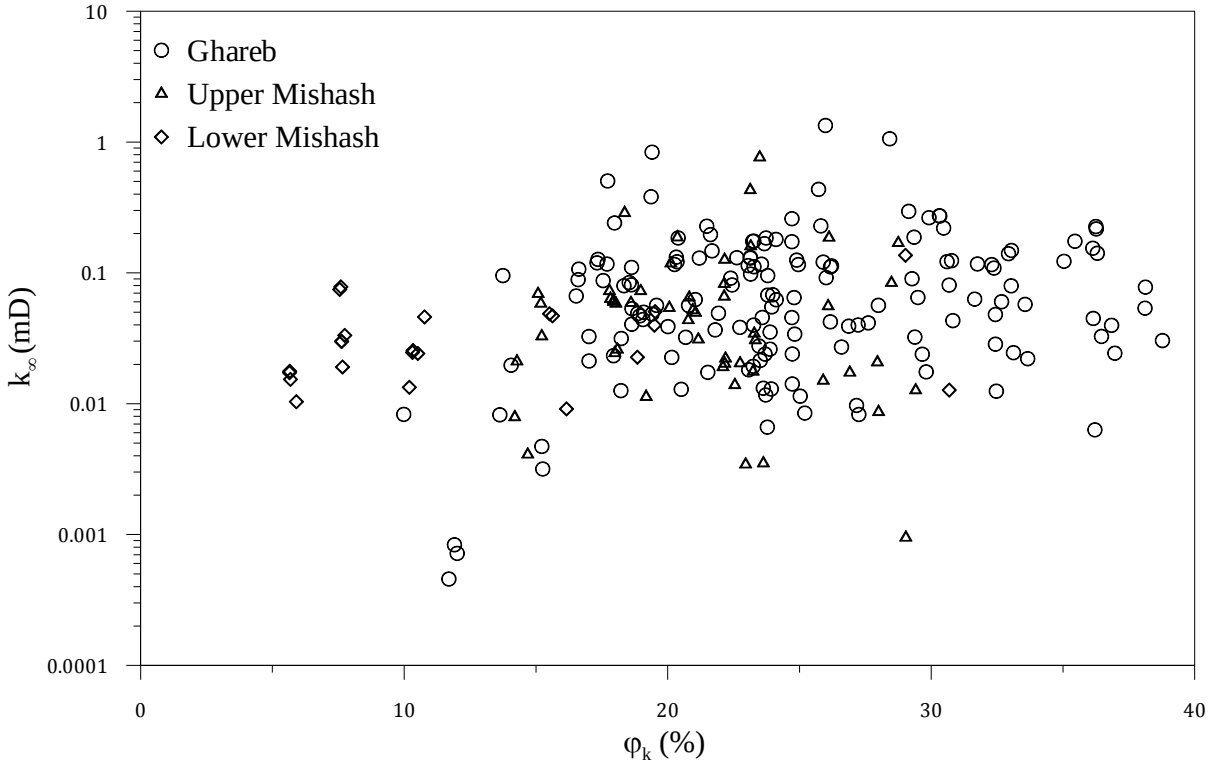

Figure 45: The variation of Klinkenberg-corrected gas permeability k_∞ with organic matter content (kerogen porosity φ_k).

6.2 Effect of thermal conversion of kerogen on the petrophysical properties

As mentioned in Chapter 4 (section 4.2.2), three retort experiments were performed on three different sets of samples. Each set was uniformly heated at a constant heating rate to a goal temperature of 430°C until full conversion (complete cessation of gas release from the samples) was attained. The first pyrolysis was performed with no back pressure applied and with a constant rise of 5°C per hour. In the second pyrolysis a back pressure of 150 psig was applied while the heating rate was kept the same, and in the third pyrolysis the heating rate was reduced to 4°C per day with no back pressure applied. We refer to the first and second experiments as "fast heating tests" and to the third experiment as "slow heating test". The conditions of the experiments are summarized in Table 13.

Table 13: Summarized conditions of pyrolysis experiments

Condition	1st pyrolysis	2nd pyrolysis	3rd pyrolysis
Target Temp (°c)	430	430	430
Back Pressure (psi)	14.7	164.7	14.7
Heating Rate (°c/hour)	5	5	0.17

Figure 46 (a-c) summarizes the k_∞- ϕ_f relationship obtained for the samples studied before (thermally immature raw material) and after the three pyrolysis experiments (Table 13). It demonstrate k_∞- ϕ_f relationship in both pre and after pyrolysis in all three experiments, but with a clear difference in magnitude. The fluid porosity of the oil shale rock after pyrolysis increases up to a maximum value of 62% and the Klinkenberg-corrected gas permeability increases up to a maximum value of 6.5 mD (Figure 47). These relationships were not separated to different lithologies as before (Figure 44) due to the fact that each set of samples that underwent thermal conversion experiment consisted of randomly distributed samples along the Aderet borehole. It should also be pointed out that the permeability data is representative mostly of parallel to bedding flow direction because most of the samples that were tested normal to bedding disintegrated after the first Coreval measurement and only the few that survived went through pyrolysis.

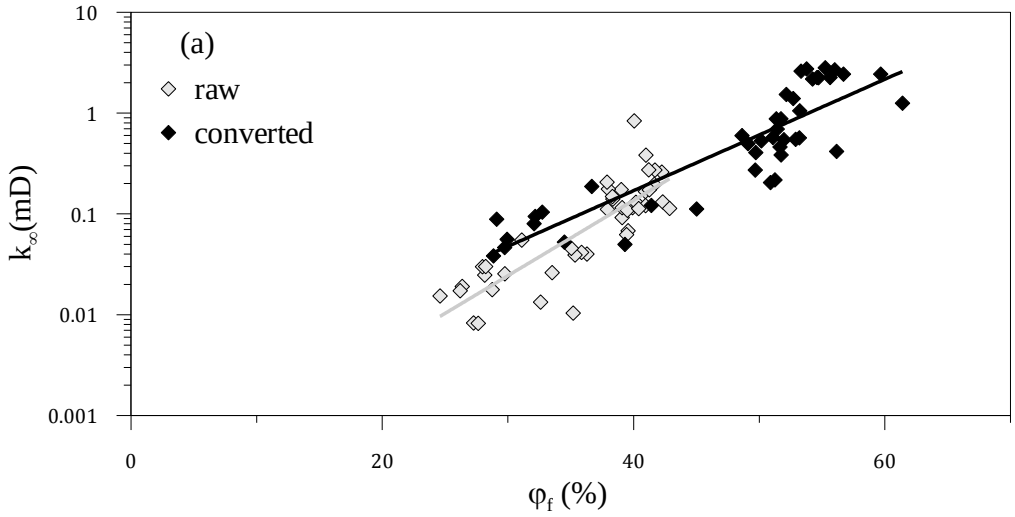

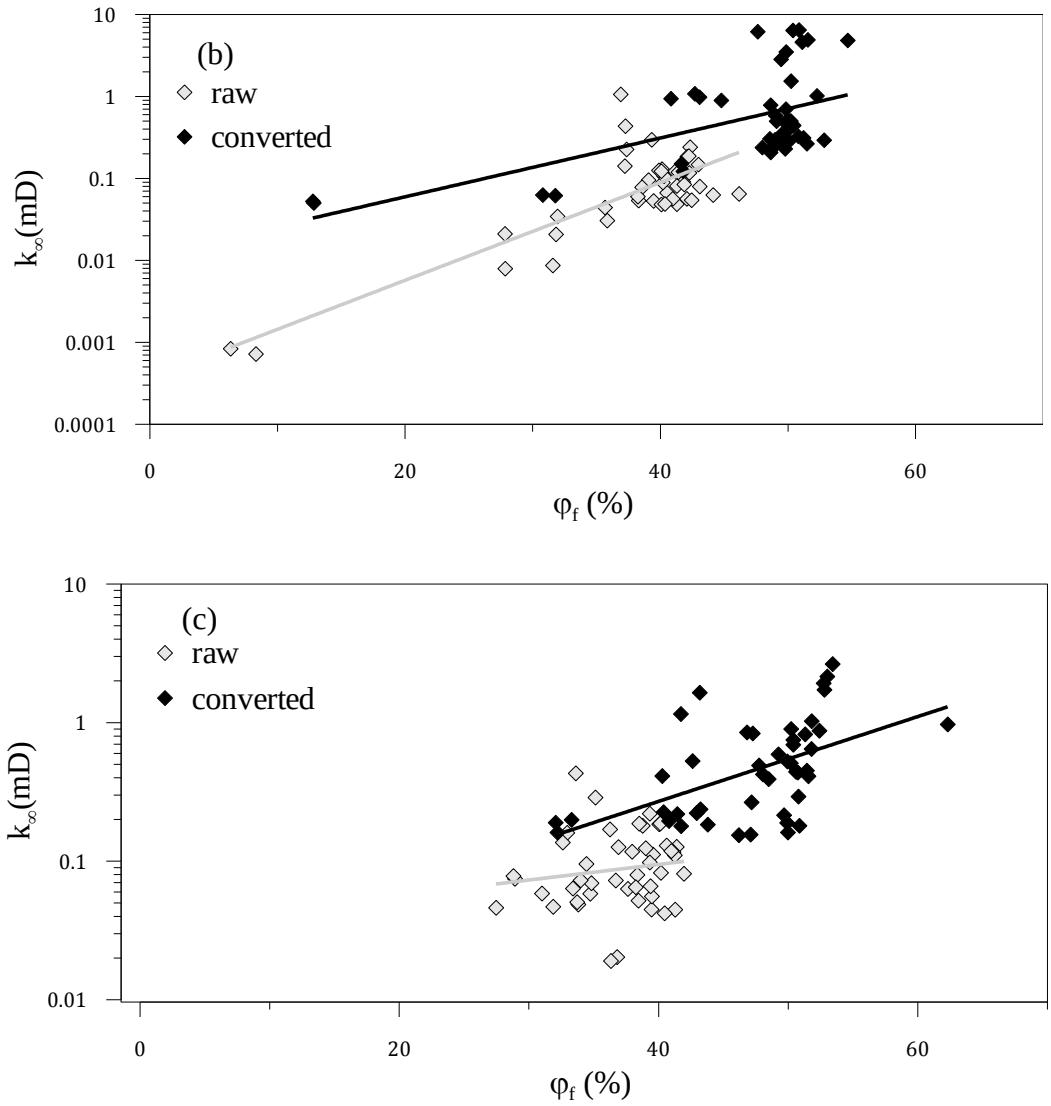

Figure 46: The k_∞- φ_f relationships for: a) 1st; b) 2nd; c) 3rd pyrolysis experiments.

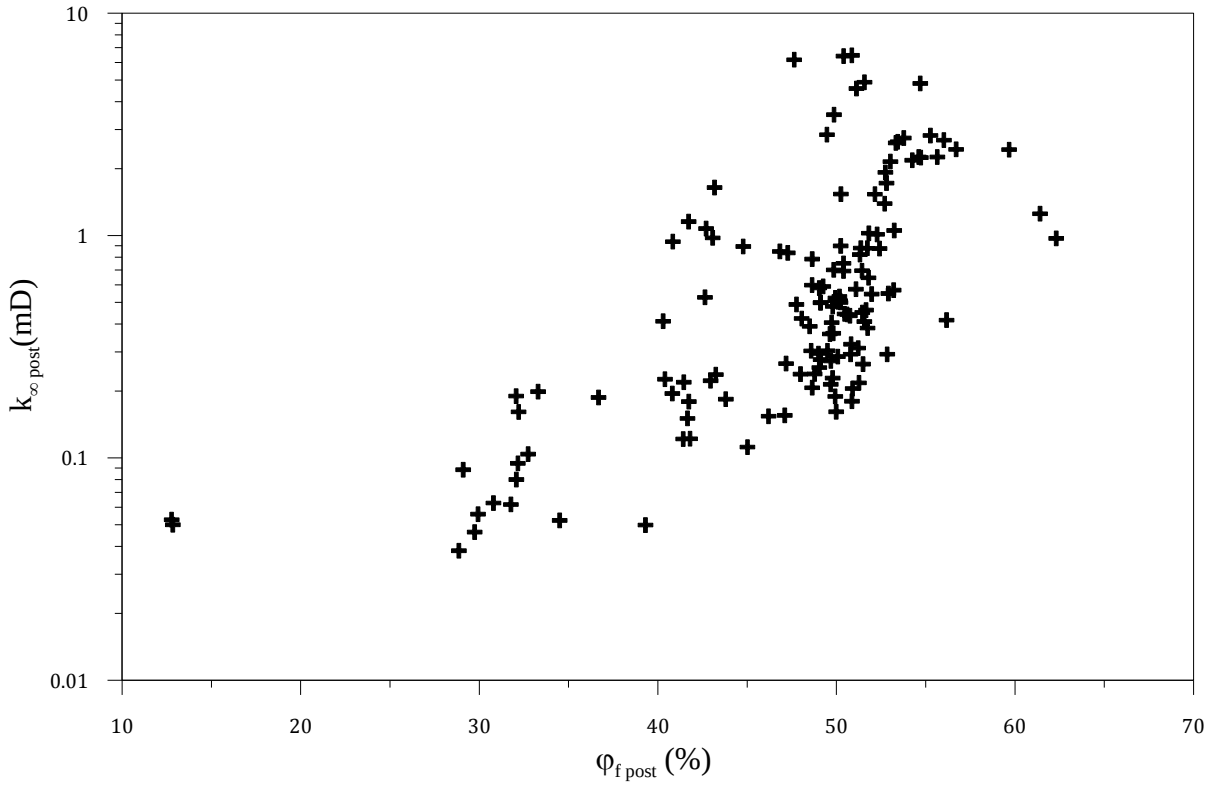

Figure 47: The Klinkenberg-corrected gas permeability after pyrolysis $k_{\infty\ post}$ as a function of fluid porosity after pyrolysis $\varphi_{f\ post}$ for the whole Aderet borehole.

The amount of kerogen loss in the three different pyrolysis experiments is shown in Figure 48. The kerogen volume loss resulted by the pyrolysis is represented by the difference between final and initial kerogen porosity, $\Delta\varphi_k$. The data points represent the difference between final (post-pyrolysis) kerogen porosity and initial (pre-pyrolysis) kerogen porosity against the initial kerogen porosity. The ratio between the data shows high linearity (R square values of 0.87, 0.97 and 0.95), indicating that the amount of kerogen loss in the thermal maturation process depends on the initial kerogen content, as is expected. In the first pyrolysis 55% of initial kerogen content was spent. In the second pyrolysis, back pressure of 150 psig was applied and the kerogen loss percent decreased to 51%. Finally, in the third pyrolysis, when the heating rate was 'slow', 54% of kerogen was spent.

This variation can be explained by visualizing the rock microstructure: it consist of the rock matrix, the kerogen, the pore space and the pore throats. Upon thermal maturation the organic matter releases liquids and gases causing volume reduction. As a result the residual kerogen becomes more solid. Applying back pressure seems to increase the amount of residual kerogen remaining in the rock, also slowing down the rate of temperature increase during the pyrolysis seems to have the same effect but to a much lower extent. This results in a lower percent of kerogen loss in the second pyrolysis experiment's conditions where back pressure of 150 psig was applied.

Next we would like to examine how the fluid porosity, Klinkenberg-corrected gas permeability and slip factor are affected by the decomposition of the kerogen as the rock undergoes pyrolysis. In addition we examine how the pyrolysis conditions (pressure and heating rate) affect these changes. The following charts are therefore presented in terms of pyrolysis number and lithology.

In general, after pyrolysis, the fluid porosity is enhanced by an average factor of ~1.28 with a relatively small variation due to changes in pyrolysis conditions (Figure 49). The ϕ_f is increased by an average factor of 1.3 for the first pyrolysis experiment and by average factors of 1.25 and 1.28 for the second and third experiments respectively. In conclusion, while the kerogen is decomposed and volatiles released during the pyrolysis, new space is being created within the rock due to its volume loss; therefore a porosity increase is measured. Applying back pressure causes an increase in the volume of residual kerogen that line up the pore space and decrease the fluid porosity growth. Decreasing the temperature ramp rate

causes the same effect (as was discussed before), resulting in a lower increase in fluid porosity.

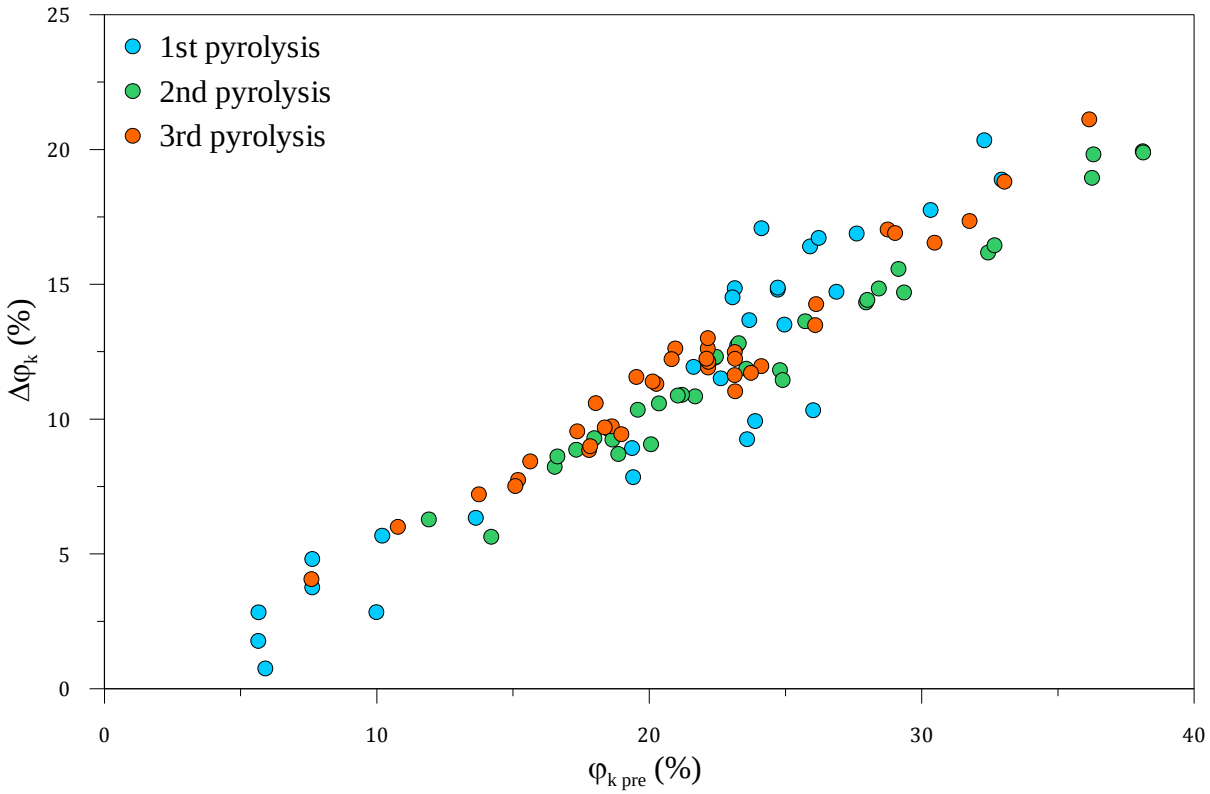

Figure 48: The relationship between the change in kerogen porosity $\Delta\varphi_k$ and the initial kerogen porosity $\varphi_{k\ pre}$; the average kerogen loss for each data set is: 55% for the 1st pyrolysis, 51% for the 2nd pyrolysis and 54% for the 3rd pyrolysis.

The degree of fluid porosity enhancement $\Delta\phi_f$ depends also on the amount of kerogen initially in place $\phi_{k\ pre}$ (see Figure 50). After the first pyrolysis, 55% of kerogen volume "opens up". When applying back pressure of 150 psig in the second pyrolysis 37% of kerogen volume "opens up". Finally, 46% of kerogen volume "opens up" in the third 'slow' pyrolysis. These findings are consistent with the argument that pyrolysis conditions affect the amount of volatile matter that are released from the kerogen and result in its volume decrease.

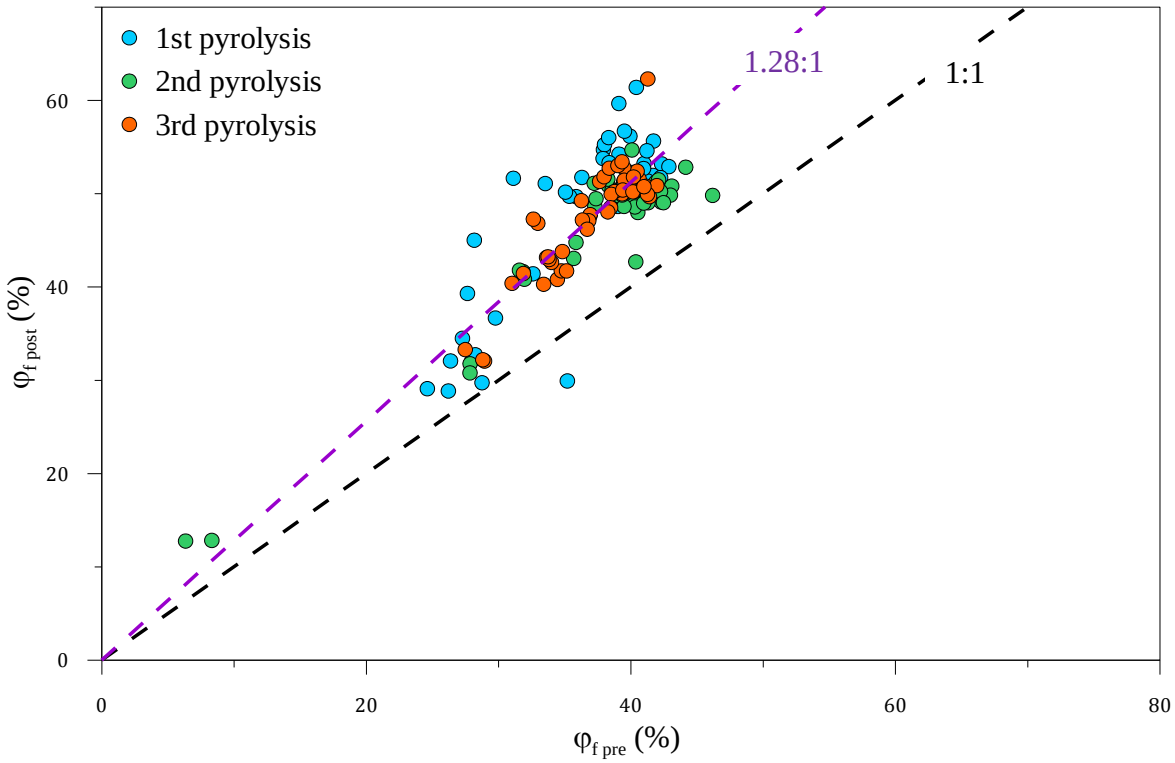

Figure 49: Fluid porosity after pyrolysis $\varphi_{f\,post}$ against fluid porosity before pyrolysis $\varphi_{f\,pre}$ for the three experiments; black dashed line represents 1:1 reference and purple dashed line represents 1.28:1 relation.

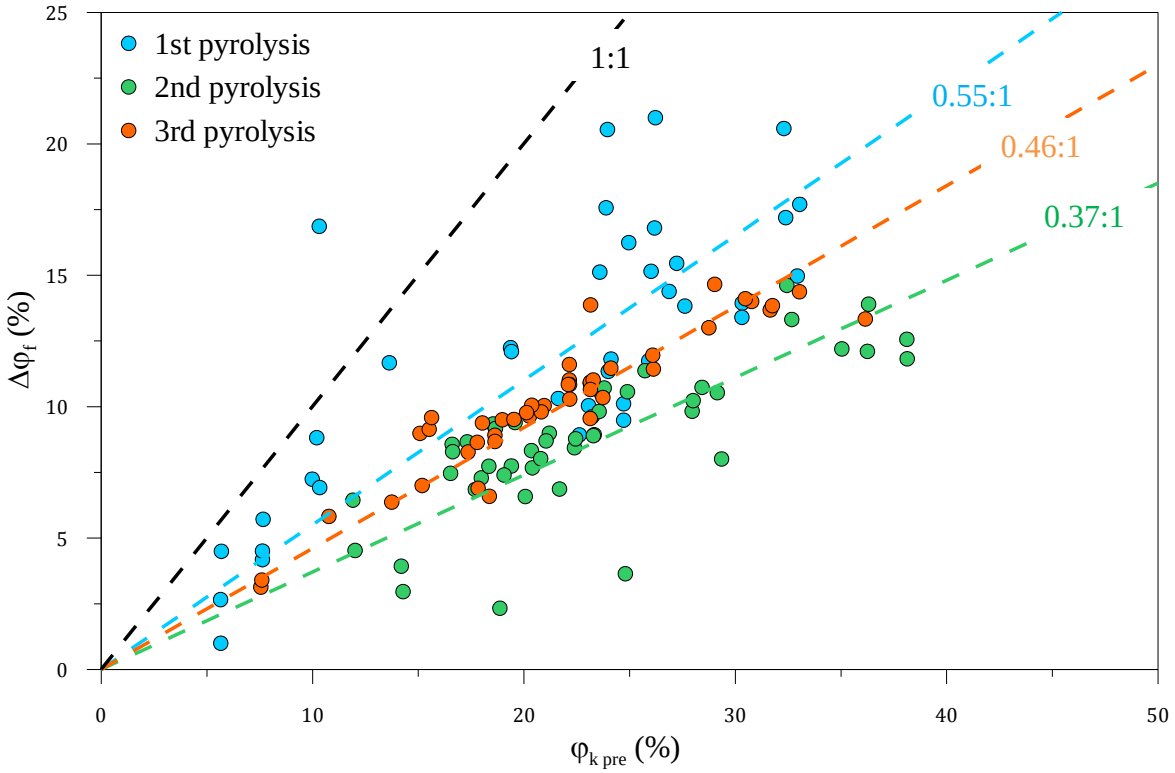

Figure 50: The relationship between the change in fluid porosity $\Delta\varphi_f$ and the initial kerogen porosity $\varphi_{k\,pre}$ for each experiment; black dashed line represents 1:1 reference, blue dashed line represents 0.55:1 relation, green dashed line represents 0.37:1 relation and orange dashed line represents 0.46:1 relation.

The Klinkenberg-corrected gas permeability k_∞ is significantly increased after thermal conversion. (Figure 51). The degree of increase has a relatively small variation with the pyrolysis conditions. The k_∞ is increased by an average factor of 8.5 for the first pyrolysis and by average factors of 10.4 and 7.2 for the second and third experiments respectively. The degree of $k_{\infty\ post}$ and the k_∞ enhancement are strongly related to the amount of kerogen initially in place (see Figure 52a and Figure 52b). Therefore, for rocks where these relations are established, the Klinkenberg-corrected gas permeability after pyrolysis $k_{\infty\ post}$ can be estimated if the initial kerogen porosity $\phi_{k\ pre}$ in the oil shale is known.

Figure 52 reveals that even though the amount of residual kerogen left behind is different between the different pyrolysis conditions, the k_∞ enhancement follows the same relationship.

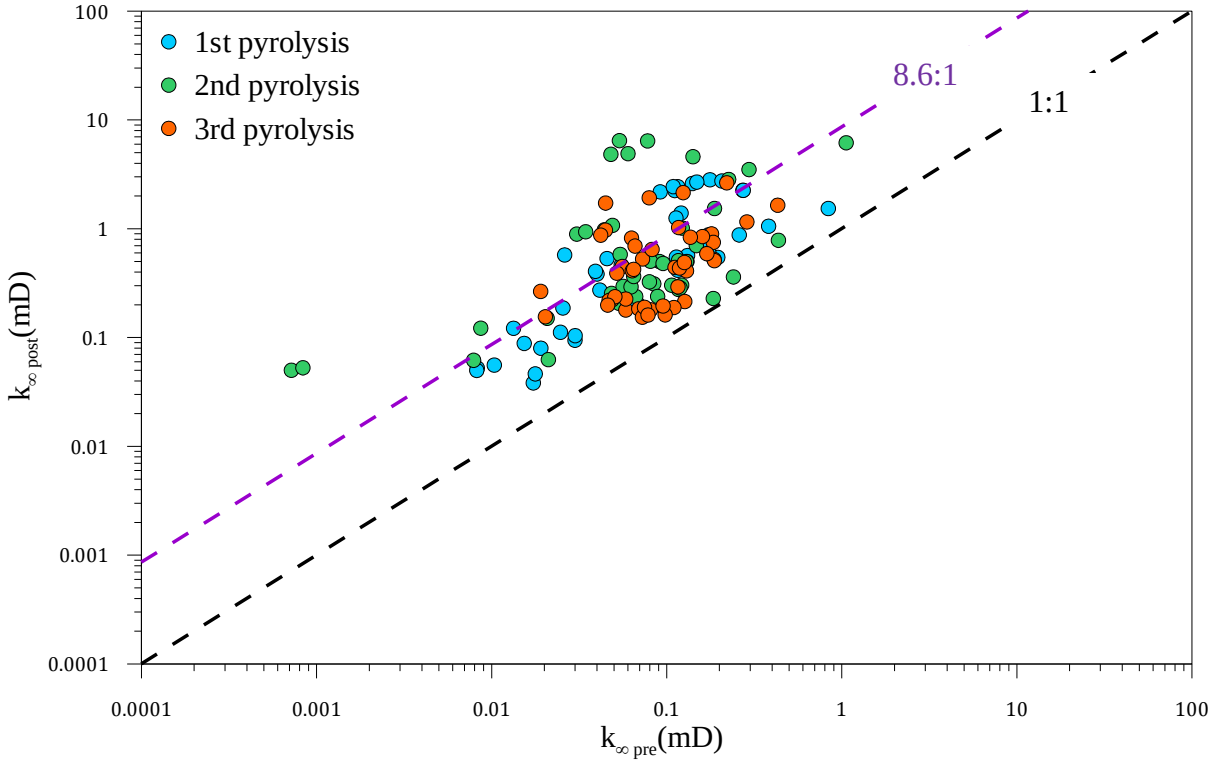

Figure 51: Klinkenberg-corrected gas permeability after pyrolysis $k_{\infty\ post}$ against Klinkenberg-cocrrected gas permeability before pyrolysis $k_{\infty\ pre}$ for each experiment; black dashed line represents 1:1 reference and purple dashed line represents 8.6:1 relation.

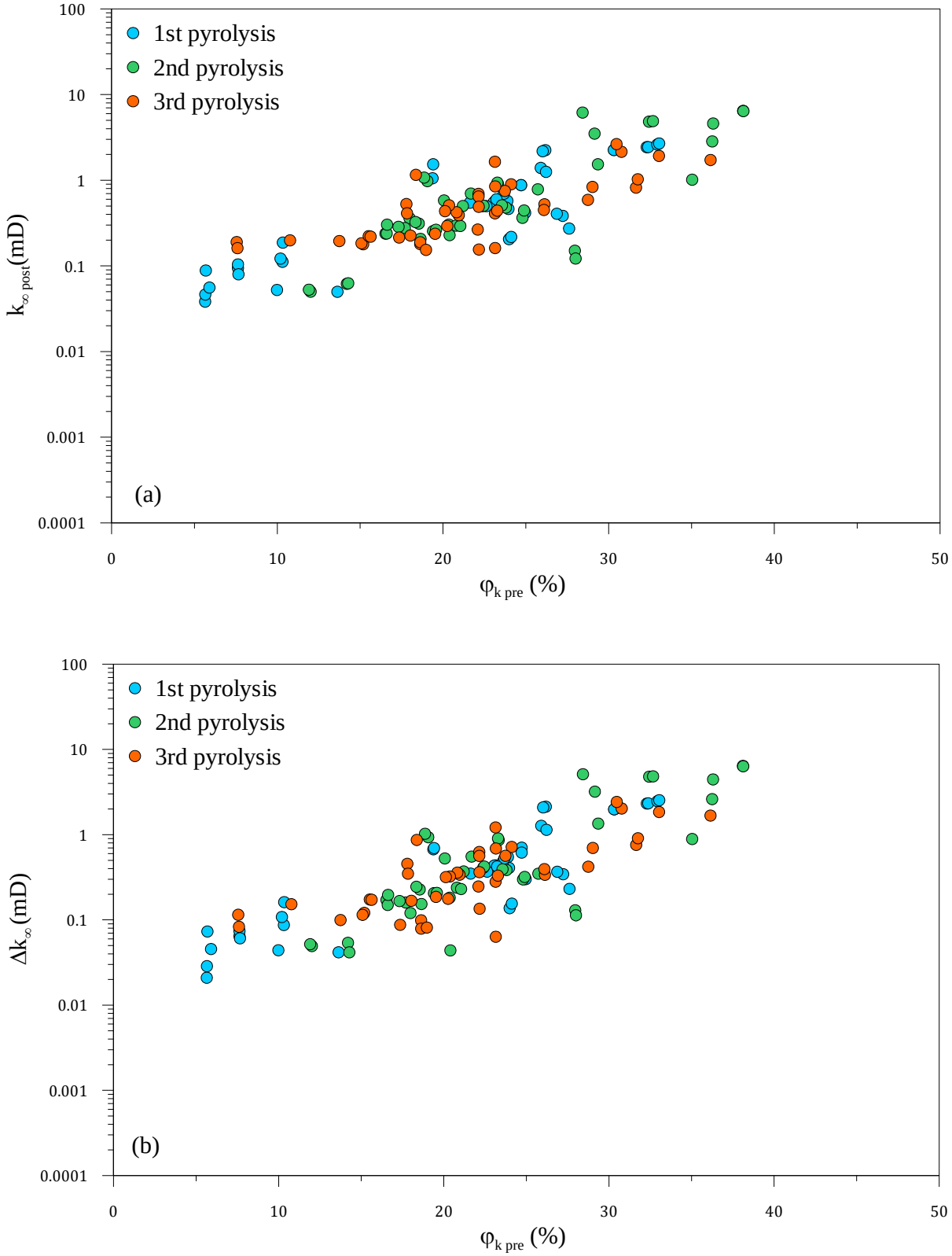

Figure 52: The relationship between: (a) the Klinkenberg-corrected gas permeability post pyrolysis k_{∞} and the initial kerogen porosity $\varphi_{k\ pre}$ for the three experiments; (b) the change in Klinkenberg-corrected gas permeability Δk_{∞} and the initial kerogen porosity $\varphi_{k\ pre}$ for the three experiments.

When applying Klinkenberg's relationship (equation 18, Chapter 3) to our porous medium of the low permeable bituminous chalk, it follows that the slip factor, that is inversely proportional to the radius of capillaries (pore throats), may be expected to be relatively large. Our results confirm this behavior and indicate that the slip factor is inversely related to the Klinkenberg-corrected gas permeability in the raw state of the rock (Figure 53). After thermal conversion the slip factor relationship with Klinkenberg-corrected gas permeability increases (Figure 54). Since the slip factor is related to the Klinkenberg-corrected gas permeability and to the mean pore throat radius, we compare graphically the change in the slip factor for the same permeability, this way the change in the slip factor after pyrolysis describes the pore throat radius change.

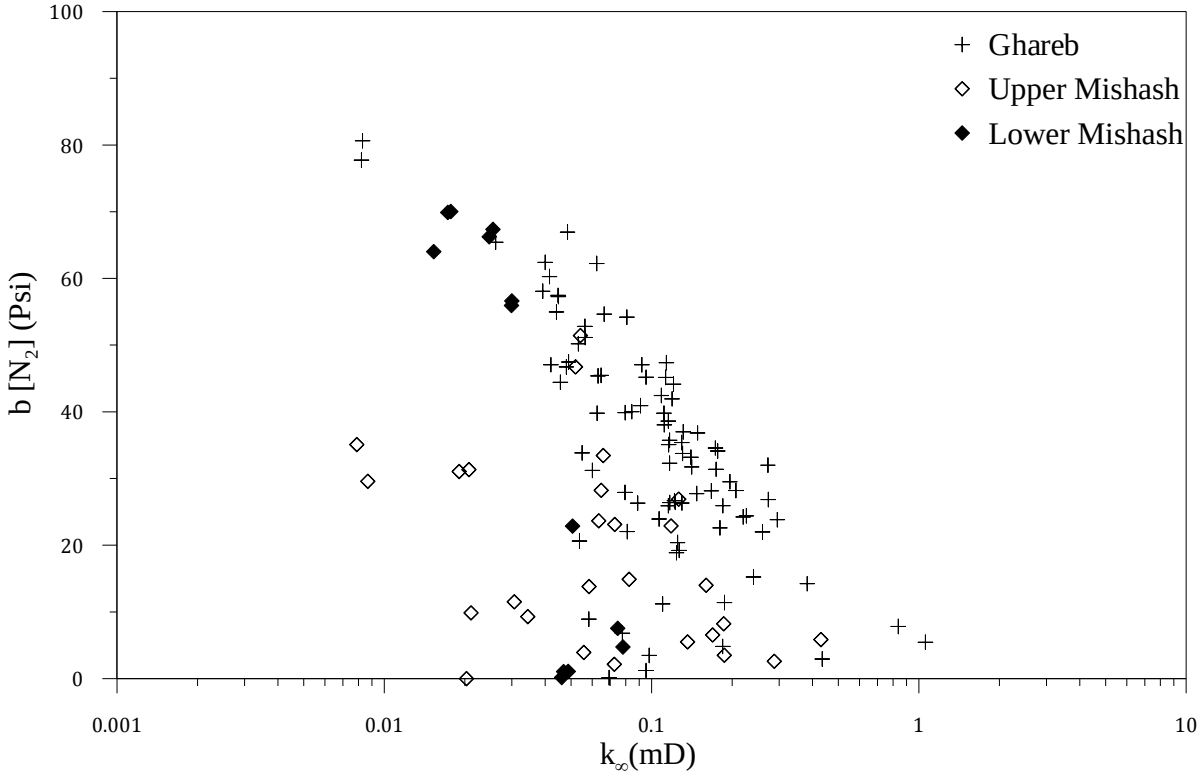

Figure 53: The relationship between slip factor b and Klinkenberg-corrected gas permeability k_∞ for Ghareb and upper Mishash and lower Mishash Formations.

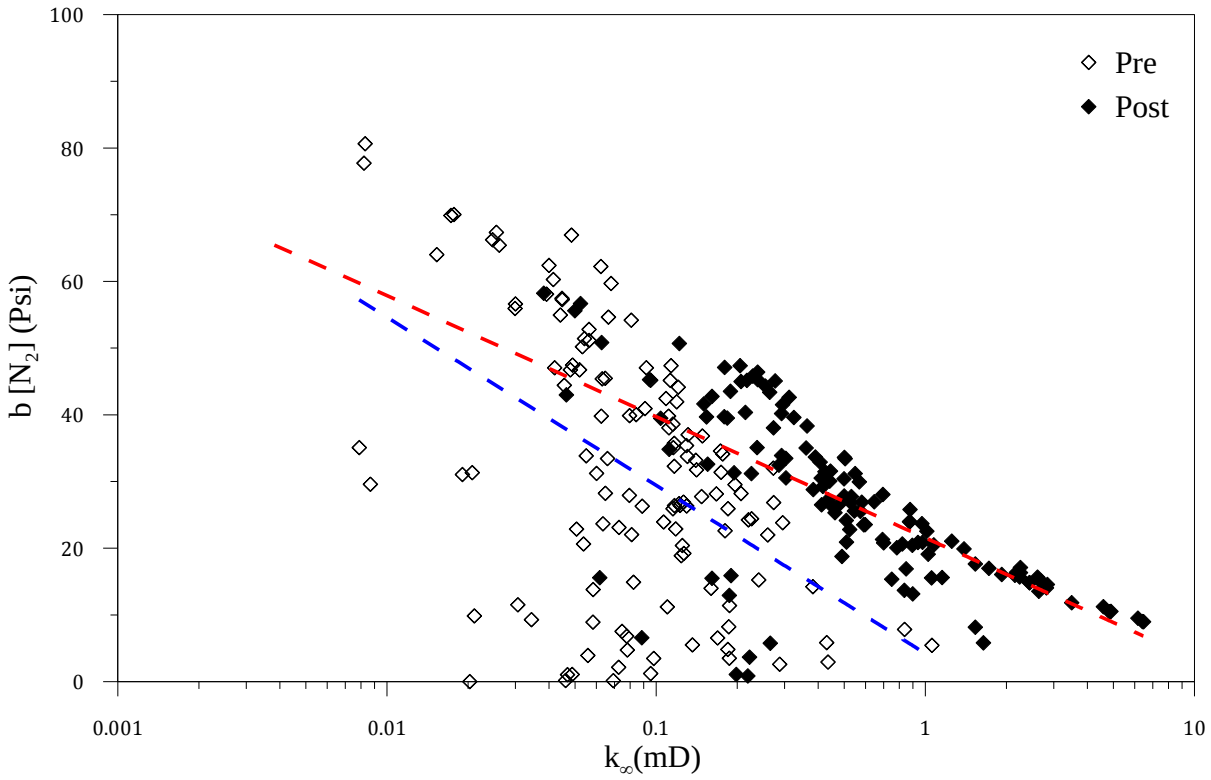

Figure 54: The relationship between slip factor b and Klinkenberg-corrected gas permeability k_∞ before and after pyrolysis tests; blue and red dashed lines represent a rough trend for the before and after the tests, respectively.

As can be noticed in Figure 54 for the same permeability the slip factor is higher after thermal conversion. This indicates that the mean pore throat radius decreased. In the lower permeability range the data seems to converge, indicating that in initially very low pore throats the change is less significant. Examination of each lithology separately in Figure 55 shows that in Ghareb this trend is clear over a wide range of permeability, whereas in the upper and lower Mishash the range of permeability is smaller and the trends seem less apparent.

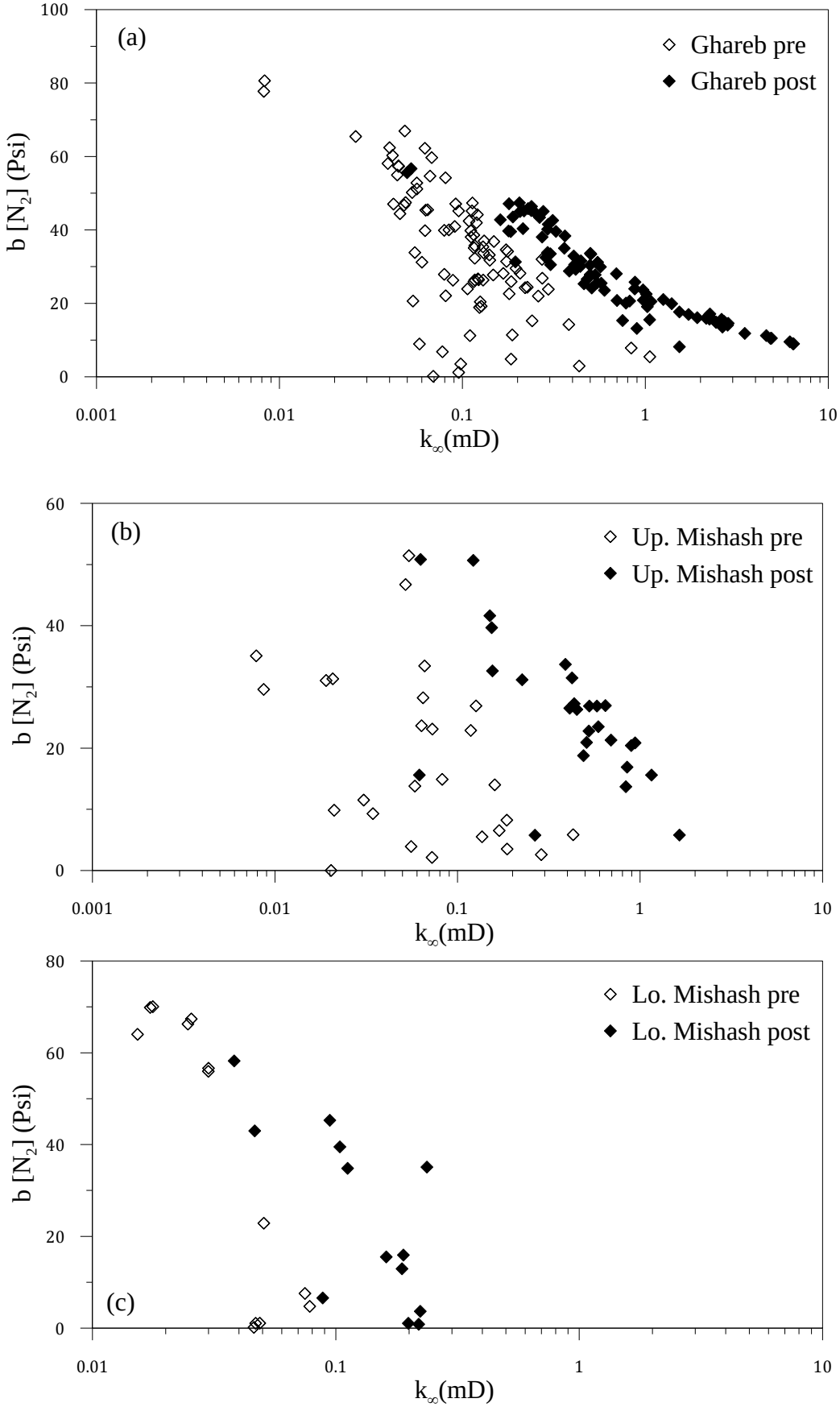

Figure 55: The relationship between slip factor b and Klinkenberg-corrected gas permeability k_∞ before and after pyrolysis experiments for separate lithologies: a) Ghareb; b) Upper Mishash; c) Lower Mishash.

Chapter 7- Summary and Conclusions

The purpose of this research was to characterize the mechanical and petrophysical behavior of the oil shale from the Shefela basin in Israel. The Shefela oil shale is mainly a bituminous chalk which was deposited in marine environment. Knowledge of the mechanical and petrophysical properties of the Shefela oil shale is required for production planning and management and for evaluation of environmental implications. These characteristics are of great importance to the understanding of natural thermal maturation and migration processes from source rocks.

A comprehensive testing program was conducted on core samples extracted from the Aderet borehole located within the Shefela deposit. The lithological section of Aderet is divided to the dark bituminous chalk of the Ghareb formation in transition to the upper Mishash formation which is litholigically similar to the Ghareb formation and below it the brighter less bituminous and somewhat silicified chalk (Burg et al., 2010) of the lower Mishash formation. The interval richest in organic matter is in the middle of the Aderet section (350-450 m) where the TOC values average 15% and decrease upwards and downwards.

For the mechanical characterization unconfined, triaxial and hydrostatic compression tests as well as Brazilian tensile strength tests were performed. At room temperature, the bituminous chalk exhibits a brittle behavior, the failure of which can be described by the linear Coulomb-Mohr criterion or more precisely by the Griffith's criterion (up to a maximum principal compressive stress of 19.5 MPa). The cohesion and the angle of internal friction obtained from the linear Coulomb-Mohr criterion are 5.51 MPa and 10.7°, respectively. Large differences can be observed in the mechanical properties between the Ghareb and the lower Mishash Formation. It was found that the static Young's modulus (E) increases with depth from ~ 1 GPa at 290 m to up to ~ 3 GPa at the bottom of the Ghareb Formation at 460 m, reaching higher values of up to 9.2 GPa at the underlying Mishash Formation. The Uniaxial compressive strength shows a similar trend, averaging 19 MPa at the tested interval in the Ghareb Formation and of 53.8 MPa at the Mishash Formation. The static bulk modulus (K) of the tested rock sample showed growth through different stages of the applied hydrostatic compression up to a maximum value of P_c= 30 MPa: the first stage indicated the closure of micro-crack with K=1.47 GPa. In the second stage a higher density caused by the first compaction with K=3.3 GPa and finally, the highest bulk modulus of K= 4.8 GPa indicated initiation of irreversible compaction but not yet pore collapse. Generally, the tensile strength

of the Shefela bituminous chalk decreases with increasing water content. Yet, the rate of change in tensile strength seems to decrease with increasing water content. Our results indicate that this behavior is mostly apparent in Mishash silicified and less bituminous chalks while the tensile strength of the Ghareb formation seems less sensitive to changes in water content. A mechanical anisotropy was observed in the entire range of tested water contents, showing that the tensile strength parallel to bedding is higher by 1.7 on average for Ghareb and by 2.2 on average for Mishash compared to normal to bedding. In addition, using the results of the compression tests, an empirical linear compression-dilation (C-D) boundary was defined for the Shefela bituminous chalk. This boundary can be applied to analyze the volumetric behavior of the rock in case of drilling vertical shafts or horizontal boreholes for heating elements and production process. We have showed that at a specific chosen depth, borehole diameter and specified orientations, the deformation of the rock transfers from compressional to dilational behavior- a process that could prompt permeability increase in the rock mass immediately surrounding the newly created underground space. Additional triaxail compression tests should be made to refine the compression-dilation boundary.

For the petrophysical characterization properties such as porosity, permeability, Klinkenberg slip factor and total organic carbon (TOC) were measured before and after three different thermal maturation (pyrolysis) experiments. It was found that in the raw state (before pyrolysis) the porosity is relatively high averaging ~ 37 % at the Ghareb and decreasing with depth most likely due to compaction and the transition to the somewhat silicified Mishash formation. The Klinkenberg-corrected gas permeability is very low ranging between 0.001 mD and 1 mD. Notably, the Klinkenberg-corrected gas permeability normal to bedding is lower than that parallel to bedding by an average factor of 5, implying that vertical flow is more restricted relative to horizontal flow along the bedding plane. The porosity and Klinkenberg-corrected gas permeability are found to be relatively independent of the organic matter content. We have also shown that porosity is the dominant factor influencing the Klinkenberg-corrected gas permeability before pyrolysis.

Upon thermal maturation the organic matter releases liquids and gases causing volume reduction. New space is being created within the rock and the porosity is enhanced by an average factor of ~1.28 up to a maximum value of 62% with relatively small variation due to changes in pyrolysis conditions. The Klinkenberg-corrected gas permeability is significantly enhanced by almost an order of a magnitude on average and up to a maximum value of 6.5 mD. The amount of organic matter loss depends on the initial organic matter content and on

the pyrolysis conditions. Applying back pressure seems to increase the amount of residual kerogen remaining in the rock and decrease the fluid porosity growth. Slowing down the rate of temperature increase during the pyrolysis seems to have the same effect but to a much lower extent. Maximum kerogen volume reduction of 55% was measured under pyrolysis with no back pressure, and minimum kerogen volume reduction of 37% was measured in the pyrolysis where back pressure of 150 psig was applied. The degree of fluid porosity enhancement and the degree of Klinkenberg-corrected gas permeability enhancement are strongly related to the amount of kerogen initially in place. The porosity enhancement depends also on the pyrolysis conditions as stated before, whereas the Klinkenberg-corrected gas permeability enhancement is independent of pyrolysis conditions and can be estimated if the initial kerogen content in the Shefela oil shale is known. Our results indicate that the slip factor is inversely related to the Klinkenberg-corrected gas permeability in the Shefela bituminous chalk, as expected. Since the slip factor is also related to the mean pore throat radius of the rock, graphical comparison of the change in the slip factor for the same permeability showed that the mean pore throat radius is decreased due to increase of permeability by pyrolysis. This trend is mostly apparent in the Ghareb formation over a wide range of permeabilities.

These results are of a high importance for the evaluation of the Shefela bituminous chalk as a potential resource of energy and can be specifically utilized for *in-situ* production planning and modeling. Future mechanical investigations should focus on refining the failure criterion and the compression-dilation boundary by performing more triaxail compression tests. In addition, investigation of the mechanical properties after pyrolysis is of a great interest for the understanding of the mechanical behavior during thermal maturation of the rock and for safe and efficient production planning. The investigation of the evolution of petrophysical properties should be detailed to discrete steps during the pyrolysis process to refine the understanding of the organic matter mobilization. It should be pointed out that the permeability data after pyrolysis is representative mostly of parallel to bedding flow direction and should be investigated for normal to bedding flow direction as well.

References

Almogi-Labin, A., Bein, A., and Sass, E., 1993, Late Cretaceous Upwelling System Along the Southern Tethys Margin (Israel) - Interrelationship between Productivity, Bottom Water Environments, and Organic-Matter Preservation: Paleoceanography, v. 8, no. 5, p. 671-690.

Altun, N. E., Hiçyilmaz, C., Hwang, J. Y., Suat Bağci, A., and Kök, M. V., 2006, Oil Shales in the world and Turkey; reserves, current situation and future prospects: a review: Oil Shale. A Scientific-Technical Journal, v. 23, no. 3, p. 211–227.

American Petroleum Institute, E. a. P. D., 1998, Recommended Practices for Core Analysis RECOMMENDED PRACTICE 40.

Brady, B., and Brown, E., 2004, Rock Mechanics for Underground Mining, Kluwer Academic Publishers, London.

Burg, A., Bartov, Y., Grosman, R., and Dror, Y., 2010, Survey of the Shfela't Yehuda Oil shale. Examination drillings at Nahal Guvrin and Aderet, drilling process and geological and hydrological preliminary conclusions.: IEI, IEI/1/2010.

Coulomb, C. A., 1776, Essai sur une application des règles de maximis & minimis à quelques problèmes de statique, relatifs à l'architecture, De l'Imprimerie Royale.

Critescu, N. D., and Hunsche, U. E., Determination of nonassociated constitutive equation for rock salt from experiments, *in* Proceedings Finite Inelastic Deformation-Theory and Applications, IUTAM Symposium1992, Springer-Verlag, New York, p. 511-523.

Darcy, H., 1856, Les fontaines publiques de la ville de Dijon. Exposition et application des principes à suivre et des formules à employer dans les questions de distribution d'eau: ouvrage terminé par un appendice relatif aux fournitures d'eau de plusieurs villes au filtrage des eaux et à la fabrication des tuyaux de fonte, de plomb, de tole et de bitume, Dalmont.

Dusseault, M. B., and Loftson, M., 1985, The mechanical properties of the Kettle Point oil shale, Ontario: Geological survey open file report 5560.

Dyni, J. R., 2003, Geology and resources of some world oil-shale deposits: Oil Shale, v. 20, no. 3, p. 193-252.

Eseme, E., Krooss, B. M., and Littke, R., 2012, Evolution of petrophysical properties of oil shales during high-temperature compaction tests: Implications for petroleum expulsion: Marine and Petroleum Geology, v. 31, no. 1, p. 110-124.

Eseme, E., Littke, R., and Krooss, B. M., 2006a, Factors controlling the thermo-mechanical deformation of oil shales: Implications for compaction of mudstones and exploitation: Marine and Petroleum Geology, v. 23, no. 7, p. 715-734.

Eseme, E., Littke, R., and Krooss, B. M., 2006b, Factors controlling the thermo-mechanical deformation of oil shales: Implications for compaction of mudstones and exploitation: Marine and Petroleum Geology, v. 23, no. 7, p. 715-734.

Eseme, E., Urai, J. L., Krooss, B. M., and Littke, R., 2007, Review of mechanical properties of oil shales: Implications for exploitation and basin modelling: Oil Shale, v. 24, no. 2, p. 159-174.

Eshet, Y., Almogi-Labin, A., and Bein, A., 1994, Dinoflagellate Cysts, Paleoproductivity and Upwelling Systems - a Late Cretaceous Example from Israel: Marine Micropaleontology, v. 23, no. 3, p. 231-240.

Fairhurst, C., 1964, On the validity of the 'Brazilian' test for brittle materials: International Journal of Rock Mechanics and Mining Sciences & Geomechanics Abstracts, v. 1, no. 4, p. 535-546.

Forchheimer, P., 1901, Wasserbewegung durch boden: Z. Ver. Deutsch. Ing, v. 45, no. 1782, p. 1788.

Goodman, R. E., 1989, Introduction to rock mechanics, Wiley, 562 p.:

Griffith, A. A., 1921, The phenomena of rupture and flow in solids: Philosophical transactions of the royal society of london. Series A, containing papers of a mathematical or physical character, v. 221, p. 163-198.

Griffith, A. A., The theory of rupture, *in* Proceedings 1st Congr. Appl. Mech.1924, Volume 55, p. 55-63.

Gvirtzman, G., Almogi-Labin, A., Moshkovitz, S., Lewy, Z., Honigstein, A., and Reiss, Z., 1989, Upper Cretaceous high-resolution multiple stratigraphy, northern margin of the Arabian platform, central Israel: Cretaceous Research, v. 10, no. 2, p. 107-135.

Gvirtzman, G., Moshkovitz, S., and Reiss, Z., 1985, Senonian to Early Eocene Mount Scopus Group in the Hashefela Region, Central Israel - Stratigraphy and Basin Evolution: Israel Journal Of Earth Sciences, v. 34, no. 4, p. 172-192.

Gvirtzman, G., and Reiss, Z., 1965, Stratigraphic nomenclature in the Coastal Plain and Hashephela regions.: Geol. Surv. Isr.

Hatzor, Y. H., and Heyman, E. P., 1997, Dilation of anisotropic rock salt: Evidence from Mount Sedom diapir: Journal of Geophysical Research, v. 102, no. B7, p. 14853-14868.

Hutton, A. C., 1987, Petrographic Classification of Oil Shales: International Journal of Coal Geology, v. 8, no. 3, p. 203-231.

IEA, 2010, World Energy Outlook 2010: Paris, OECD, p. 165.

Jaeger, J. C., Cook, N. G. W., and Zimmerman, R. W., 2007, Fundamentals of rock mechanics, Wiley-Blackwell.

Jones, S. C., 1972, A rapid accurate unsteady-state Klinkenberg permeameter: Old SPE Journal, v. 12, no. 5, p. 383-397.

Kirsch, G., 1898, Theory of Elasticity and Application in Strength of Materials: Zeitschrift des Vereins Deutscher Ingenieure, v. 42, no. 29, p. 797-807.

Klinkenberg, L. J., 1941, The permeability of porous media to liquids and gases: Drilling and Production Practice, American Petroleum Inst., p. 200-213.

Kundt, A., and Warburg, E., 1875, On the viscosity and heat conduction in rarified gases: Ann. Physik, v. 156, p. 177-211.

Minster, T., 2009, Oil shale deposits in Israel: Geological Survey of Israel.

Ratigan, J., Van Sambeek, L., DeVries, K., and Nieland, J., 1991, The influence of seal design on the development of the disturbed rock zone in the WIPP alcove seal tests: Topical Report RSI-0400.

Shahar, Y., Team, G. S. o. I. S., and no.6, S. o. I. M. o. D. G. S. S. S., 1968, Type Section of the Campanian Maastrichtian Ghareb Formation in the Oron Syncline (Northern Negev), Israel Ministry of Development.

Spiers, C., Peach, C., and Brzesowsky, R., 1988, Long-term Rheological and Transport Properties of Dry and Wet Salt Rocks: Final Report, Office for Official Publications of the European Communities.

Spiro, B., 1980, Geochemistry and mineralogy of bituminous rocks in Israel. [Ph.D.: Hebrew University, Jerusalem.

Talesnick, M. L., Hatzor, Y. H., and Tsesarsky, M., 2001, The elastic deformability and strength of a high porosity, anisotropic chalk: International Journal of Rock Mechanics and Mining Sciences, v. 38, no. 4, p. 543-555.

Tissot, B. P., and Vandenbroucke, M., 1983, Geochemistry and Pyrolysis of Oil Shales: Abstracts of Papers of the American Chemical Society, v. 185, no. Mar, p. 53-Geoc.

Tissot, B. P., and Welte, D. H., 1984, Petroleum formation and occurrence, Berlin, Springer, 699 p.:

Van Sambeek, L. L., Ratigan, J. L., and Hansen, F. D., 1993, Dilatancy of rock salt in laboratory tests: International Journal of Rock Mechanics and Mining Sciences & Geomechanics Abstracts, v. 30, p. 735-738.

Warburg, E., 1876, Annalen der Physik, v. 159, no. 399.

Appendices

Appendix 1- Physical and geometrical parameters of the tested samples

Type of Test	Sample	Depth, m	D, mm	L, mm	V, cm^3	W, g	ρ, g/cm3
Uniaxial compression	AD1-11a	291.4-292.95	54.05	105.11	241.17	347.71	1.44
	AD1-27c	338.7-341.75	53.72	108.41	245.71	443.50	1.80
	AD1-34b	356.9-359.95	53.95	104.78	239.53	382.97	1.60
	AD1-40b	375-378.3	53.59	105.20	237.32	318.75	1.34
	AD1-55a	420-423	53.78	106.40	241.70	404.00	1.67
	AD1-64c	447-450	53.98	106.35	243.38	422.61	1.74
	AD1-104b	570.65-573.7	53.82	105.28	239.60	448.39	1.87
	AD1-113b	598.1-601.15	53.88	109.22	249.03	503.65	2.02
Triaxial compression	AD1-27c2	338.7-341.75	53.75	108.28	245.69	444.05	1.81
	AD1-28a	341.75-344.8	53.75	106.85	242.45	413.94	1.71
	AD1-26a	335.65-338.7	53.83	106.91	243.31	457.51	1.88
	AD1-26a2	335.65-338.7	53.96	106.45	243.43	451.16	1.85
	AD1-29b	344.8 - 347.85	53.87	106.65	243.08	434.09	1.79
	AD1-29b2	344.8 - 347.85	53.95	104.75	239.46	439.27	1.83
	AD1-27a	338.7-341.75	53.90	104.02	237.35	430.49	1.81
Hydrostatic compression	AD1-4-c	271.6-274.65	53.58	104.53	235.69	342.55	1.45
	AD1-27b	338.7-341.75	53.72	106.38	241.11	455.08	1.89
Brazilian	AD1-1-a	265.3-266.8	53.33	28.44	63.53	87.93	1.38
	AD1-1-a	265.3-266.8	53.38	26.02	58.24	79.93	1.37
	AD1-1-a	265.3-266.8	53.45	26.18	58.74	83.70	1.43
	AD1-1-a	265.3-266.8	53.51	26.08	58.65	85.91	1.46
	AD1-4-c	271.6-274.65	54.08	25.78	59.22	101.41	1.71
	AD1-4-c	271.6-274.65	54.25	26.82	61.99	103.75	1.67
	AD1-4-c	271.6-274.65	54.24	28.08	64.89	92.19	1.42
	AD1-4-c	271.6-274.65	54.25	26.41	61.05	86.86	1.42
	AD1-11-a	291.4-292.95	53.85	28.09	63.98	86.81	1.36
	AD1-11-a	291.4-292.95	54.21	27.09	62.53	83.72	1.34
	AD1-24a	329.55-332.6	53.80	30.05	68.31	113.68	1.66
	AD1-24a	329.55-332.6	53.98	26.51	60.67	100.24	1.65
	AD1-24a	329.55-332.6	53.95	30.20	69.04	115.45	1.67
	AD1-26a	335.65-338.7	53.75	29.76	67.53	112.90	1.67
	AD1-26a	335.65-338.7	53.76	29.09	66.03	104.37	1.58
	AD1-26a	335.65-338.7	53.83	27.85	63.38	116.54	1.84
	AD1-27c	338.7-341.75	53.55	29.26	65.90	102.64	1.56
	AD1-27c	338.7-341.75	53.84	28.80	65.57	118.14	1.80
	AD1-28-a	341.75-344.8	53.87	26.85	61.20	91.37	1.49

Type of Test	Sample	Depth, m	D, mm	L, mm	V, cm^3	W, g	ρ, g/cm3
Brazilian	AD1-28-a	341.75-344.8	54.02	27.90	63.94	93.68	1.47
	AD1-28b	341.75-344.8	53.76	29.50	66.96	97.47	1.46
	AD1-29-c	344.8 - 347.85	54.01	27.60	63.23	95.52	1.51
	AD1-29-c	344.8 - 347.85	53.90	28.80	65.71	98.97	1.51
	AD1-30-a	348.77-350.82	53.93	27.20	62.13	136.02	2.19
	AD1-30-a	348.77-350.82	53.82	28.30	64.38	142.93	2.22
	AD1-31-a	350.82-352	53.80	26.90	61.15	90.79	1.48
	AD1-31-a	350.82-352	53.85	28.20	64.23	95.18	1.48
	AD1-32-a	352-353	53.80	28.23	64.19	89.41	1.39
	AD1-32-a	352-353	53.90	24.34	55.54	76.34	1.37
	AD1-32-a	352-353	53.96	27.28	62.38	85.43	1.37
	AD1-32-a	352-353	53.65	28.54	64.52	96.91	1.50
	AD1-33-a	353.81-356.4	53.73	25.80	58.50	85.83	1.47
	AD1-33-a	353.81-356.4	53.74	26.91	61.04	88.75	1.45
	AD1-33-a	353.81-356.4	53.65	27.57	62.33	89.33	1.43
	AD1-34-b	356.9-359.95	53.82	26.70	60.74	92.55	1.52
	AD1-34-b	356.9-359.95	53.95	28.60	65.38	96.65	1.48
	AD1-35-c	359.95-363	54.01	27.43	62.84	95.86	1.53
	AD1-35-c	359.95-363	53.97	28.83	65.95	101.84	1.54
	AD1-36-a	363-366.05	53.75	30.70	69.66	109.31	1.57
	AD1-36-a	363-366.05	53.80	30.38	69.06	106.74	1.55
	AD1-38-c	369.3-372.3	53.81	29.25	66.52	96.05	1.44
	AD1-38-c	369.3-372.3	53.90	27.40	62.52	89.58	1.43
	AD1-39-b	372.3-375.3	53.89	29.50	67.29	109.83	1.63
	AD1-39-b	372.3-375.3	53.83	27.50	62.59	98.89	1.58
	AD1-40-b	375-378.3	53.88	31.50	71.82	100.91	1.41
	AD1-40-b	375-378.3	54.01	30.80	70.56	99.28	1.41
	AD1-42-b	381.3-384.3	54.10	29.50	67.81	99.75	1.47
	AD1-42-b	381.3-384.3	53.90	28.40	64.80	96.71	1.49
	AD1-42-b	381.3-384.3	54.02	28.10	64.40	96.65	1.50
	AD1-43-b	384.3-387.1	53.84	27.13	61.77	89.88	1.46
	AD1-43-b	384.3-387.1	54.01	27.70	63.46	91.47	1.44
	AD1-43-b	384.3-387.1	53.80	27.73	63.04	93.01	1.48
	AD1-45-a	390.1-393.1	53.80	28.55	64.90	96.22	1.48
	AD1-45-a	390.1-393.1	53.90	28.15	64.23	93.33	1.45
	AD1-47a	396.1-399	53.88	28.10	64.07	107.96	1.69

Type of Test	Sample	Depth, m	D, mm	L, mm	V, cm^3	W, g	ρ, g/cm3
Brazilian	AD1-47a	396.1-399	53.80	29.45	66.95	102.55	1.53
	AD1-51a	408-411	53.81	29.40	66.86	101.41	1.52
	AD1-52b	411-414	53.87	27.50	62.68	88.73	1.42
	AD1-54-c	417-420	53.88	25.80	58.83	82.93	1.41
	AD1-54-a	417-420	53.68	27.15	61.44	83.95	1.37
	AD1-54-a	417-420	53.83	26.15	59.51	86.65	1.46
	AD1-55-a	420-423	53.90	27.71	63.23	88.65	1.40
	AD1-57b	426-429	53.79	27.65	62.83	93.25	1.48
	AD1-57b	426-429	53.89	29.80	67.97	97.99	1.44
	AD1-57b	426-429	53.79	27.50	62.49	94.01	1.50
	AD1-58b	429-432	53.86	29.10	66.30	96.86	1.46
	AD1-58b	429-432	53.83	30.05	68.39	96.34	1.41
	AD1-58b	429-432	53.79	27.53	62.56	92.77	1.48
	AD1-61b	438-441	53.88	26.70	60.88	98.52	1.62
	AD1-61b	438-441	53.86	29.10	66.30	94.19	1.42
	AD1-61b	438-441	53.95	27.72	63.37	103.25	1.63
	AD1-62c	441-444	53.98	28.40	64.99	113.18	1.74
	AD1-62c	441-444	53.95	27.30	62.41	101.74	1.63
	AD1-62c	441-444	53.94	29.95	68.44	116.94	1.71
	AD1-65c	450-453	53.94	28.64	65.45	129.12	1.97
	AD1-65c	450-453	53.85	27.52	62.68	121.68	1.94
	AD1-65c	450-453	53.86	28.30	64.48	125.85	1.95
	AD1-67c	456-459	53.95	29.20	66.75	137.44	2.06
	AD1-67c	456-459	53.96	29.19	66.75	130.39	1.95
	AD1-67c	456-459	53.91	28.17	64.30	129.06	2.01
	AD1-71c	468-471	53.95	30.10	68.81	121.01	1.76
	AD1-71c	468-471	53.94	27.50	62.84	109.14	1.74
	AD1-71c	468-471	53.91	28.30	64.60	116.81	1.81
	AD1-72a	471-474	53.78	27.35	62.13	88.67	1.43
	AD1-72a	471-474	53.76	27.80	63.10	88.62	1.40
	AD1-72a	471-474	53.65	28.20	63.75	92.37	1.45
	AD1-73c	474-477	53.83	29.80	67.82	114.34	1.69
	AD1-73c	474-477	53.85	28.75	65.48	110.50	1.69
	AD1-73c	474-477	53.80	30.20	68.65	114.98	1.67
	AD1-77a	486-489	53.84	28.48	64.84	99.83	1.54
	AD1-77a	486-489	53.86	28.30	64.48	99.16	1.54

Type of Test	Sample	Depth, m	D, mm	L, mm	V, cm^3	W, g	ρ, g/cm3
Brazilian	AD1-77a	486-489	53.82	29.50	67.11	103.40	1.54
	AD1-79c	492-495	53.95	28.50	65.15	116.83	1.79
	AD1-79c	492-495	53.92	28.70	65.53	116.51	1.78
	AD1-81a	498-501	53.75	28.40	64.44	117.36	1.82
	AD1-81a	498-501	53.84	29.12	66.30	119.60	1.80
	AD1-81a	498-501	53.70	28.50	64.55	113.52	1.76
	AD1-83c	504-507	53.63	30.13	68.06	108.48	1.59
	AD1-83c	504-507	53.62	28.85	65.15	102.77	1.58
	AD1-86b	513-516	53.93	28.80	65.79	110.13	1.67
	AD1-86b	513-516	53.99	29.50	67.54	110.23	1.63
	AD1-86b	513-516	53.88	29.80	67.95	112.62	1.66
	AD1-88a	519-522	53.83	28.70	65.32	111.06	1.70
	AD1-89a	522-525	53.75	28.95	65.69	101.22	1.54
	AD1-89a	522-525	53.76	28.80	65.37	99.50	1.52
	AD1-89a	522-525	53.78	28.20	64.06	96.30	1.50
	AD1-94-b	540-542.5	53.76	24.74	56.15	90.04	1.60
	AD1-94-b	540-542.5	53.82	22.37	50.89	81.02	1.59
	AD1-96c	546-549	53.82	28.56	64.97	120.01	1.85
	AD1-96c	546-549	53.92	28.35	64.74	119.60	1.85
	AD1-96c	546-549	53.97	29.12	66.62	118.96	1.79
	AD1-97c	549-552	53.84	27.90	63.52	126.03	1.98
	AD1-97c	549-552	53.90	27.70	63.20	117.36	1.86
	AD1-97c	549-552	53.85	29.54	67.28	117.49	1.75
	AD1-99b	555-558	53.88	28.60	65.21	120.51	1.85
	AD1-99b	555-558	53.91	29.80	68.02	113.70	1.67
	AD1-99b	555-558	53.93	28.70	65.56	106.32	1.62
	AD1-102b	564-567.6	53.88	28.10	64.07	134.07	2.09
	AD1-102b	564-567.6	53.87	27.25	62.11	119.63	1.93
	AD1-102b	564-567.6	53.95	27.50	62.86	132.39	2.11
	AD1-104-b	570.65-573.7	53.86	26.71	60.86	114.70	1.88
	AD1-104-b	570.65-573.7	54.03	21.77	49.92	104.45	2.09
	AD1-104-b	570.65-573.7	53.84	26.23	59.72	108.22	1.81
	AD1-104-b	570.65-573.7	53.85	25.06	57.07	106.74	1.87
	AD1-113-b	598.1-601.15	53.80	27.45	62.39	132.68	2.13
	AD1-113-b	598.1-601.15	53.86	27.92	63.60	130.45	2.05
	AD1-113-b	598.1-601.15	53.93	27.41	62.63	135.08	2.16
	AD1-113-b	598.1-601.15	53.81	27.84	63.32	130.62	2.06

Type of Test	Sample	Depth, m	D, mm	L, mm	V, cm^3	W, g	ρ, g/cm3
Petrophysical	AD1-1a-b	265.3-266.8	24.37	26.67	12.44	17.87	1.44
	AD1-2a-a	266.8-269.3	24.36	27.30	12.72	18.46	1.45
	AD1-2a-b	266.8-269.3	24.39	28.05	13.11	18.74	1.43
	AD1-3a-a	269.5-271	24.36	29.10	13.56	19.27	1.42
	AD1-3a-b	269.5-271	24.37	29.05	13.55	19.29	1.42
	AD1-3a-o1	269.5-271	24.51	30.26	14.28	21.04	1.47
	AD1-4c-a	271.6-274.65	24.50	26.15	12.33	17.98	1.46
	AD1-4c-b	271.6-274.65	24.40	26.25	12.27	18.00	1.47
	AD1-4c-o	271.6-274.65	24.36	25.85	12.05	17.03	1.41
	AD1-4c-o	271.6-274.65	24.45	27.85	13.08	18.08	1.38
	AD1-5b-a	274.65-277.7	24.50	28.20	13.29	19.17	1.44
	AD1-5b-b	274.65-277.7	24.43	30.50	14.30	20.37	1.42
	AD1-5b-o2	274.65-277.7	24.56	30.05	14.24	20.42	1.43
	AD1-6c-a	277.7-280.75	24.51	27.60	13.02	18.65	1.43
	AD1-6c-b	277.7-280.75	24.45	26.85	12.61	18.22	1.45
	AD1-6c-o1	277.7-280.75	24.48	29.90	14.07	20.56	1.46
	AD1-7b-a	280.75-283.8	24.34	26.75	12.45	18.15	1.46
	AD1-7b-b	280.75-283.8	24.37	30.60	14.27	20.77	1.46
	AD1-7b-o1	280.75-283.8	24.45	25.20	11.83	17.16	1.45
	AD1-8b-a	283.8-286.85	24.50	29.75	14.03	20.44	1.46
	AD1-8b-b	283.8-286.85	24.45	29.32	13.77	20.23	1.47
	AD1-8b-o1	283.8-286.85	24.48	27.08	12.75	19.05	1.49
	AD1-9a-a	286.85-289.9	24.38	27.80	12.98	19.53	1.50
	AD1-9a-b	286.85-289.9	24.35	28.80	13.41	20.38	1.52
	AD1-9a-o1	286.85-289.9	24.52	27.40	12.94	20.22	1.56
	AD1-10a-b	289.9-291.4	24.39	27.35	12.78	18.99	1.49
	AD1-11a-a	291.4-292.95	23.90	27.20	12.20	18.62	1.53
	AD1-11a-b	291.4-292.95	24.49	26.75	12.60	18.45	1.46
	AD1-11a-o	291.4-292.95	24.48	26.80	12.61	18.34	1.45
	AD1-11b-a	291.4-292.95	24.29	30.60	14.18	20.24	1.43
	AD1-11b-b	291.4-292.95	24.30	30.20	14.01	20.10	1.43
	AD1-11b-o1	291.4-292.95	24.45	27.95	13.12	19.26	1.47
	AD1-12b-a	292.95-296	24.23	29.05	13.40	19.51	1.46
	AD1-12b-b	292.95-296	24.30	29.30	13.59	19.88	1.46
	AD1-12b-o1	292.95-296	24.40	29.90	13.98	20.50	1.47
	AD1-13b-a	296-299.05	24.32	28.40	13.19	18.84	1.43

Type of Test	Sample	Depth, m	D, mm	L, mm	V, cm^3	W, g	ρ, g/cm3
Petrophysical	AD1-13b-b	296-299.05	24.50	28.10	13.25	18.73	1.41
	AD1-13b-o1	296-299.05	24.45	28.76	13.50	19.28	1.43
	AD1-14a-a	299.05-302.1	24.43	29.93	14.03	20.62	1.47
	AD1-14a-o2	299.05-302.1	24.50	28.60	13.48	20.24	1.50
	AD1-15a-a	302.1-305.15	24.40	28.90	13.51	19.25	1.42
	AD1-15a-b	302.1-305.15	24.37	28.90	13.48	18.82	1.40
	AD1-15a-o1	302.1-305.15	24.45	27.50	12.91	18.35	1.42
	AD1-16a-a	305.15-308.2	24.38	27.05	12.63	18.07	1.43
	AD1-16a-b	305.15-308.2	24.39	27.55	12.87	18.63	1.45
	AD1-16a-o1	305.15-308.2	24.42	29.40	13.77	20.05	1.46
	AD1-17a-a	308.2-311.25	24.42	29.90	14.00	20.48	1.46
	AD1-17a-b	308.2-311.25	24.43	28.25	13.24	19.23	1.45
	AD1-17a-o1	308.2-311.25	24.49	28.48	13.42	20.01	1.49
	AD1-19b-o1	314.3-317.35	24.42	29.10	13.63	19.62	1.44
	AD1-20a-a	317.35-320.4	24.40	28.22	13.20	19.46	1.47
	AD1-20a-a1	317.35-320.4	24.30	24.60	11.41	16.99	1.49
	AD1-20a-b	317.35-320.4	24.32	27.30	12.68	18.92	1.49
	AD1-20a-o	317.35-320.4	24.42	30.50	14.29	20.50	1.44
	AD1-20c-b	317.35-320.4	24.23	29.30	13.51	20.11	1.49
	AD1-20c-o1	317.35-320.4	24.37	28.30	13.20	19.70	1.49
	AD1-22b-o1	323.45-326.5	24.39	25.45	11.89	17.63	1.48
	AD1-23a-a	326.5-329.55	24.42	28.05	13.14	18.90	1.44
	AD1-23a-b	326.5-329.55	24.38	26.70	12.46	18.15	1.46
	AD1-23a-o1	326.5-329.55	24.47	26.74	12.58	18.51	1.47
	AD1-24a-a	329.55-332.6	24.31	26.65	12.37	17.86	1.44
	AD1-24a-b	329.55-332.6	24.21	25.90	11.92	17.30	1.45
	AD1-24a-o1	329.55-332.6	24.40	28.30	13.23	19.18	1.45
	AD1-26a-a	335.65-338.7	24.10	29.50	13.46	19.91	1.48
	AD1-26a-b	335.65-338.7	24.20	30.30	13.94	20.37	1.46
	AD1-26a-o1	335.65-338.7	24.30	27.80	12.89	19.21	1.49
	AD1-27c-a	338.7-341.75	24.33	30.10	13.99	20.35	1.45
	AD1-27c-o1	338.7-341.75	24.35	29.20	13.60	19.27	1.42
	AD1-28a-a	341.75-344.8	24.30	26.63	12.35	17.24	1.40
	AD1-28a-b	341.75-344.8	24.28	28.52	13.20	18.47	1.40
	AD1-28a-o1	341.75-344.8	24.40	30.02	14.04	20.39	1.45
	AD1-29c-a	344.8 - 347.85	24.48	29.50	13.88	19.56	1.41

Type of Test	Sample	Depth, m	D, mm	L, mm	V, cm^3	W, g	ρ, g/cm3
Petrophysical	AD1-29c-b	344.8 - 347.85	24.34	28.30	13.17	18.67	1.42
	AD1-29c-o1	344.8 - 347.85	24.54	27.50	13.01	18.70	1.44
	AD1-30a-a	348.77-350.82	24.36	28.50	13.28	18.67	1.41
	AD1-30a-b	348.77-350.82	24.40	26.60	12.44	23.87	1.92
	AD1-30a-o1	348.77-350.82	24.55	28.20	13.35	28.68	2.15
	AD1-30a-o2	348.77-350.82	24.62	27.86	13.26	28.43	2.14
	AD1-31a-a	350.82-352	24.45	28.10	13.19	18.36	1.39
	AD1-31a-b	350.82-352	24.39	28.20	13.18	18.27	1.39
	AD1-31a-o1	350.82-352	24.47	27.60	12.98	18.16	1.40
	AD1-31a-o2	350.82-352	24.49	27.78	13.09	18.73	1.43
	AD1-32a-a1	352-353	24.45	25.50	11.97	17.29	1.44
	AD1-32a-a2	352-353	24.37	25.91	12.09	17.70	1.46
	AD1-32a-b	352-353	24.41	25.67	12.01	17.12	1.43
	AD1-32a-o	352-353	24.47	26.09	12.27	17.68	1.44
	AD1-33a-a	353.81-356.4	24.36	26.43	12.32	17.43	1.41
	AD1-33a-b	353.81-356.4	24.38	26.15	12.21	17.49	1.43
	AD1-33a-o	353.81-356.4	24.28	26.40	12.22	17.24	1.41
	AD1-33a-o1	353.81-356.4	24.30	27.45	12.73	18.24	1.43
	AD1-34b-b	356.9-359.95	24.39	28.55	13.34	18.77	1.41
	AD1-34b-o	356.9-359.95	24.45	28.50	13.38	18.85	1.41
	AD1-35c-a	359.95-363	24.37	28.80	13.43	18.85	1.40
	AD1-35c-b	359.95-363	24.45	27.70	13.01	18.25	1.40
	AD1-35c-o1	359.95-363	24.40	28.35	13.26	18.60	1.40
	AD1-36a-a	363-366.05	24.39	28.05	13.11	19.14	1.46
	AD1-36a-b	363-366.05	24.33	27.90	12.97	19.45	1.50
	AD1-36a-o	363-366.05	24.38	28.50	13.30	19.82	1.49
	AD1-36a-o1	363-366.05	24.41	28.05	13.13	19.72	1.50
	AD1-37b-a	366.3-369.3	24.56	27.80	13.17	33.33	2.53
	AD1-37b-b	366.3-369.3	24.60	27.12	12.89	32.39	2.51
	AD1-37b-o1	366.3-369.3	24.63	30.30	14.44	35.29	2.44
	AD1-38c-a	369.3-372.3	24.37	29.40	13.71	19.60	1.43
	AD1-38c-b	369.3-372.3	24.47	31.90	15.00	21.17	1.41
	AD1-38c-o	369.3-372.3	24.40	29.20	13.65	19.24	1.41
	AD1-38c-o2	369.3-372.3	24.50	28.00	13.20	18.46	1.40
	AD1-39b-o1	372.3-375.3	24.45	27.80	13.05	17.64	1.35
	AD1-40b-a	375-378.3	24.42	28.62	13.40	18.03	1.35

Type of Test	Sample	Depth, m	D, mm	L, mm	V, cm^3	W, g	ρ, g/cm3
Petrophysical	AD1-40b-b	375-378.3	24.33	29.60	13.76	18.50	1.34
	AD1-40b-o	375-378.3	24.46	28.85	13.56	18.40	1.36
	AD1-40b-o1	375-378.3	24.48	25.20	11.86	16.14	1.36
	AD1-42b-b	381.3-384.3	24.35	28.62	13.33	18.66	1.40
	AD1-42b-o1	381.3-384.3	24.41	27.52	12.88	17.93	1.39
	AD1-43b-a	384.3-387.1	24.35	29.25	13.62	18.90	1.39
	AD1-43b-b	384.3-387.1	24.30	30.05	13.94	19.63	1.41
	AD1-43b-o	384.3-387.1	24.30	27.51	12.76	17.80	1.40
	AD1-47a-a	396.1-399	24.30	29.80	13.82	19.61	1.42
	AD1-47a-b	396.1-399	24.40	28.40	13.28	18.65	1.40
	AD1-47a-o1	396.1-399	24.38	28.30	13.21	18.99	1.44
	AD1-49b-a	402.1-405.1	24.33	28.30	13.16	18.93	1.44
	AD1-49b-b	402.1-405.1	24.24	29.30	13.52	19.52	1.44
	AD1-49b-o1	402.1-405.1	24.41	27.80	13.01	18.90	1.45
	AD1-50c-a	405-408	24.50	27.52	12.97	17.52	1.35
	AD1-50c-b	405-408	24.43	27.80	13.03	17.70	1.36
	AD1-50c-o1	405-408	24.40	27.85	13.02	17.84	1.37
	AD1-51a-a	408-411	24.40	25.90	12.11	16.73	1.38
	AD1-51a-b	408-411	24.50	25.70	12.12	16.98	1.40
	AD1-51a-o1	408-411	24.51	24.85	11.72	16.59	1.41
	AD1-54a-a	417-420	24.35	27.17	12.65	17.32	1.37
	AD1-54a-b	417-420	24.43	27.85	13.05	17.76	1.36
	AD1-54a-o1	417-420	24.56	27.74	13.14	18.73	1.43
	AD1-54c-a	417-420	24.43	27.05	12.68	17.47	1.38
	AD1-54c-b	417-420	24.46	28.60	13.44	18.65	1.39
	AD1-55a-a	420-423	24.42	26.95	12.62	17.17	1.36
	AD1-55a-b	420-423	24.40	27.55	12.88	17.57	1.36
	AD1-55a-o1	420-423	24.45	29.12	13.67	18.68	1.37
	AD1-55b-a	420-423	24.40	30.10	14.07	19.22	1.37
	AD1-55b-b	420-423	24.42	29.20	13.68	18.74	1.37
	AD1-55b-o1	420-423	24.52	28.11	13.27	18.23	1.37
	AD1-56a-a	423-426	24.41	26.75	12.52	17.15	1.37
	AD1-56a-o1	423-426	24.42	28.35	13.28	18.26	1.38
	AD1-57b-a	426-429	24.35	29.42	13.70	19.19	1.40
	AD1-57b-o1	426-429	24.45	29.50	13.85	19.49	1.41
	AD1-58b-a	429-432	24.50	29.35	13.84	19.19	1.39

Type of Test	Sample	Depth, m	D, mm	L, mm	V, cm^3	W, g	ρ, g/cm3
Petrophysical	AD1-58b-b	429-432	24.45	27.40	12.86	17.64	1.37
	AD1-58b-o1	429-432	24.49	27.90	13.14	17.99	1.37
	AD1-61b-a	438-441	24.30	29.30	13.59	18.35	1.35
	AD1-61b-b	438-441	24.33	29.49	13.71	18.53	1.35
	AD1-61b-o1	438-441	24.45	28.40	13.33	18.04	1.35
	AD1-62c-a	441-444	24.42	27.20	12.74	17.75	1.39
	AD1-62c-b	441-444	24.40	27.90	13.05	18.31	1.40
	AD1-62c-o1	441-444	24.46	26.80	12.59	17.87	1.42
	AD1-64b-a	447-450	24.52	29.95	14.14	19.46	1.38
	AD1-64b-b	447-450	24.47	26.55	12.49	17.39	1.39
	AD1-64b-o1	447-450	24.52	28.45	13.43	18.68	1.39
	AD1-64c-o1	447-450	24.48	29.59	13.93	20.46	1.47
	AD1-64c-o2	447-450	24.46	27.80	13.06	19.12	1.46
	AD1-65c-a	450-453	24.41	28.35	13.27	21.53	1.62
	AD1-65c-b	450-453	24.45	26.85	12.61	20.24	1.61
	AD1-65c-o1	450-453	24.56	28.15	13.34	21.44	1.61
	AD1-67c-a	456-459	24.45	27.60	12.96	22.62	1.75
	AD1-67c-o1	456-459	24.52	27.35	12.91	22.78	1.76
	AD1-68a-a	459-462	24.46	28.30	13.30	22.63	1.70
	AD1-68a-b	459-462	24.52	27.50	12.99	21.94	1.69
	AD1-68a-o1	459-462	24.51	28.05	13.23	22.27	1.68
	AD1-71c-a	468-471	24.50	27.25	12.85	18.80	1.46
	AD1-71c-b	468-471	24.30	28.20	13.08	19.11	1.46
	AD1-71c-o1	468-471	24.45	29.40	13.80	20.50	1.49
	AD1-72a-b	471-474	24.42	28.60	13.40	19.16	1.43
	AD1-72a-o1	471-474	24.50	28.13	13.26	19.57	1.48
	AD1-73c-a	474-477	24.18	25.95	11.92	19.99	1.68
	AD1-73c-b	474-477	24.17	25.65	11.77	19.77	1.68
	AD1-73c-o1	474-477	24.15	25.40	11.63	20.14	1.73
	AD1-75b-a	480-483	24.40	24.60	11.50	17.62	1.53
	AD1-75b-b	480-483	24.40	28.60	13.37	20.35	1.52
	AD1-75b-o1	480-483	24.51	29.85	14.08	21.42	1.52
	AD1-76b-a	483-486	24.40	29.25	13.68	20.15	1.47
	AD1-76b-b	483-486	24.36	28.40	13.24	19.51	1.47
	AD1-76b-o1	483-486	24.46	26.75	12.57	18.33	1.46
	AD1-77a-a	486-489	23.95	26.30	11.85	17.63	1.49

Type of Test	Sample	Depth, m	D, mm	L, mm	V, cm^3	W, g	ρ, g/cm3
Petrophysical	AD1-77a-b	486-489	24.00	26.80	12.12	17.82	1.47
	AD1-77a-o1	486-489	24.20	26.12	12.01	17.98	1.50
	AD1-78b-b	489-492	24.30	27.25	12.64	19.20	1.52
	AD1-78b-o1	489-492	24.20	25.70	11.82	17.80	1.51
	AD1-79c-a	492-495	24.25	27.25	12.59	19.87	1.58
	AD1-79c-b	492-495	24.30	28.20	13.08	20.63	1.58
	AD1-79c-o1	492-495	24.52	28.50	13.46	21.64	1.61
	AD1-80a-a	495-498	24.30	29.10	13.50	26.04	1.93
	AD1-80a-b	495-498	24.30	30.05	13.94	27.03	1.94
	AD1-80a-o1	495-498	24.39	27.60	12.90	25.34	1.97
	AD1-81a-a	498-501	24.30	26.38	12.23	19.31	1.58
	AD1-81a-b	498-501	24.20	27.30	12.56	19.73	1.57
	AD1-81a-o1	498-501	23.98	27.50	12.42	19.63	1.58
	AD1-83c-b	504-507	23.90	25.40	11.40	18.06	1.58
	AD1-83c-o1	504-507	24.05	24.80	11.27	17.80	1.58
	AD1-84c-a	507-510	24.42	28.20	13.21	22.16	1.68
	AD1-84c-b	507-510	24.44	29.40	13.79	23.08	1.67
	AD1-84c-o1	507-510	24.53	28.42	13.43	22.21	1.65
	AD1-85b-a	510-513	24.30	28.50	13.22	21.71	1.64
	AD1-85b-b	510-513	24.30	28.80	13.36	21.96	1.64
	AD1-85b-o1	510-513	24.45	27.70	13.01	21.85	1.68
	AD1-86b-b	513-516	23.95	26.10	11.76	18.62	1.58
	AD1-86b-o1	513-516	24.40	25.17	11.77	17.98	1.53
	AD1-87b-a	516-519	24.44	25.35	11.89	17.30	1.45
	AD1-87b-b	516-519	24.05	25.60	11.63	17.32	1.49
	AD1-87b-o1	516-519	24.20	25.70	11.82	17.75	1.50
	AD1-88a-a	519-522	24.20	24.02	11.05	18.71	1.69
	AD1-88a-b	519-522	24.17	24.20	11.10	19.13	1.72
	AD1-88a-o1	519-522	24.22	23.50	10.83	18.48	1.71
	AD1-88a-o2	519-522	24.30	23.25	10.78	18.30	1.70
	AD1-89a-o1	522-525	22.60	25.70	10.31	16.31	1.58
	AD1-91a-a	528-531	24.08	23.50	10.70	18.66	1.74
	AD1-91a-o1	528-531	24.54	24.05	11.38	19.12	1.68
	AD1-96c-a	546-549	24.31	24.40	11.33	17.61	1.55
	AD1-96c-o1	546-549	24.40	23.20	10.85	17.53	1.62
	AD1-97c-a	549-552	24.35	23.50	10.94	18.50	1.69

Type of Test	Sample	Depth, m	D, mm	L, mm	V, cm^3	W, g	ρ, g/cm3
Petrophysical	AD1-97c-b	549-552	24.35	23.65	11.01	18.73	1.70
	AD1-97c-o1	549-552	24.52	23.60	11.14	19.33	1.73
	AD1-99b-a	555-558	24.30	24.40	11.32	18.62	1.65
	AD1-99b-b	555-558	24.39	23.45	10.96	18.06	1.65
	AD1-99b-o1	555-558	24.26	24.25	11.21	17.62	1.57
	AD1-101b-b	561-564	24.10	24.55	11.20	21.36	1.91
	AD1-101b-o1	561-564	24.42	25.30	11.85	21.82	1.84
	AD1-102b-a	564-567.6	24.39	24.90	11.63	21.84	1.88
	AD1-102b-b	564-567.6	24.32	24.80	11.52	21.75	1.89
	AD1-102b-o1	564-567.6	24.48	24.70	11.63	22.14	1.90
	AD1-104b-a	570.65-573.7	24.60	24.80	11.79	21.12	1.79
	AD1-104b-b	570.65-573.7	24.47	24.75	11.64	21.01	1.81
	AD1-104b-o	570.65-573.7	24.47	23.60	11.10	19.68	1.77
	AD1-104c-a	570.65-573.7	24.48	24.30	11.44	21.48	1.88
	AD1-104c-b	570.65-573.7	24.48	24.30	11.44	21.40	1.87
	AD1-104c-o	570.65-573.7	24.48	24.45	11.51	21.83	1.90
	AD1-113b-a	598.1-601.15	24.50	25.05	11.81	23.51	1.99
	AD1-113b-3a	598.1-601.15	24.51	24.85	11.72	23.18	1.98
	AD1-113b-b	598.1-601.15	24.50	24.45	11.53	22.83	1.98
	AD1-113b-o	598.1-601.15	24.50	24.30	11.46	23.69	2.07

Legend: *D* is the average diameter of rock sample; *L* is the average length of the sample; *V* is the bulk volume of sample, *W* is the weight of the sample, ρ is the bulk density of the sample at test conditions.

תקציר

פצלי השמן מאגן השפלה תוארו באופן נרחב מבחינה גיאולוגית, גיאוכימית והידרולוגית בספרות הקיימת, אך התכונות המכניות והפטרופיזיקליות מתוארות לראשונה במחקר זה. מבחינה ליתולוגית, פצלי השמן המצויים באגן השפלה שבמרכז הארץ הינם סלע קירטון ביטומני כהה בעל נקבוביות גבוהה (עד כ-37%) וחדירות נמוכה (כ-0.09 mD). במרכז החתך של קידוח אדרת הנחקר, בתצורת ע'רב, תכולת פחמן אורגני מגיעה עד ל-20% משקלי. החדירות (permeability) מראה התנהגות אנאיזוטרופית, כאשר הזרימה במאונך למישורי השיכוב (שאינם נראים לעין) מוגבלת בממוצע פי 5 מהזרימה לאורך מישורי השיכוב. מבחינה מכנית, הסלע מאופיין בהתנהגות פריכה ומתואר באמצעות קריטריון קולומב-מוהר הליניארי וקריטריון גריפית' הלא-ליניארי. הקוהזיה וזוית החיכוך הפנימית אשר חושבו מתוך קריטריון קולומב-מוהר באמצעות רגרסיה ליניארית הינם 5.51 MPa ו- 10.7°בהתאמה. חוזק הלחיצה החד צירי הינו 19 MPa בממוצע בתוך תצורת ע'רב וחוזק המתיחה הברזיליאני הינו כ- 3.1 MPa בממוצע במצב יבש וקטן כאשר תכולת הרטיבות עולה לערך ממוצע של כ-2.6 MPa בתכולת רטיבות של כ-25%. ניתן להבחין באנאיזוטרופיות מכנית ברורה, כאשר חוזק המתיחה במקביל לשיכוב גבוה פי 1.7 בממוצע מחוזק המתיחה בניצב לשיכוב. באמצעות בדיקות הלחיצה החד ציריות והתלת ציריות הוגדר גבול לחיצה-תפיחה אמפירי, גבול זה משמש לאנליזה של ההתנהגות הנפחית הצפויה של הסלע במצב מאמצים מוגדר מסוים ובמקרה של שינוי מצב מאמצים זה (כמו במקרה של פתיחת קדח אופקי או אנכי כחלק מתהליך הפקה אפשרי).

הנקבוביות, החדירות, מקדם ה"החלקה" ותכולת הפחמן האורגני נמדדו לפני ואחרי שלושה ניסויי הפקה (פירוליזה) שונים, במהלכם החומר האורגני (קרוגן ברובו) התפרק לתוצרי דלק וגז וכתוצאה מכך נפחו בסלע הצטמצם. הנקבוביות והחדירות טרם ההפקה אינם תלויים בתכולת החומר האורגני. לאחר הפירוליזה ושחרור הנוזלים והגז מהחומר האורגני נוצרת בו רשת חללים קטנים יותר, המורידה את גודל רדיוס החללים הממוצע של הסלע, אך מגדילה את נפח הנקבוביות הכולל של הסלע פי 1.28 בממוצע עד לערך של 62% כמעט ללא הבדל בין תנאי הפירוליזה השונים. החדירות גדלה משמעותית בסדר גודל בממוצע (עד 6.5 mD). השינוי בתכולת החומר האורגני תלויה בתכולתו הראשונית ובתנאי הפירוליזה: נמצא כי הפעלת לחץ מגדילה את כמות החומר האורגני השאריתי בסלע וכתוצאה מקטינה את הגידול בנקבוביות, האטת קצב העלאת הטמפרטורה במהלך הפירוליזה היא בעלת השפעה דומה אך במידה מועטה יותר. השינוי בחדירות תלוי בתכולת החומר האורגני הראשונית אך נמצא כבלתי תלוי בתנאי הפירוליזה. לכן ניתן להעריך את החדירות לאחר הפירוליזה בהינתן תכולת החומר האורגני הראשונית והחדירות ההתחלתית.

ממצאים אלו הינם בעלי חשיבות גדולה הקשר בין התכונות הפטרופיסיות של הסלע לתכולת החומר האורגני והשפעת תהליך המטורציה התרמלית ושחרור מי החללים והפרקציה הוולטילית על השינויים בתכונות אלה. למידע זה יש ערך רב להבנת תהליך הנדידה ולתכנון וניהול ההפקה בתהליך תרמלי בתת הקרקע מתוך סלע מקור כדוגמת הקירטון הביטומני מאגן השפלה.